Silicon Nanowires for Integrated Photonics: Bridging Nano and Micro Photonics

by

Mohammadreza Khorasaninejad

A thesis
presented to the University of Waterloo
in fulfillment of the
thesis requirement for the degree of
Doctor of Philosophy
in
Electrical and Computer Engineering

Waterloo, Ontario, Canada, 2012

I hereby declare that I am the sole author of this thesis. This is a true copy of the thesis, including any required final revisions, as accepted by my examiners. I understand that my thesis may be made electronically available to the public.

Abstract

Silicon Nanowires (SiNWs) with ability to confine carriers and photons in two directions while allowing propagation in third dimension offer interesting modified optical properties such as increased material absorption and optical non-linearities with regard to that of bulk silicon. Enhanced optical properties in SiNWs open a window not only to improve the performance of existing devices but also to realize novel structures. As such, I chose to investigate SiNWs for their applications in photonics, especially for sensing and non-linear devices. My goal was to conduct fundamental research on the optical properties of these SiNWs, and then develop an integration platform to realize practical devices. The platform should be compatible with IC manufacturing.

Electron Beam Lithography (EBL) using a Poly Methyl Methacrylate (PMMA) resist followed by Inductively Coupled Plasma Reactive Ion Etching (ICP-RIE) is used for SiNWs fabrication. Now we are able to fabricate nanowires as small as 15 nm in diameter with the smallest separation of 50 nm. In addition, the interface between SiNWs and Si substrate is optically smooth enabling us to fundamentally understand optical properties of these structures. During the course of this project, I have contributed new fundamental knowledge about SiNWs. For example, Second Harmonic Generation (SHG) is demonstrated in SiNWs, which is absent in bulk silicon. This is achieved by self-straining the nanowires and is the first demonstration of this kind. Second-order non-linearities are more efficient for optical signal processing than third-order ones (which have been used for silicon photonics devices so far). Therefore, these results open a new area of research in silicon. In addition to second order nonlinearity, high enhancement of Raman scattering is achieved in SiNWs fabricated on Silicon on Insulator (SOI) substrate. This can find promising applications in sensing and nonlinear based devices such as optical switches and logic gates. Further, polarization resolved reflections from these nanowire arrays were measured and significant differences were observed for the reflection characteristics for the s- and p-polarized beams. In order to understand these reflections, an effective index model is proposed based on calculations using Finite Difference Time Domain (FDTD) method. Results of this analysis provide useful information for designing of many optical devices using SiNWs such as solar cells and photodetectors.

As another part of this thesis, vivid colors in mutually coupled SiNWs is demonstrated where nanowire diameters range from 105 nm to 345 nm. A simple sensor is demonstrated by observing the change in the reflected color with changing refractive index of the surrounding medium. A refractive index resolution of 5×10^{-5} is achieved using a simple charge coupled device (CCD) camera.

Although, there were some paradigm shifting results during my fundamental studies, it became very apparent that SiNWs suffer from a major issue inhibiting their use in photonics devices. Below the diameter of 100 nm where these enhanced material properties were observed, SiNW is a poor optical waveguide with less than 1 % of light confined. The low confinement factor means that though the intrinsic properties of SiNWs increase, the overall device performance is not significantly enhanced. To overcome this issue, a new platform technology is invented, called Silicon Nanowire Optical Waveguide (SNOW). It combines the material advantages of nanostructures with the optical properties of conventional waveguides, and consists of arrays of nanowires in close proximity. It is shown that such a structure can guide an optical mode using the FDTD method. This waveguide structure can be used as a versatile platform to manufacture various devices such as sensors, switches, modulators, grating, and delay lines. For instance, a novel bio-sensor is proposed and designed whose sensitivity is enhanced by a factor of 20, compared to conventional silicon-wire waveguides.

Acknowledgements

I would like to thank my supervisors Prof. Simarjeet Singh Saini and Prof. Safieddin Safavi-Naeini for their guidance and support during my PhD studies. Especially I would like to thank Prof. Simarjeet Singh Saini for his encouragement, knowledge, patience and never ending enthusiasm throughout my PhD studies at the University of Waterloo. Special thanks to Prof. M. P. Anantram and Prof. Sujeet K. Chaudhuri for their insightful comments and useful discussions. I also would like to thank my thesis committee, Prof. Dayan Ban, Prof. Bo Cui, Prof. John Yeow and Prof. Zetian Mi for their insightful suggestions and comments on my thesis. I would like to thank Dr. Bahareh Sadeghi-Makki, Michael Adachi, Dr. Yipu Song, Brian Goddard, Vito Logiudice, Rodello Salandanan, Dr. Nathan Nelson-Fitzpatrick and Richard Barber for sharing their experience and expertise in clean room fabrication. I also would like to thank to all of my colleagues at Nanophotonics and Integrated Optoelectronics laboratory.

Last but not least, I would like to acknowledge the endless love and support from my family.

The work is funded by the Natural Sciences and Engineering Research Council of Canada (NSERC) and Ontario Centres of Excellence (OCE).

Dedication

This is dedicated to my parents and Shanshan.

Contents

List of Figures

Chapter 1

Introduction

Over the past two decades, significant progress has been made towards the fabrication, characterization, and utilization of new nano-sized semiconductor for a vast variety of applications. Essential physical properties of nano-sized semiconductors can be modified with regard to those of bulk material. These properties modification provides an opportunity to not only improve performance of existing devices but also realize new category of products. Among different types of nano-structures, the one-dimensional nanowires attract a great deal of attention. This interest arises from their capability to confine the photons or carriers in two dimensions, while allowing them to propagate in the third dimension. In addition, semiconductor nanowires as a one-dimensional nanostructures offer a great opportunity to study effects of size and dimensionality on physical properties. Results from this kind of study play a critical role in designing nano-devices using nanowires as building blocks.

1.1 Why SiNWs?

While silicon has been the material of choice for electronic devices for decades, only over the last decade it has been investigated for photonics applications. Silicon photonics offers low cost optoelectronic solutions for applications ranging from telecommunications to chip to chip interconnections. In addition to its low cost, its compatibility with silicon IC manufacturing, and silicon MEMS technology have stimulated a significant amount of research and generated a great deal of attention to the silicon photonics field. As a transmission medium, silicon has much higher nonlinear effects than the commonly used silicon dioxide. Silicon-on-Insulator (SOI) material

system, with its high index contrast, Δn of ~ 2 between Si and SiO_2, provides an excellent platform for the fabrication of photonic devices, with the prospect of full integration of electronic and optical devices on the same substrate. Additionally, SOI waveguides can confine the optical field to an area that is approximately an order of magnitude smaller than the modal area in a standard single-mode optical fiber. Propagation loss is another fundamental parameter that impacts virtually all optical devices. Silicon waveguides are characterized by losses in the range of $0.1 - 3\ dB/cm$ depending on the dimensions and fabrication process [8]. These beneficial points of Si encourage researchers to investigate various photonics devices in Si such as fast optical modulators (GHz) [9], optical switches [10], photodetector [11] among many others.

One of the major drawbacks of silicon is the absence of optical gain. Owing to its indirect bandgap, silicon has poor light emission properties. In addition, second order non-linearities are very weak in bulk silicon arising from inversion symmetry of the crystal lattice. As such, most of the active devices have been based on the third order non-linearity and two photon absorption [12–14]. Recently, progress has been made for non-linear mixing in SOI waveguides based on the third-order nonlinear response [15]. We also proposed all optical log operation by means of third-order nonlinearity and free carrier effects [14]. However, most of these devices suffer from a requirement for large pumping power making their practical use suspect. Here is the place where the role of nano-technology comes to the picture by either improving optical properties or creating new properties as compared to that of bulk silicon.

Since the 1990s, an important class of semiconductor nanostructures has emerged viz. the semiconductor nanowires consisting of diameters ranging from $2 - 200\ nm$. These structures differ from quantum dots or nano-crystals in that the confinement occurs in two directions only, allowing carriers or photons to freely travel in the third direction. Among different nano-structures, Silicon Nanowires (SiNWs) have recently attracted considerable attention because of their interesting physical properties. For instance, visible photoluminescence (PL) has been reported in silicon nanostructures [16, 17] which is promising for optoelectronics applications. PL at room temperature also has been observed in SiNWs with diameters varying from few nanometer to tens of nanometers. As an example, Yu *et al.* [18] showed emission of blue light from SiNWs which was visible to the naked. Their nanowires had an average diameter of 15 nm and were excited by a 325 nm laser. In this case, as the diameter is not small enough to provide quantum confinement, the photoluminescence was attributed to the 2 nm overcoating sheath of silicon oxide. Moreover, visible photoluminescence due to quantum confinement effects was reported by different groups [**?**, 19, 20]. Holmes *et al.* [19] reported visible photoluminescence due to quantum confinement effects

of SiNWs. In this case, SiNWs had diameters ranging from $4-5$ nm and were prepared by thermally degrading diphenylsilane in sc-hexane. Moreover, they showed effects of crystal orientation on the PL spectra. While $< 100 >$ oriented wires showed a sharp PL peak at 3.75 eV, $< 110 >$ oriented wires showed three peaks at 3.35 eV, 2.9 eV and 2.55 eV. Zhang *et al.* [20] have further investigated effect of quantum confinement effects in which they showed that photoluminescence blue-shifted by decreasing nanowire diameter. In their study, SiNWs were fabricated by laser ablation. The nanowire with different diameters were achieved by changing the ambient gas. Nanowire grown in N_2 had a diameter distribution peak at 6 nm and showed a PL peak of $1.99eV$. Diameter of nanowires increased to 9.5 nm by growing in Ar $(5\%H_2)$ ambient. These nanowires had a red-shifted PL peak at $1.58eV$. By further increasing the nanowire diameter to 13.2 nm, PL was vanished. Evidence of PL in SiNWs also provides an opportunity to fabricate light emitting devices [21, 22]. In [21], Electroluminescence (EL) devices based on SiNWs were demonstrated. SiNWs with diameter ranging from $20-40$ nm were fabricated using deep UV lithography followed by Reactive Ion Etching (RIE). Diameter of nanowire were further reduce to 10 nm by means of high-temperature thermal oxidation. EL in the visible range was observed with a maximum around 650 nm. In another work [22] EL was reported from SiNWs with average diameter of 4 nm grown from disilane. The emission peak occurred at about 600 nm and were attributed to band-to-band electronhole recombination. To observe the EL, the device was biased with a pulse with voltage 70 V and reputation rate of 3 kHz. These kind of studies clearly show power of nanotechnology as a lever to modify and enhance material properties. As one can see there is a extensive study on PL for last decades but no PL studies have been done on ordered SiNW arrays with diameter of tens of nanometers.

Another phenomenon which is very weak in bulk silicon is second order nonlinearity such as Second Harmonic Generation (SHG). This absence arises from inversion symmetry in silicon crystal [23] and only an electric dipole response from the surface or an electric quadruple response from the bulk is observed [24]. However, nanowires have great potentials that could make it possible to generate SHG. Strong SHG has been demonstrated from silicon nanocrystals embedded in silicon dioxide [25]. Ionic vibrations or excitonic self-trapping on radiative Si-Si dimer phase was suggested as the basic mechanism for introducing antiharmonicity. However, the nanocrystals are difficult to integrate in photonics integrated circuits using silicon-on-insulator (SOI) optical waveguides. Strained silicon has also been considered as a novel electro-optic material and a $\chi^{(2)}$ with 830 pmV^{-1} was observed by breaking the symmetry [26]. While SHG was not measured in these devices, it is expected to be present. Porous silicon has also been investigated along with integration with vertical photonic crys-

tals and SHG was achieved [27]. Again, porous silicon is difficult to integrate in planar lightwave circuits. In [28], plasma etching was used to disorder the surface of the silicon in SOI wafer to achieve second-harmonic and difference-frequency generation. SiNWs are promising as they have increased surface to volume ratio. While SHG is forbidden in the medium with inversion symmetry, it can be allowed on the surface due to broken symmetry [24]. With increased surface to volume ratio, SiNWs are ideal candidates to be investigated for SHG. There is also field enhancement on the surface of the nanowires due to very large dielectric mismatch. In addition, due to the large length to diameter ratio of nanowires, it is feasible to bend and consequently strain them. Strained SiNWs can be used to break the centro-symmetry and make second harmonic generation possible. In SiNWs, a very large 24 % strain has been achieved by using advanced nano-fabrication and polymers as straining mediums [29]. For the first time in this thesis, SHG is reported from self-strained SiNWs. Second-order non-linearities are more efficient for optical signal processing than third-order ones (which have been used for silicon devices so far). Therefore, our results open a new area of research in silicon.

Raman scattering is one of the nonlinear phenomena that attracts a great deal of attention with interesting photonics applications such a silicon lasers and amplifiers [12], optical modulators [13] and optical logic gates [14]. The Raman spectrum of bulk crystalline silicon has been studied and is well understood, possessing only one Raman active first-order phonon, centered in the Brillouin zone, with an optical phonon energy of 520 cm^{-1} [30,31]. It has been shown that the Raman enhancement per unit volume (REV) can be enhanced by three order of magnitude using SiNWs and silicon nanocones [32]. One study has shown enhanced Raman scattering from vertical SiNW arrays, with decreasing diameter, for wires ranging in diameter from 450 nm to 900 nm and morphology dependence on the enhancement [33]. However, no mention is made with regards to the center frequency of the vibrational mode, or about heating effects in highly ordered nanowire arrays. More important, most of the works have used REV to show Raman enhancement. While REV is an important parameter to understand the physics of Raman enhancement, the actual intensity values are as important from the applications point of view, since devices made of nanowire arrays will ultimately take advantage of this increased intensity. To our knowledge, in none of the previous studies which involve nanowire arrays, the actual Raman scattering intensities are mentioned.

In addition to improved and novel properties, SiNWs attract a lot of research interest owing to their special structures. SiNWs array provides an effective-index between air and bulk Si and it can be tuned by changing the physical parameters such as diameter, pitch and length. Therefore, SiNWs can use as a transition medium form

low refractive-index of air to high refractive index of silicon eventually decreasing the total reflection. Effect of sub-wavelength ensembles on reduction of reflected light have been studied for a long time. For the first time in 1967, Bernhard demonstrated the anti-reflective property of an array of sub-wavelength structures [34]. He reported that a periodic array of conical perturbations on the corneal lens of a moth eye significantly lower optical reflection. Then, Clapham *et al.* [35] patterned photoresist on glass to create artificial moth eye structures. They showed that the integrated specular reflection of white light was reduced to 0.2 %. This work was extended to silicon nanopillar by Gittleman *et al* [36], where they showed reduction of specular reflection to 10^{-3} or less for wavelengths below 1 μm. By fabrication of a similar texturing scheme, Craighead *et al.* [37] reported reduction of thin film amorphous silicon reflection to nearly zero over the visible spectrum [37]. Since then different groups have investigated anti-reflective properties in SiNWs [38, 39], and tapered silicon nano-structures [40, 41]. In addition to aforementioned experimental results, recently optical properties of SiNWs including absorption and reflection have been simulated with varying diameters and lengths [42]. However, experimental verification of the models has not been considered yet. Although enhanced absorption has been shown experimentally in [43], physical understanding behind it is still unclear.

Furthermore, SiNWs due to their large surface area have found promising applications in biosensing area. For example, Li *et al.* [44] demonstrated highly sensitive and sequence-specific DNA sensors using SiNWs. SiNW-based biosensors have also showed fast response and high sensitivity to glucose [45]. However, most of these works are based on electronics properties of SiNWs rather than of optical properties. Sensors also were demonstrated in porous silicon based optical interferometric biosensors [46], evanescent wave optical sensors in which the evanescent field is increased by use of SiNWs [6], and fluorescence sensors based on SiNWs [47]. In all of these experiments, an expensive measurement system is required such as spectrometers and tunable lasers, as they work by means of measuring the spectral changes in presence of the detectants.

1.2 Goal of This Research

SiNWs have a lot of promise in photonics applications; however, there are some lack of knowledge about optical properties of SiNWs as mentioned in previous section. Although bulk material properties have bee modified and enhanced in SiNWs; at device level the performance is lower than bulk devices. Therefore, in this study we try to fill these gaps. As it is difficult to ascertain optical properties of single SiNW

due to their small size, we decided to use array of nanowire. This was also based on the realization that most of the areas where the nanotechnology has become successful has been when an ensemble of nano-structure are used. In addition, electromagnetic modeling of nanowire in array is simple and fast as one can used periodic boundary condition in transverse directions. Based on this introduction, the goal of this thesis is as follow:

1. **Studying mechanical properties of SiNWs.**

   A lot of SiNWs fabricated and reported in literature are bunched. However there is no study to understand why and when this bunching happens. Therefore, several experiments were conducted to understand this phenomenon. The goal was to create engineering rules of when SiNWs can be vertical and when they bunch.

2. **Investigating how the optical properties of SiNWs change as compared to those of bulk Si.**

   Optical properties of SiNWs such as polarized-resolved reflection, photoluminescence and nonlinear gain including Raman Scattering and Second-Harmonic Generation were experimentally studied.

3. **Simulating and modeling obtained experimental results.**

   Modeling was used to understand experimental results and also to design and optimize enhanced properties.

4. **Applying the enhanced and modified properties to propose and design novel structures or improve the performance of existing devices**.

The core goal of this research is to use nanotechnology for altering the properties of bulk silicon and eventually use enhanced properties to built novel devices in a integrated platform.

Based on these set goal, accomplishment of this research are summarized as:

1. **Developed all steps of fabrication process to create high-anisotropic SiNWs using top-down approach, electron beam lithography followed by reactive ion etching. SiNW as small as** $15\ nm$ **to the length of few micrometers have been fabricated by this method.**

2. **Measured polarization resolved reflections from ordered vertical SiNW arrays of different diameters and compared the results to Rigorous Coupled Wave Analysis (RCWA) and Finite Difference Time Domain (FDTD) simulations. Ellipsometric analysis based on anisotropic effective medium approximation was used to fit the experimental data to extract the optical properties of nanowire such as refractive index and absorption loss.**

3. **Conducted a polarization resolved photoluminescence measurements of ordered vertical SiNW arrays. The polarization ratios match well with model based on image forces. As opposed to porous silicon or black silicon, very weak polarization memory is observed in the ordered nanowires and a high polarization memory in disordered nanowires.**

4. **Demonstrated SHG in SiNWs for the first time. While SHG is forbidden in silicon with inversion symmetry, it can be allowed on the surface due to broken symmetry. This discovery introduces potential applications in silicon that were not possible before.**

5. **Demonstrated actual Raman scattering enhancement in SiNW array and implemented a model to describe Raman enhancement in SiNWs. Experimental results show good agreements with theoretical predictions. This model is important, specially in design and simulation of optical devices based on nonlinear Raman effects such as all-optical logic gates and optical bio-sensors.**

6. **Proposed a novel optical waveguide called Silicon Nanowire Optical Waveguide (SNOW). SNOW bridges the gap between the "nanoscopic" and "microscopic" world in that while light interacts with the nano-confined SiNWs, the optical mode resembles that of conventional waveguides, requiring conventional micro-lenses for coupling light in and out of SNOW structures. As a potential application a high-sensitive bio-sensor were designed and simulated based on SNOW concept.**

   During the literature search and course of this study it becomes apparent that the most of the increased material properties in SiNWs are observed only for diameters less than 100 nm, where a single nanowire is a poor waveguide. Thus, photonics devices with an enhanced performance compared to bulk structures were not demonstrated. To overcome this issue, SNO is proposed.

7. **Demonstrate vivid colors in mutually coupled silicon nanowires with diameters ranging from** $105\ nm$ **to** $345\ nm$**. A simple sensor is demonstrated by observing the change in the reflected color with changing refractive index of the surrounding medium. A refractive index resolution of** 5×10^{-5} **is achieved using a simple Charge Coupled Device (CCD) camera.**

The thesis is organized as follows. In Chapter 2, fabrication method developed to fabricate to fabricate SiNWs is described. Fabricated nanowires have highest packing density reported so far (diameter-pitch ratio of 80%) and are among the highest aspect ratio achieved. Similar structures are being fabricated in major groups from Cal-Tech [48], and Harvard [49]. Fabricated nanowires are better or equal to all these groups in all aspects (such aspect ratio, symmetry, length). In addition in this chapter mechanical properties of fabricated nanowires are studied experimentally and theoretically. This study provides guidelines for SiNWs arrays being considered for various applications including solar cells, optical logics, optical waveguides, and sensors. Optical properties of fabricated SiNWs are also measured and presented in Chapter 3. Purpose of this chapter is to to experimentally measure how the optical properties such as reflection, photoluminescence and second and third order nonlinearities change in the nano-regime. Based on these measurement results, one can define where using SiNWs help and where it does not. Based on this research it become clear to us that single SiNW can not provide a high efficient optical device by itself due lack of optical confinement. To fulfill this gap a novel optical waveguide consisting of closely packed arrays of SiNWs on a Silicon-on-Insulator (SOI) substrate are proposed in Chapter 4. It is shown that such a structure can guide an optical mode, provided the electric field is polarized along the length of the nanowires (the same polarization for which enhanced optical interactions are observed in nanowires). Furthermore, the guidance happens even if the nanowires are randomly arranged, albeit with an increased loss. Based on this structure an optical sensor is proposed and discussed in the rest of the chapter. In Chapter 5, a simple sensor is demonstrated by observing the change in the reflected color with changing refractive index of the surrounding medium. Finally, the future work will be described in Chapter 6.

Chapter 2

Silicon Nanowire Fabrication

There are several methods to create semiconductor nanowires including Silicon Nanowires (SiNWs). These methods can be categorized into two main approaches:

1. **Growth (Bottom-Up Approach)** .
2. **Etching (Top-Down Approach)** .

These two approaches will be discussed in the next section.

2.1 Different Approaches for SiNWs Formation

2.1.1 Growth (Bottom-Up Approach)

Vapor Liquid Solid Growth

There are several methods to grow Silicon Nanowires (SiNWs). One of the most common one is Vapor Liquid Solid (VLS). VLS growth is a general method for the synthesis of SiNWs. Using this method SiNWs with accurate physical dimensions and high quality electronic and optical properties can be obtained. In an isotropic crystal such as silicon, growth of nanowires can be obtained provided the growth process is restricted to one dimension. To break the physical symmetry of silicon growth, predefined sites are created for processes. This role can be accomplished by

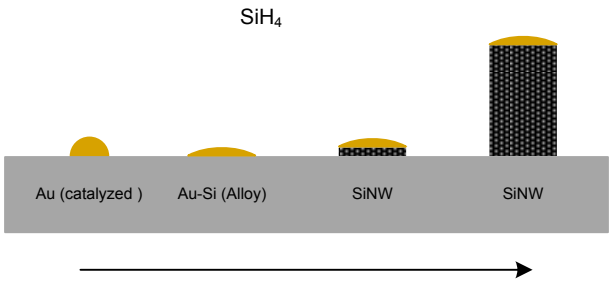

Figure 2.1: Steps of VLS mechanism.

creating nanoclusters or nanodroplets. The VLS method is based on metal nanocluster catalyzed which contains the catalytic material and the semiconductor material. In SiNWs growth process, gold (Au) generally acts as the catalytic material and silane is used as the Si source gas. If the temperature is kept higher than the eutectic temperature of the binary system of Au and Si, some nanodroplet of Au-Si alloy will be formed. During the reaction, silane will alloy with gold nanodroplets and will decompose at the surface. Then the silicon dissolves into the melted gold nanoparticle. The saturation occurs by dissolving more silicon in the gold. Beyond the saturation point excess Si goes out from the liquid phase to form the solid phase of silicon. Steps of process are shown in Fig. 2.1. Further details of process can be found in [50, 51].

VLS method suffers from metal impurities which can be detrimental in devices where photon-electron interaction takes place. In addition, nanowires created by this method are randomly arranged and tend to bunch up. This makes fundamental understanding difficult to ascertain. In the next sub-section a metal free method for SiNWs formation will be described.

Oxide Assisted Growth

In VLS growth process, created nanowires contain metal impurities due to need of metal catalyst. This issue can be overcome by using Oxide Assisted Growth (OAG) method that does not require a metal catalyst. In addition, lower limit for nanowires diameter can be achieved by this method. Nanowires with diameters in range of $6 - 28\ nm$ have been reported by this method [52]. OAG technique also allows for mass production of nanowires. In this method, oxide plays the same role that metal does in VLS growth. Oxides act as sites to start nanowires growth. Key part of the

process is generation of silicon monoxide vapor that can be done either by thermal evaporation [53] or laser ablation [54]. For instance in thermal evaporation case [53], thermal evaporation generates the vapor phase of Si_xO $(x > 1)$ which plays the most important part of the oxide assisted process. The silicon formation occurs in two essential steps as follow:

$$Si_xO \longrightarrow Si_{x-1} + SiO \ (x > 1) \tag{2.1}$$

and

$$2SiO \longrightarrow Si + SiO_2 \tag{2.2}$$

These decompositions happen at temperature of $930°C$ creating nucleation of silicon nanoparticles. These nuclei of silicon are cladded by shells of silicon oxide and act as seeds for growth of SiNWs. Although the OAG does not need metal catalyst, fabricated nanowires were surrounded by a shell of silicon dioxide which affects optical and electrical properties by creating defect states.

Template-Directed Synthesis

Another way of nanowire formation is template-directed synthesis. Size and shape of nanowires are controlled by size and shape of the template. As compared to the previous methods, direct deposition into template typically yields polycrystalline material. However, combining this method with VLS growth can be used to produce single crystal semiconductor nanowires. Template-directed synthesis results in nanowires with good control over diameter and uniformity. In addition, fabrication of multi-layered nanowires [55] is achievable by this method.

Template is typically made of nanoporous materials such as anodized aluminum. Synthesis of nanowires and nanotubes has been proposed using porous aluminum as templates. For example, metal and semiconductor nanowires with diameters in the continuous range 10 to 200 nm were produce by Al-Mawlawi *et al.* [56] via electrodeposition. In a similar way, CdSe nanowire arrays were synthesized by Xu and coworkers [57]. Nanowire growth also can be achieved by Chemical Vapor Deposition (CVD).

As mentioned, there are several methods to synthesize SiNWs. Some difficulties of these methods, encouraging us to try another method, are listed below:

1. **Costly (need MBE or MOCVD)** .

2. **Critical growth process**.

3. **Variation of the growth direction**.

4. **Mostly core-shell configuration instead of pure crystalline nanowire**.

5. **Difficult to grow vertical standing nanowires**.

To overcome these problems in this study, we decide to use top-down approach to fabricate SiNWs which will be described in next section.

2.1.2 Etching (Top-Down Approach)

Like bottom-up approach, there are several approaches to form SiNWs by top-down approach. Here two of these techniques will be discussed.

Metal-nanoparticle Catalyzed Chemical Etching

The most widely used method for Porous Silicon (PS), silicon substrate with pores in surface , formation is the anodic electrochemical dissolution in Hydrofluoric (HF) solution. This method can be extended to create SiNWs using metal particles or films deposited at the Si surface as catalyst. The whole process is shown in Fig. 2.2. Metal particles should be deposited on surface of Si before chemical etching to enhance the Si dissolution. The metal layer can be created by several methods such as thermal evaporation sputtering and electrochemical deposition. As soon as the sample is immersed inside in the HF solution, etching process will start from positions where the metal catalysts exist. The area will etch away and the metal particles sink into substrate. Therefore they will create holes such that the depth start to increase during the etching process.

This method also suffers from uniformity of created nanowires. To have more control over size and shape of formed SiNWs lithography following by Reactive Ion Etching (RIE) methods is the best option. This is our next topic.

Lithography followed by Reactive Ion Etching

The most controlled way of top-down process is using lithography to define a mask pattern followed by RIE. In semiconductor processing lithography is used to transfer

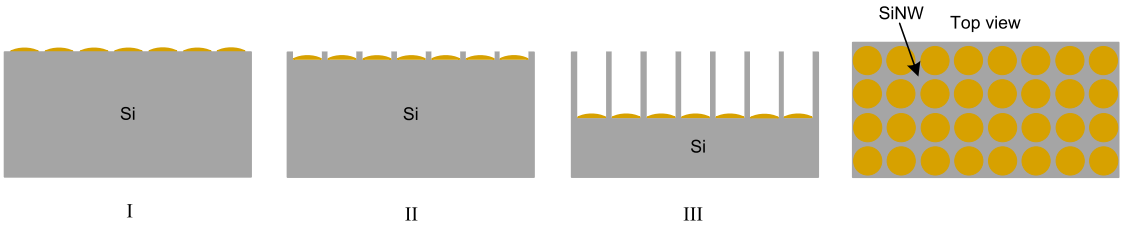

Figure 2.2: Steps of metal-nanoparticle catalyzed chemical etching mechanism.

a design pattern from a mask to a wafer. In typical optical lithography the pattern size is in a few micrometers that is sufficient for most of the applications. However, in nanowire structures, sizes are extended from hundred of nanometer to tens of nanometer pushing us to look for higher resolution methods of lithography. Electron Beam Lithography (EBL) is basic pattern transfer tool used in nanotechnology area. In contrast to optical lithography, resolution in EBL is not limited by diffraction of light but scattering of electrons. As the electron scattering is much smaller than optical diffraction EBL results in high resolution lithography.

After defining the pattern by EBL, the next step is etching. Generally, etching occurs in two directions simultaneously, vertical and lateral. To have a high aspect ratio the vertical etching should dominate. Especially, for nanowire formation since the diameter is in range of nanometer while the length can be few of micrometers there is a need to decrease lateral etching as much as possible. This goal can be obtained by utilizing a highly anisotropic etching in which the lateral etch component is very small resulting in a faithful pattern transfer. On the other hand, diameter and length of nanowires are mostly independent by using anisotropic etching.

In addition to isotropy and anisotropy, another important etching characteristic is the etch-selectivity. Etch selectivity is defined as the ratio between etching rates between two materials at the same etching conditions. There is a huge research interest to develop high anisotropic etching in conjunction with good selectivity between bulk material and mask. As a good example, Henry *et al.* [48] have reported selectivity of $5000:1$ for cryogenic silicon etching and $68:1$ for SF_6/C_4F_8 silicon etching. They used sputtered alumina as a etch mask for fluorine based RIE of silicon to fabricate high-aspect-ratio micro and nanopillars. Nanopillars with diameters ranging from below 50 nm up to several hundred nanometers with heights greater than 2 μm were reported. Micropillars with diameters of 5 to tens of micrometers are etched to heights of over 150 μm with aspect ratios greater than 25. In the next section, we describe the details of our process used to fabricate SiNWs.

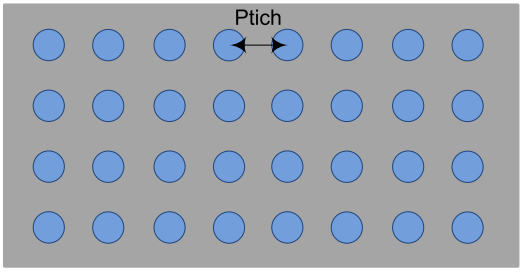

Figure 2.3: Schematic diagram of the design.

2.2 Fabrication of Silicon Nanowire

In order to control the physical parameters, the SiNWs were fabricated with top-down approach using EBL and subsequent etching using Inductively Coupled Plasma Reactive Ion Etching (ICP-RIE). For all the experiments, the nanowires were arranged in a square lattice. E-beam resist, PMMA950-A3, was spun to a thickness of approximately 170 nm and baked at $180°C$ for 20 minutes in an oven. Patterns were written within 20 $kV - 25$ KV electron beam exposure depending on designs. Fig. 2.3 shows a typical pattern including arrays of nano circles with an equal distance from each other called pitch. Dosage was changed for controlling the diameter of the nanowires. The PMMA was developed for 30 sec in a mixture of methyl-isobutyl-ketone (MIBK) and isopropanol (IPA) with ratio of 1:3 followed by dipping in IPA for 30 sec. Then a 30 nm thick layer of aluminum was deposited as a hard mask on the patterned structure by electron-beam evaporation. Lift-off process is accomplished in acetone. The whole steps of nanowire fabrication process are depicted in Fig 2.4. Silicon was etched into nanowires using aluminum as a mask in an ICP-RIE plasma etcher (Oxford Plasmalab 100 $ICP380$) with a gas mixture of SF_6 and C_4F_8. During the etching process, carbon containing polymers were formed on the surface of the nanowires. This side wall passivation was removed after etching through ashing in an oxygen plasma and the removal was verified by measuring the carbon content using energy-dispersive X-ray spectroscopy before and after the ashing showing zero value. SiNW with diameters ranging from 15 nm to several hundred nanometers can be fabricated by this process. For understanding the limitations on the vertical nature of the SiNWs, diameter, pitch and length were varied and the nanowires were analyzed under SEM.

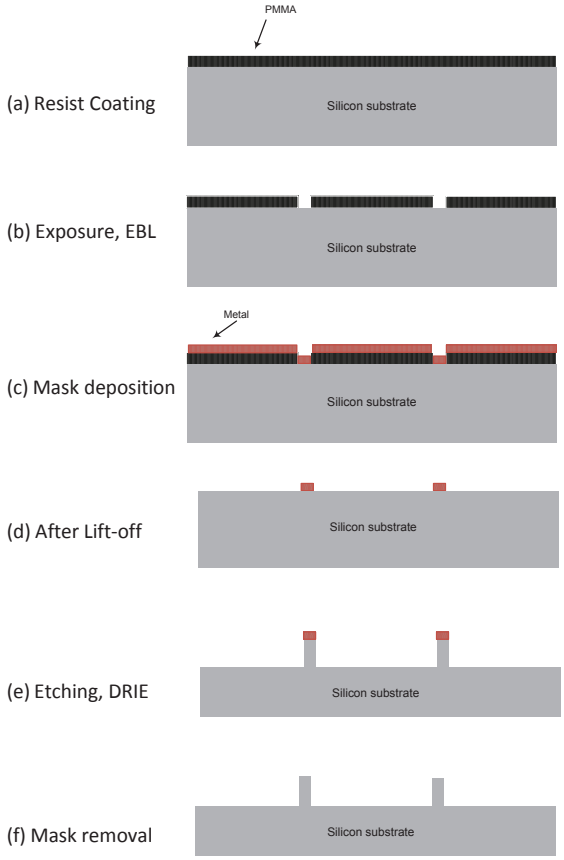

Figure 2.4: Schematic diagram of the lift-off process. (a) Resist Coating (b) Exposure, EBL, (c) Mask deposition (d) After Lift-off (e) Etching, ICP-RIE, (f) Mask removal.

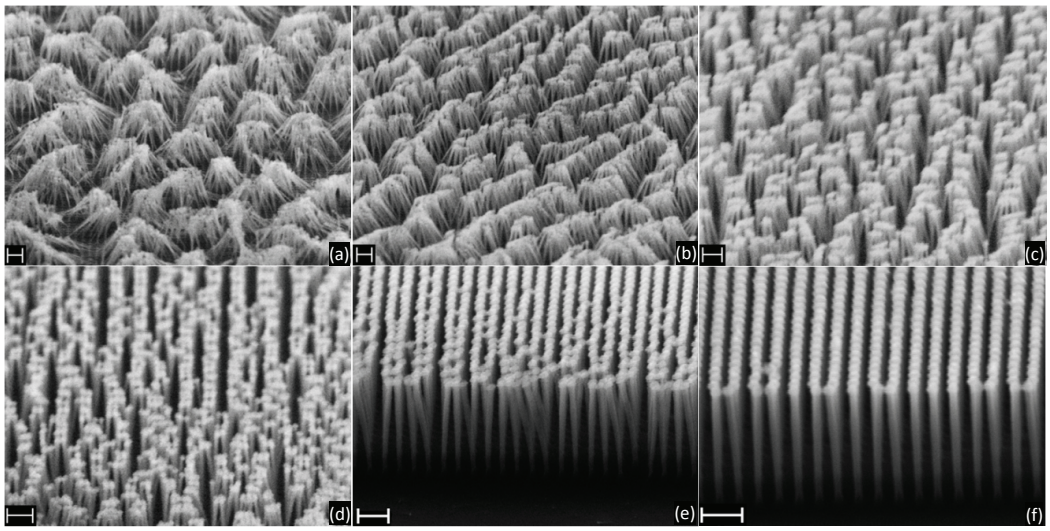

Figure 2.5: SEM images taken at 70 degree angle for nanowires with increasing average diameters (a) 15 nm (b) 20 nm (c) 28 nm (d) 32 nm (e) 37 nm (f) 43 nm. As the diameter is increased, the bunching is reduced and above 40 nm, the nanowires are vertical. The length of the nanowires is 650 nm. All scale bars are 200 nm [1].

2.3 Mechanical Properties of Silicon Nanowires

Since the optical properties are significantly dependent on the physical dimensions and bunching of the nanowires [42, 58], it is important to study which parameters affect the bunching and understand the limitations in diameter, pitch, and length to achieve bunch free arrayed nanowires. In this section, we describe the experimental study of how nanowires bunch as the different parameters such as diameter, length, and pitch are changed. The detailed experimental study provides guidelines for SiNW arrays being considered for different applications including solar cells, optical waveguides, and sensors.

In the first experiment, the diameter of the nanowires was changed from 15 nm to 43 nm. The pitch between the nanowires was 100 nm. The diameters were altered by changing the dose in the e-beam exposure. However, because of the proximity effect during the e-beam exposure and inevitable small lateral change in the mask dimensions, the final diameters do not change in a linear fashion. The average length of the nanowires measured from the SEMs was approximately 650 nm. Figure 2.5 shows the SEM images of the nanowire arrays for different diameters. The images were taken at an angle of 70 degrees to the normal. While the nanowires with diam-

eters larger than 40 nm are fully ordered and vertical, as the diameter is decreased the nanowires bunch together. For the smallest diameter, 15 nm, the nanowires have bunched into conical shape aggregates with an average base diameter of 1200 nm. As the diameter is increased to 20 nm, the conical shape is still maintained but the average base diameter of the conical aggregates decreases to 800 nm. The bunching is further decreased when the diameters are increased to 28 nm and 32 nm, but the nanowires still grab each other. However, for a diameter of 32 nm, conical shapes are no longer achieved. With further increase of the diameter to 37 nm, the nanowires bunch mainly in groups of two between neighboring columns. With further increase in the diameter to 43 nm, the nanowires are perfectly aligned over a large area with no bunching and are vertical. For this diameter, the aluminum mask was etched using PAN solution consisting of $H_3PO_4 : Water : AceticAcid : HNO_3$ 25 : 5 : 2 : 1, at $30°C$ subjecting the nanowires to wet chemistry. No difference in the nanowires was observed after the wet etch, showing that the ordered nanowires can be subjected to wet chemistry without bunching.

Van der Waals forces are normally considered to be the dominant force resulting in bunching of nanowires [59]. In order to understand the role of the van der Waals forces, we considered force laws for this system. SiNWs were considered to be perfectly cylindrical with van der Waals energy dependence given by [60]:

$$W(P) = \frac{AL\sqrt{d}}{24\sqrt{2}(P-d)^{3/2}} \tag{2.3}$$

where L is the length, d is the diameter, P is the pitch and A is the conventional Hamaker constant which was considered to be 19×10^{-20} J for silicon [60]. Van der Waals force ($F = -\partial W/\partial P$) per unit length is plotted in Fig. 2.6 as the diameter of the nanowires is changed. The equation is valid under the approximation that the separation between the nanowires (P-d) is smaller than the diameter of the nanowire. While this is not true for our case, Eq. 2.3 gives an upper bound for the force per unit length and shows similar exponential behaviour as with finite element modeling [59]. As the nanowire diameter is increasing, the van der Waals forces are increasing. However, in Fig. 2.5, the nanowires experiencing the increased van der Waals forces (with larger diameters) are still vertical. Thus the increased forces must be compensated by an increased stiffness in the nanowires.

In order to understand the role of stiffness of the nanowires, the deflection of the nanowires was studied using a Finite Element Model (FEM) by applying a force of 260 $nN/\mu m^2$ on the tip of the nanowire and calculating the deflection. The value of the force was chosen as it has previously been suggested that the total load applied

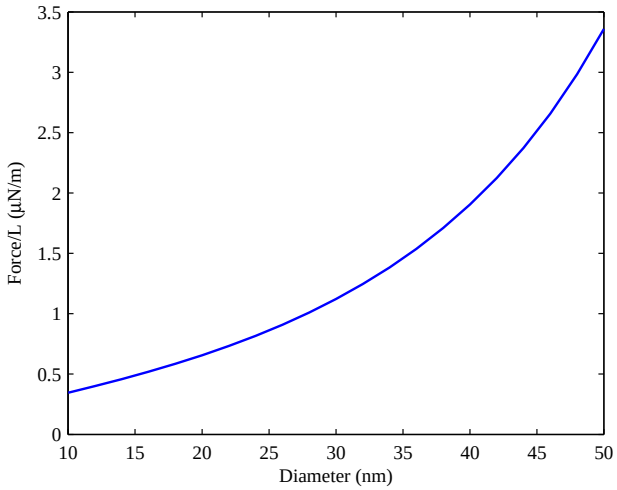

Figure 2.6: Calculated van der Waals force per unit length as the diameter is increased. The pitch is 100 nm. While the van der Waals force increases exponentially with diameter, as seen in Fig. 2.5, nanowires with diameter greater than 37 nm are still vertical whereas nanowires with diameter smaller than 32 nm are bunched [1].

on arrayed nanowires is of that order [29]. The nanowire is taken as a cantilever beam in pure bending with deforming force acting at the free end, in a direction perpendicular to the axis of the wire. The effect of pure bending is to bring the free ends of neighbouring nanowires close together leading to an enhanced force of attraction. The Young's modulus of silicon was taken as 160 GPa [29]. Sensitivity analysis of nanowires of varying diameter and length were conducted to give the trend of variation of maximum deflection at the end of the wire. These trends are shown in Fig. 2.7 for varying diameters with different lengths. It can be seen that the maximum deflection increases exponentially as the diameter of the nanowire is decreased. Further, as the nanowire's length is increased, the inflection point is shifted to larger diameters. The sudden increase in the deflection of nanowires with decreasing diameter suggests that the nanowires will bunch abruptly if the diameter is decreased even slightly from the critical point. In addition, a change in the length results a change in the bunching characteristics. Consequently, this figure suggests that the diameter-length ratio is a crucial parameter for vertical nanowires in an array.

Another experiment was conducted where the nanowires' length was decreased to 400 nm. The pitch was also changed to 75 nm to increase the van der Waals

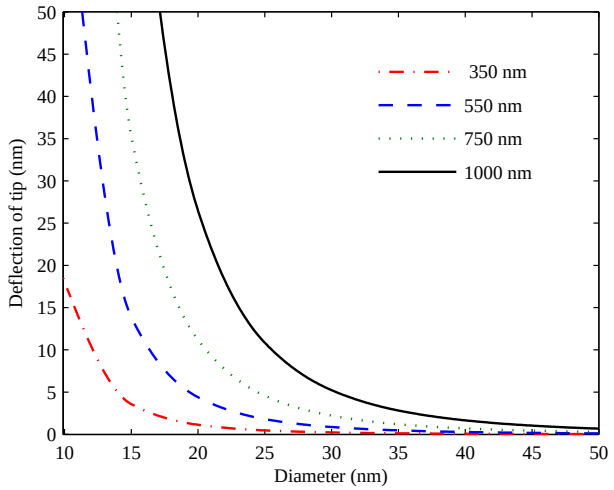

Figure 2.7: Maximum deflection at the end of the nanowire when a 260 $nN/\mu m^2$ force is applied. Different diameters and lengths for the nanowires are considered showing exponentially increasing deflection below a certain diameter. The inflection point in the diameter increases rapidly with increasing length [1].

force. Figure 2.8 shows the SEM images of nanowires with diameter of 34 nm for two different lengths of 400 nm and 650 nm. The top view perspective was chosen for ease of characterization. While the 400 nm long nanowires are vertical, the 650 nm long nanowires bunch into conical shapes. Also a few nanowires of 400 nm length bunch in groups of two, suggesting that 34 nm is the critical diameter between the bunching and vertical phases for these nanowires. For the 650 nm long nanowires, when the diameter was 42 nm, the nanowires were vertical similar to Fig. 2.5f where the pitch was 100 nm. This suggests that the diameter-length ratio plays a more important role as compared to the pitch between the nanowires.

In order to evaluate the essential effect of the diameter, a sample was created where the diameter of the nanowires was incrementally increased for different columns of the array from 25 nm to 50 nm. The pitch between the nanowires and the length were 75 nm and 400 nm, respectively. Figure 2.9 shows the SEM image taken normal to the sample. Interestingly in this figure, the interface between vertical and bunched nanowires is abrupt. Nanowires with diameters larger than 34 nm are vertical whereas the ones with diameters less than 32 nm are bunched. The abrupt nature of the change in the phase from bunching to vertical standing mirrors the understanding from the simple deflection studies shown in Fig. 2.7.

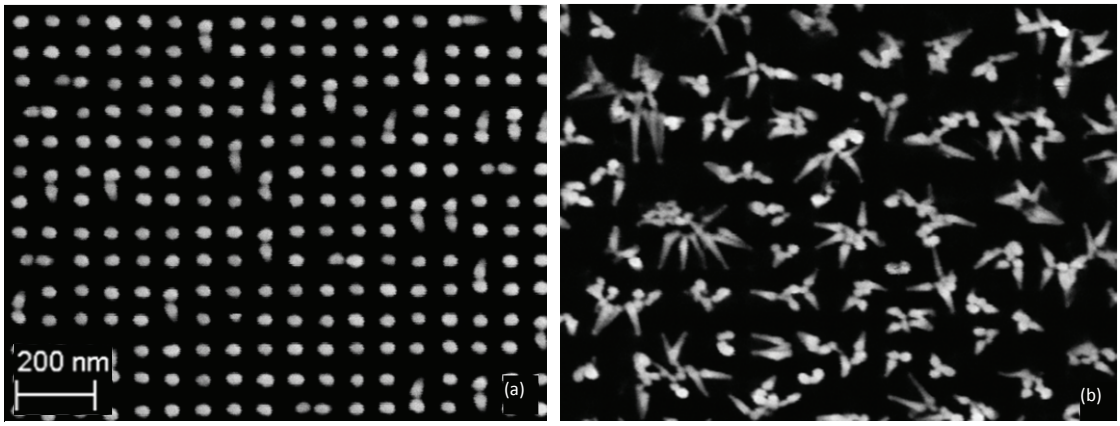

Figure 2.8: SEM image at normal incidence for a diameter of 34 nm for a length of (a) 400 nm and (b) 650 nm. Pitch between the nanowires is 75 nm [1].

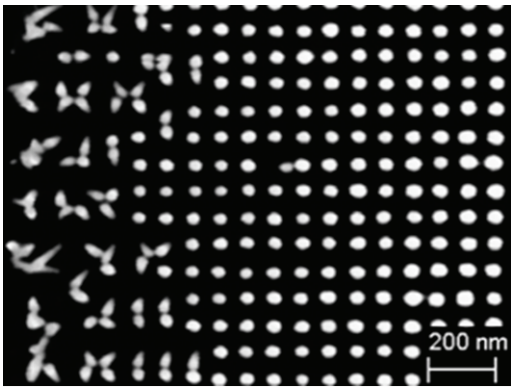

Figure 2.9: Top view of the nanowires with length of 400 nm as the average diameter is increased gradually from 25 nm to 50 nm. Nanowires with diameters greater than 34 nm are vertical whereas the ones with diameter below 32 nm bunch. An abrupt transition is observed [1].

In a regular array, the force acting on a nanowire is symmetrical because of the neighbouring nanowires. Hence, one will normally expect the nanowires to be vertical due to the balancing of the forces. However, as one goes towards the edges of the arrays, the balance of the force is broken and nanowires may bunch. While in the bulk of the area, nanowires are standing vertically, the nanowires at the edges and the corner are leaning inwards. We also studied the edge effect on the bunching with increase in diameter. The SEM image taken at normal to the substrate is shown in Fig. 2.10. The array area is $10\mu m \times 10\mu m$. The pitch between the nanowires is 100 nm and the length is 400 nm. In these arrays, the diameter of the nanowires on the outside was approximately 10 % smaller than of ones on the inside due to the proximity effect. The pattern was created using a dot dosage to create a hole in the PMMA which was filled with metal using e-beam deposition and lift-off. The exposure times were corrected for achieving the desired diameter in the bulk of the array. However, at the edges, there was less scattering of electrons due to fewer number of neighboring pixels. Thus, for the same exposure time, a smaller hole and a reduced diameter nanowire was achieved after etching. It was observed that when the nanowires' diameter is 24 nm in the middle (Fig. 2.10(a)), the nanowires all over the array are bunched. As the nanowires' diameter is increased to 35 nm (2.10(b)), they are bunched around the edges while are vertical in the center. Since 35 nm is the critical diameter and the nanowires on the outer edges are smaller than this diameter, they are expected to bunch. With further increase in the diameter to 53 nm (2.10(c)), the edge effect is reduced but the nanowires are still bunching at the corners where force balancing does not hold. Here, the diameter is larger than 45 nm even at the edges. This suggests that force balancing also plays a role in keeping the nanowires vertical in the arrays. As the diameter is increased to 68 nm, the nanowires are vertical all over the array with minimal edge effect observed Fig. (2.10(d)). For this diameter, the nanowires were vertical even over a large area of 400 $\mu m \times 400$ μm. Further, for the nanowire arrays at the edges the lean of the nanowires is directly towards the expected net force. This is shown in Fig. 2.11 for an array where the corner has been imaged. It can be clearly seen that in the corners, the nanowires are leaning diagonally inwards, while in the sides, they are leaning normally into the sample. This suggests that while the nanowires in the middle are being balanced by the neighbouring SiNWs, if a disordered array with similar average diameter and pitch was created, it could still bunch up as the force will not be balanced. For disordered nanowires of length 400 nm, the diameter will need to be larger than 60 nm for the bunching to be reduced. For an ordered nanowire array, one may also place larger diameter nanowires at the edges for increased stiffness to reduce the edge effect. The symmetry of forces is present even for the smaller diameter

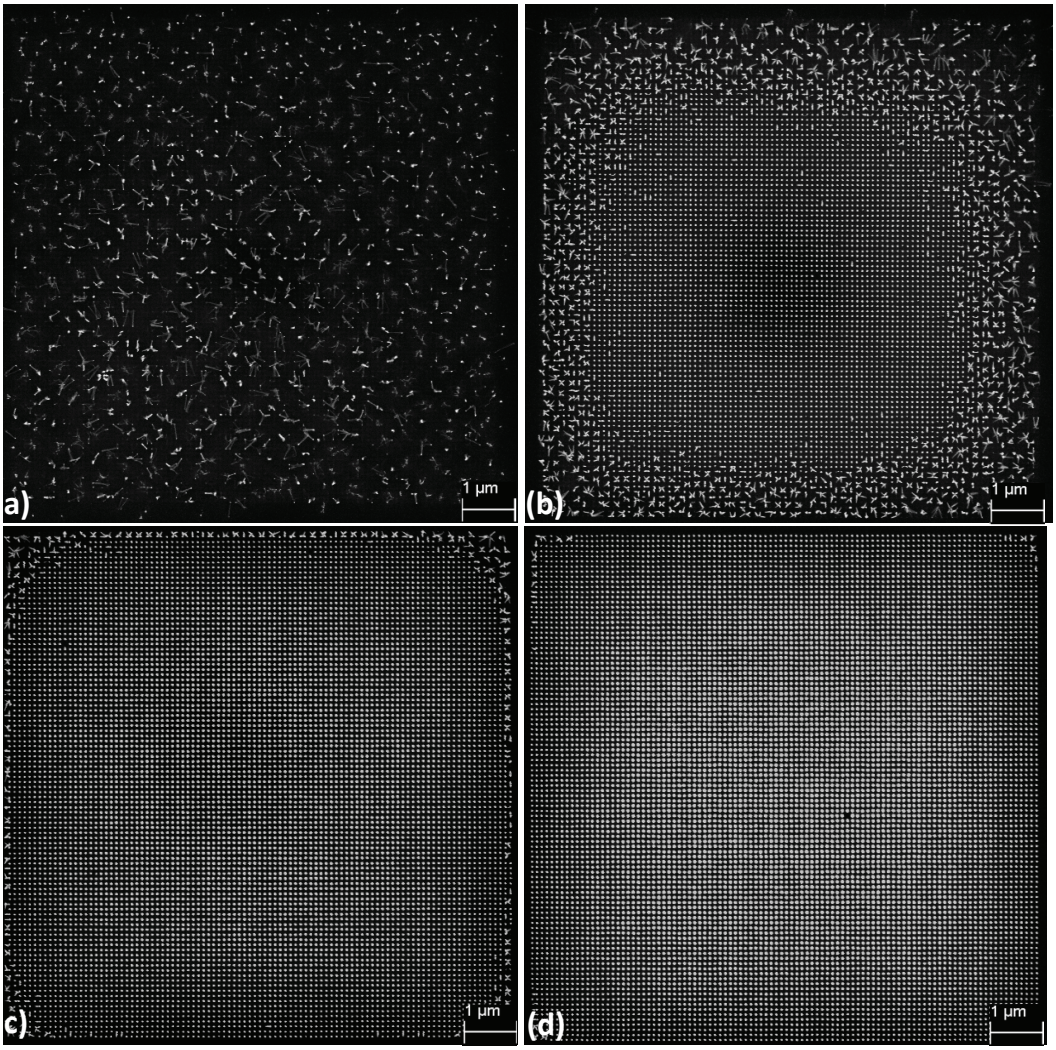

Figure 2.10: SEM image of $10\mu m \times 10\mu m$ arrays of SiNWs as the average diameter at the center of the array is changed from (a) 24 nm (b) 35 nm (c) 53 nm (d) 68 nm. Pitch is 100 nm. Length is 400 nm [1].

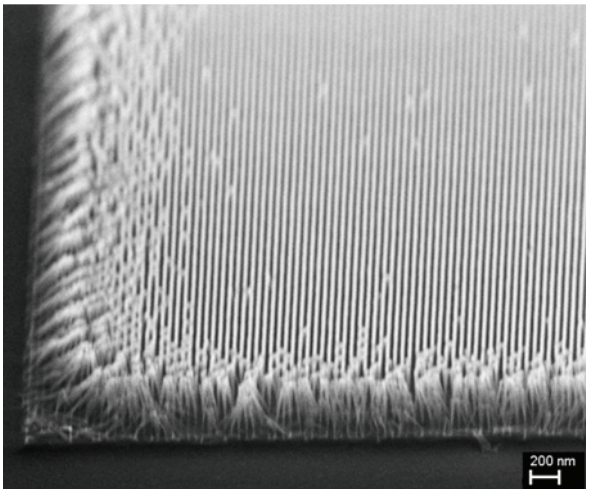

Figure 2.11: SEM image at the corner of array. Nanowires at the corner are falling inwards diagonally whereas nanowires on the sides are falling normally into the sample [1].

nanowires such as the ones in Fig. 2.5(a)-(c) and one could expect the possibility of an ordered array. However, due to random thermal vibrations, the symmetry in the van der Waals forces can be broken. As the thermal vibrations bring some nanowires randomly close together, van der Waals forces between them increase, resulting in a net force and bunching of the nanowires. Since this is a stochastic process; we believe this causes the conical structures in Fig. 2.5, which vary with diameter.

In this chapter, we discussed the fabrication processes to make high aspect-ratio SiNWs using EBL followed by ICP-RIE etching. In addition, SiNWs mechanical properties were parametrically studied by varying the diameter, the length, and the pitch. We showed the importance of the diameter-length ratio for keeping the nanowires vertical. The detailed experimental study is is important to design SiNWs array for wide rang of applications. In next chapter, we will investigate optical properties of these SiNWs.

Chapter 3

Optical Properties of Silicon Nanowires

In this chapter, we experimentally investigate how the optical properties of Silicon Nanowires (SiNWs) such as reflection, photoluminescence and non-linear effect including second harmonic generation and Raman scattering change as compared to those of bulk silicon.

3.1 Polarization Resolved Reflection from Ordered Vertical Silicon Nanowire Arrays

SiNWs have been considered for their reduced reflection and increased absorption in the solar spectrum [61]. Optical properties of SiNWs such as absorption and reflection have been previously calculated with varying diameters and lengths [42]. However, experimental verification of the models has not been conducted. Increased absorption has been shown experimentally in [43] but physical understanding is still not clear. In Seo *et al.* work [49], different colors from nanowire arrays with varying diameters ranging from 45 nm to 70 nm were observed and explained using guided modes within individual nanowires. Unpolarized reflection measurements were conducted at normal incidence and compared to simulated values. In their work, the arrays were sparsely populated with a pitch of 1 μm. Since the nanowire arrays are expected to have a different reflection value for light waves polarized parallel or perpendicular to the length, normal measurements do not give complete information on the reflection

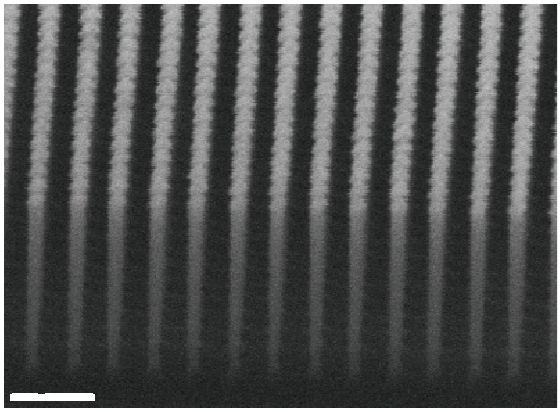

Figure 3.1: SEM image taken at 70 degrees angle for nanowires with an average diameter of 38 nm. The length of the nanowires is 375 nm. Scale bar is 200 nm [2].

behavior of the arrays. Ellipsometric measurements were conducted in [62] and effective medium approximation (EMA) was used to model disordered silicon nanowires to fit the experimental data. These results are in contrast with the theoretical calculations in [42] where it was shown that at least for ordered nanowire arrays, EMA does not work well. In order to fill these gaps, in this section, we measured the polarization resolved reflection at an incident angle of 65° from highly ordered SiNW arrays of different diameters and showed good agreement with simulations. The simulations were carried out by means of a Rigorous Coupled Wave Analysis (RCWA). We also showed that depolarization of light occurs at shorter wavelengths in which EMA fails. However, for longer wavelengths, ellipsometric measurements provide a good agreement in diameter and length of the nanowires with Scanning Electron Microscope (SEM) measurements.

A (100) Si wafer was used as the starting substrate. Highly ordered vertical SiNWs arranged in a cubic lattice were achieved. For the present experiment, two different average diameters, 38 and 45 nm, were considered. The pitch between the nanowires was 100 nm and the length of the nanowires from SEM images was in the range of 375 $nm - 390$ nm. The array size for each diameter was 100 $\mu m \times 100$ μm. Figure 3.1 shows the SEM image for SiNWs with an average diameter of 38 nm and a length of 375 nm. Polarization resolved reflections were measured at wavelength of 230 nm to 1000 nm using a focused beam with a J. A. Woollam M-2000 ellipsometer. The incident angle for the measurements was 65°. The spot size was approximately 25 $\mu m \times 60$ μm. In order to study the depolarization by the SiNW arrays due to coherent patterning effects, total reflected powers and reflected powers only in the

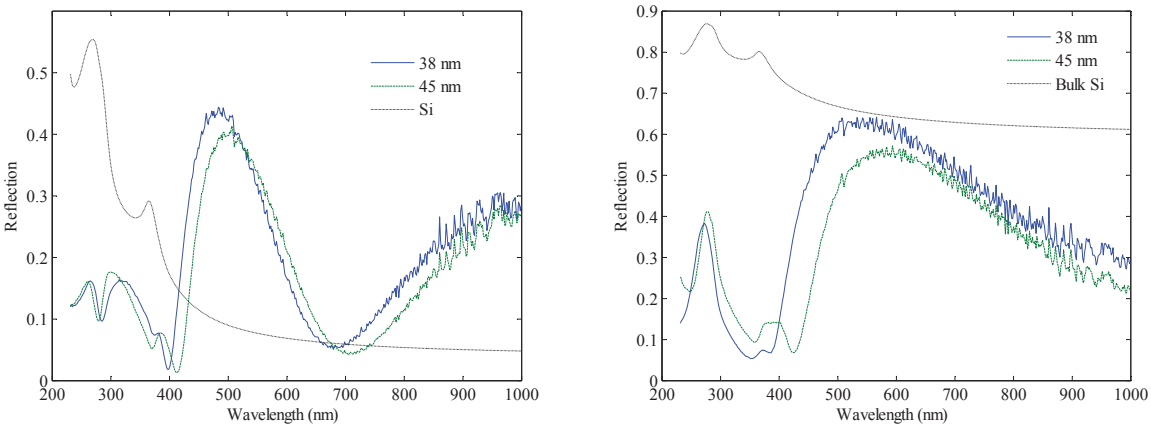

Figure 3.2: Total reflection intensity from SiNW arrays with diameters of 38 nm and 45 nm for, **Left**: p-polarized input and, **Right**: s-polarized input. Dotted lines show the simulated reflection for bulk silicon [2].

same polarization as the input were measured.

Figure 3.2 shows the total reflected intensity in the p- and s- polarization for two arrays with different diameters. A reflection peak in either polarization is observed between 450 nm to 600 nm. As the diameter increases, the reflection intensities at higher wavelengths decrease slightly and the peak shifts slightly to longer wavelengths for either polarization. This is opposite of what one would expect as the silicon volume is increasing. Further, the reflection intensities are higher in the s-polarized input as compared to the p-polarized input. Since the sample consists of SiNW arrays on top of bulk silicon, multiple reflections are created at the air-SiNW interface and the SiNW-silicon interface which may interfere constructively or destructively as the input wavelength is changed. Theoretical reflections from air-silicon interface are also shown in the figures for both polarizations for comparison. The reflection from the SiNW arrays is quite different from that of silicon. While the reflection from the s-polarized beam reduces with SiNWs for the complete range, for p-polarized input the reflection increases for wavelengths greater than 400 nm. It is seen in Fig. 3.2 that there are wavelengths at which the reflection reduces considerably and these troughs are dependent on the diameter.

Figure 3.3 shows the comparison between the total reflected intensity and the reflected intensity in the same polarization as the input for the array with the diameter of 38 nm. While the reflected intensity is minimally depolarized above the wavelength of 400 nm, it shows significant depolarization below this wavelength. As the

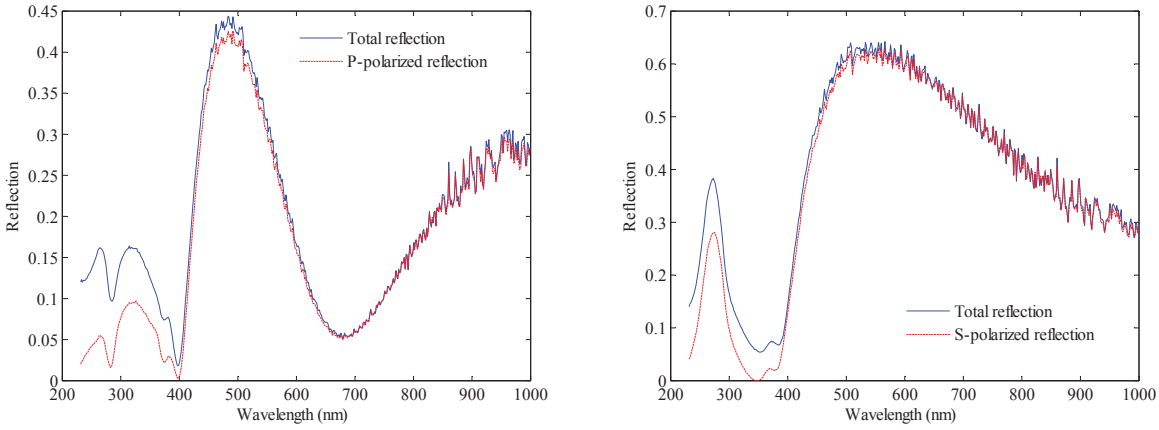

Figure 3.3: Total reflection and reflection in the same polarization as the input for, **Left**: p-polarized input and, **Right**: s-polarized input. Depolarization is observed below 400 nm [2].

wavelength is decreased, the diameter to wavelength ratio increases and the pattern dependent effects of SiNW increase considerably resulting in the depolarization. Similar results were also obtained for the array with nanowires with a diameter of 45 nm. Since minimal depolarization is observed above 400 nm, EMA should work well over this range. This was confirmed using an ellipsometric measurement described by two parameters, Ψ and Δ given by:

$$tan(\psi)e^{i\Delta} = \frac{R_{pp}}{R_{ss}} \tag{3.1}$$

where R_{pp} and R_{ss} are the complex Fresnel reflection coefficients of the sample for p- and s-polarized input light, respectively. Figure 3.4 shows the comparison between the experimental value and the value obtained from anisotropic EMA model [62]. Unlike [62], the SiNW structures were well-defined and did not require index grading versus depth into the film, as the same EMA void fraction is consistent from bottom to top of the nanowires. Nanowires' diameter and length were determined from the EMA model, relating to the fitting parameters of EMA void % and layer thickness, respectively. Best fit diameters of 37.8 nm and 43.7 nm and a length of 374 nm were obtained. The diameters and lengths are in agreement with SEM measurements of average diameter of 38 nm and length range of 375 $nm - 390$ nm. Good fits between the EMA and the experimental data shows that EMA can be effectively used to simulate nanowires above the wavelength where depolarization is negligible.

The extracted anisotropic refractive indices are plotted in Fig. 3.5 . For both

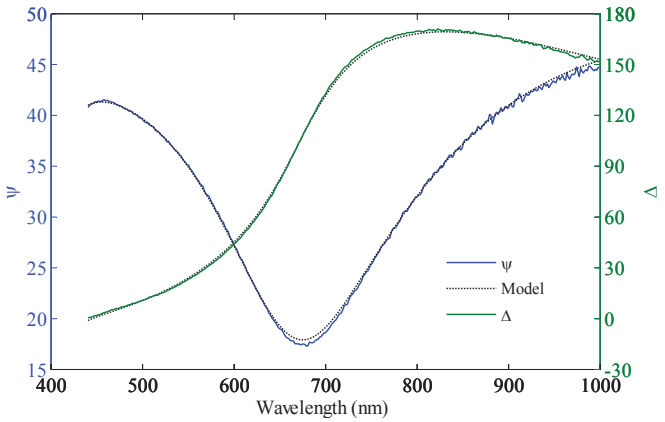

Figure 3.4: Experimental and modeled generated fits. EMA model is used to represent the SiNW arrays [2].

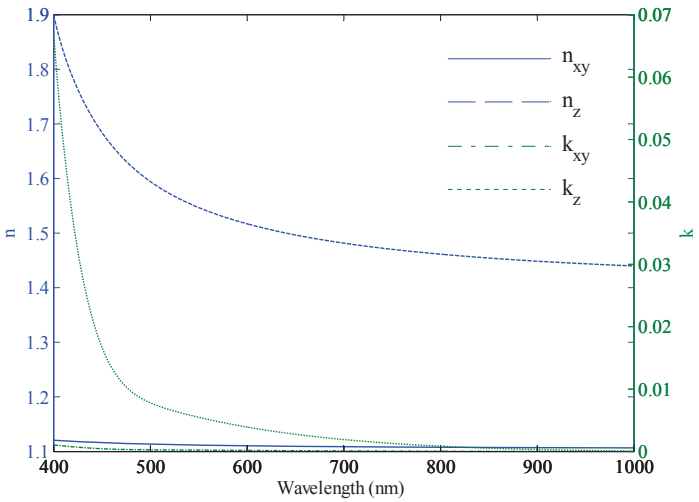

Figure 3.5: Anisotropic refractive index and absorption coefficient for the nanowire arrays of diameter 38 nm [2].

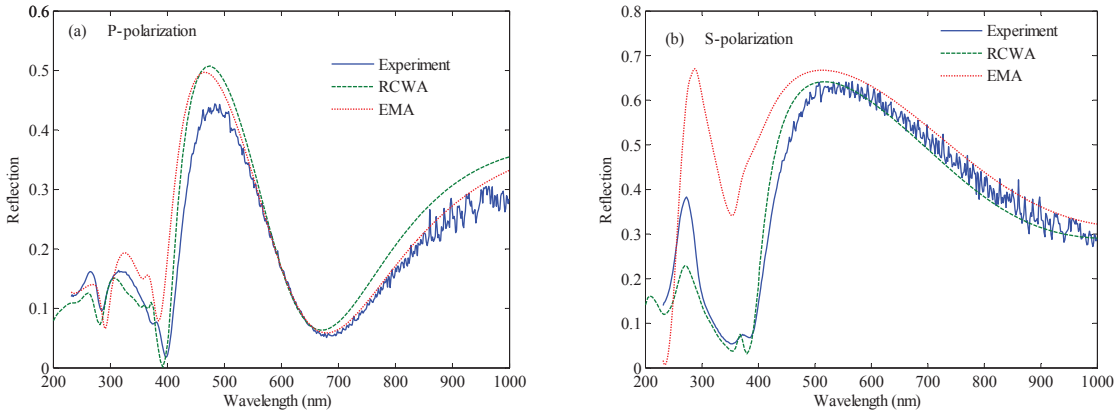

Figure 3.6: Experimental and modeled reflections for the array with SiNWs of 38 nm diameter for (a) p-polarized input (b) s-polarized input [2].

the real and imaginary part (the absorption coefficient), the values are higher when the electric field is polarized along the length of the nanowires (z-direction in the figure). The effective index for the perpendicular electric field (x, or y direction) is around 1.11 for nearly the complete range from 450 nm to 1000 nm. This should result in low reflections for the s-polarized beam. However, the absorption coefficient also decreases appreciably in this polarization compared to the parallel polarization. No light trapping is evident above the wavelength of 450 nm. Thus, the reflections seen from the bottom silicon surface are observed more in the s-polarized light where the electric field is perpendicular to the nanowires, increasing the total reflections observed. Constructive and destructive interferences between the top and the bottom reflections as the wavelength is changed create the frequency dependent features.

The SiNW arrays were simulated using a commercial RCWA technique [63]. Periodic boundary conditions were used in the transverse directions to decompose the SiNW array into a single periodic cell. SiNW of the given diameter and length of 375 nm were placed on top of a semi-infinite bulk silicon layer. Perfect matching layers were used at the top and bottom boundaries. Figure 3.6 shows the modeled and experimental data for p- and s-polarized inputs. Modeled data from EMA is also shown. For s-polarized beams, an excellent agreement is achieved above 300 nm whereas for p-polarized beams, the maximum modeled reflection is slightly higher as compared to the experimental values. However, the peak wavelength and the features in the reflection are fully observed. The higher reflection in the simulation could be due to the fact that the actual nanowires may be slightly conical in shape, tapering at the top as compared to the modeled cylindrical shapes. The tapering

could be due to the etching process. To our knowledge, this is the first time good agreement between experimental and modeled reflection values has been obtained for ordered SiNW arrays. In conclusion, polarization resolved reflections were measured and compared well to RCWA models. Good agreement was achieved between the experimental results and the simulated values. Depolarization of reflected light was observed below the wavelength of 400 nm. Above this wavelength, ellipsometric models based on anisotropic EMA fit well to the measured results. Diameters and lengths extracted from the ellipsometric fits compared well to the SEM images suggesting that spectroscopic ellipsometry could be used to characterize SiNWs.

For this experiment, the diameter and the length were small. Some of the results that we achieved were opposite of what other groups reported. It was not clear whether the discrepancy was due to nanowire diameters or length. This is the subject of the next section.

3.2 Polarization Resolved Reflection For SiNWs with Longer Length and Larger Diameters

For this study, SOI wafer was used as a starting substrate. The SOI wafer has 1.5 μm thick top silicon layer and 3 μm thick buried oxide layer. All the nanowires have a length of 1 μm. Figure 3.7 (a) and (b) plots the s-polarized reflections against wavelength for the different diameters. Reflections from the side of the arrays with no nanowires are also plotted for reference. The reflections achieved are exactly what are expected from a smooth silicon surface, showing that after etching the bottom interface is optically smooth. Reflections from nanowire arrays are significantly different than the reflections from silicon, and differences are also seen as the diameter of the nanowire is changed. For diameters 130 nm and smaller, at longer wavelengths (> 700 nm) the reflections approach that of silicon. As the diameter is increased further, oscillatory behavior similar to Fabry-Perot peaks is observed with increasing number of longitudinal modes and decreasing wavelength spacing seen with increasing diameters. There is a sudden decrease in reflections seen at different wavelengths for different diameters, and this sudden decrease is more apparent in the smaller diameters. This sudden change shifts towards the higher wavelengths as diameter is increased. The peak reflection values also decreases as diameter increases. For the diameter of 130 nm, strong reflection peaks are observed at wavelengths of 504 nm and 557 nm. The nanowire arrays are sandwiched between air and silicon surface below. The reflections should come from the interactions of the reflections from the

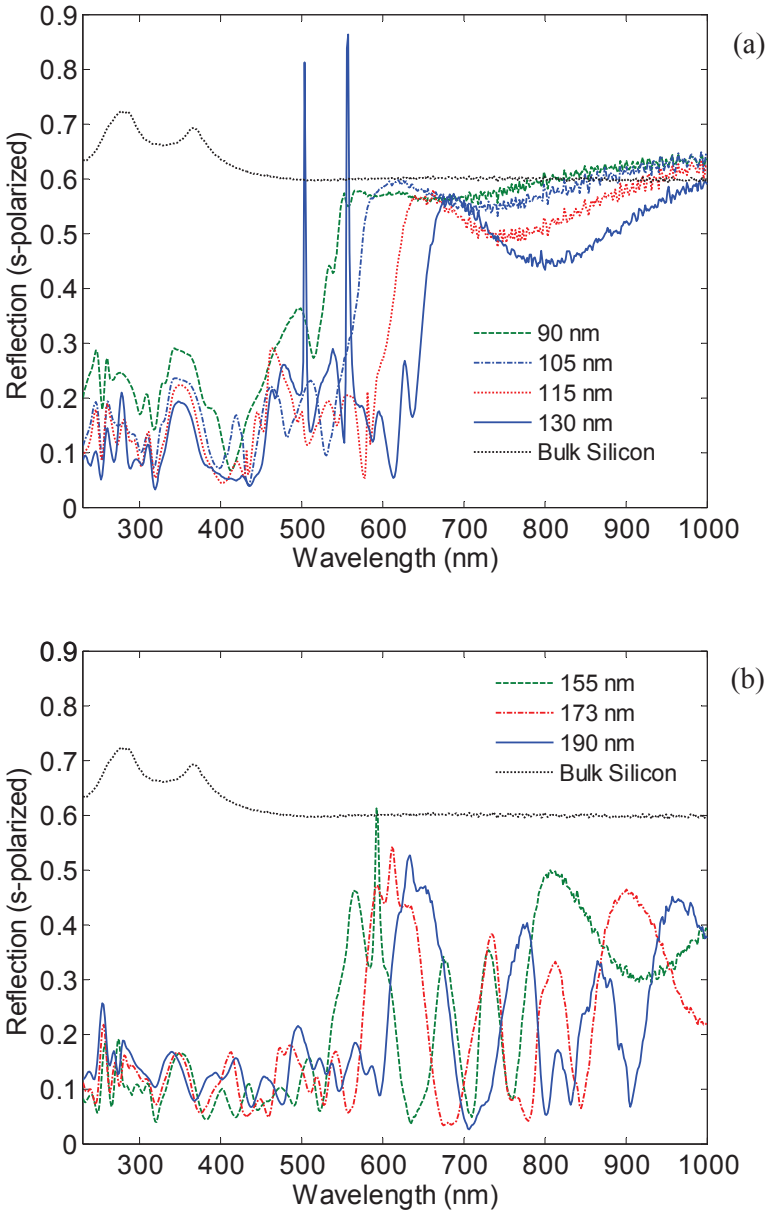

Figure 3.7: S-polarized reflections versus wavelength for diameters of (a) 90 nm to 130 nm (b) 155 nm to 190 nm. Reflections from the side of the wafer with no nanowires is also shown for reference.

top surface and the bottom surface along with any light absorption seen within the nanowires. Thus, by measuring these reflections, we should be able to investigate the optical properties for the nanowires. For example, at longer wavelengths the absorption for the nanowire arrays is very low allowing the light to penetrate through the nanowires and be reflected back from the back silicon surface. This could be the reason for the measurements to approach that of silicon surface at these wavelengths. Further discussion of this figure is considered when we discuss the model.

Fig. 4 3.8 (a) and (b) show the p-polarized reflections with wavelength for the different diameters. The values for the reflections from the side of the arrays are also plotted. Again the reflections obtained are quite different compared to the bulk silicon. However, as opposed to s-polarized beam the reflections at longer wavelengths are higher than bulk silicon and even for smaller diameters show oscillatory behavior. This suggests that the reflections from the SiNW-air interface are larger in the p-polarized beam as opposed to the s-polarized beam. In previous section, we have shown a higher value of effective refractive index for the electric field polarized in the direction parallel to the nanowires. This component is present in the p-polarized beam and hence, we observe higher reflections. Also as the real part of the refractive index is also higher, the Fabry-Perot spacing, $\Delta\lambda$, given by $\Delta\lambda = \frac{\lambda^2}{2ln_g}$ where λ is the free space wavelength, n_g is the group index, and l is effective length of the cavity, is smaller than the s-polarized beam for the same diameter. Thus, we observe more oscillatory behavior in the p-polarized beam. The sharp reflections observed in the s-polarized reflections at 504 nm and 557 nm, are also observed in the p-polarized beam for the diameter $130nm$. Once again, the distinct features seen in the reflection shift towards higher wavelengths as the diameter is increased. Also the number of modes increase and the wavelength spacing between the peaks decrease as the diameter increases. Both s- and p-polarized reflections show a presence of strong Fabry-Perot interferences with increasing diameter, showing that the light is interrogating the bottom silicon surface well. While there are wavelengths where the s- and p-polarized reflections are low and nearly similar in either bunched or vertical nanowires, over the whole band the values could be quite different. This contradicts the conclusions made in [64] where the reflections were measured at one wavelength for bunched nanowires and it was concluded that the SiNW arrays have omni-directional reflection spectrum. While this is true for certain wavelengths as seen in Figs. 3.7 and 3.8, it is not true generally over the complete band.

In order to understand these results, a theoretical model was conducted. In previous models [42, 58], nanowires with cover and substrate are considered in the simulations. Thus, the results are not only affected by electromagnetic coupling between the nanowires but also by Fabry-Perot interferences. Since the silicon properties

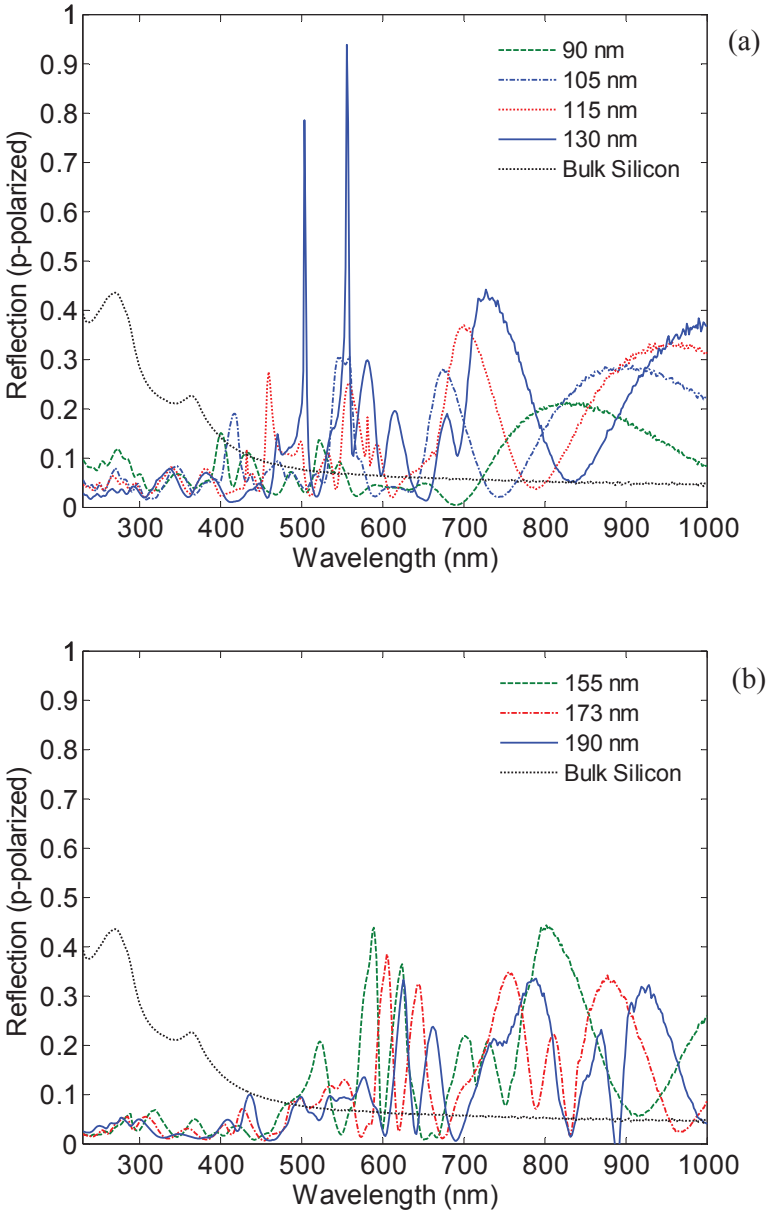

Figure 3.8: P-polarized reflections versus wavelength for diameters of (a) 90 nm to 130 nm (b) 155 nm to 190 nm. Reflections from the side of the wafer with no nanowires is also shown for reference.

change over the wavelength range between the Fabry-Perot peaks, it is difficult to ascertain the role of coupling versus interference in the reflection spectrum. As such, we modeled semi-infinite nanowires with FDTD. For the current model, we have only done normal incidence and hence, the results are valid for only s-polarization beams. S-polarization is of interest to solar cell applications. A plane wave is incident on the top of the nanowires. Part of this wave is reflected while the other part starts to propagate through the nanowires. Periodic boundary conditions are used to consider the array as a unit cell. Perfectly matched layer boundary is considered at the bottom of the nanowires to achieve the semi-infinite condition. Figures 3.9 (a) and (b) plot the simulated reflections and transmission after a length of 450 nm for different diameters. In all these diameters, we see a reflection peak which changes in value and position depending on diameter. As the diameter is increased, the reflection peak increases and shifts towards longer wavelengths. Further, the reflection peak has a resonance like bandwidth suggesting it may arise from the coherent coupling between the nanowires. From these results, one can extract the effective refractive index, n and absorption coefficient, k, for the nanowire arrays. The idea is to replace the nanowires with a bulk medium with an effective refractive index and absorption coefficient to have the same optical parameters as the nanowire arrays. The reflection, R and transmission T, are given by the following:

$$R = (((n-1)^2 + k^2)/((n+1)^2 + k^2)) \tag{3.2}$$

$$T = (1-R)exp((-4\pi kl)/\lambda) \tag{3.3}$$

where λ is the free space wavelength, n is the real part of the effective refractive index, k is the effective absorption coefficient, and l is the length of the nanowires. By calculating R and T, k can be easily determined from equation 3.3 and once k is known, n can be determined through equation 3.2. The value of n and k are plotted for different diameters against wavelength in Fig. 3.10 (a) and (b), respectively. Values for bulk silicon are also plotted in the same chart for reference. It is observed that k values for nanowire arrays can be higher than bulk silicon but only over small wavelength regions. Where there are peaks in absorption coefficient, there are also peaks in effective refractive index, so both reflection and absorption are increased at these wavelengths. Beyond these peaks, the effective refractive index and absorption is significantly lower than bulk silicon and hence, both the reflections at the nanowire-air interface and absorption through the nanowires are decreased at these wavelengths. The peaks are where coherent coupling between the nanowires occur resulting in increased optical confinement within the nanowires. Similar coupling has

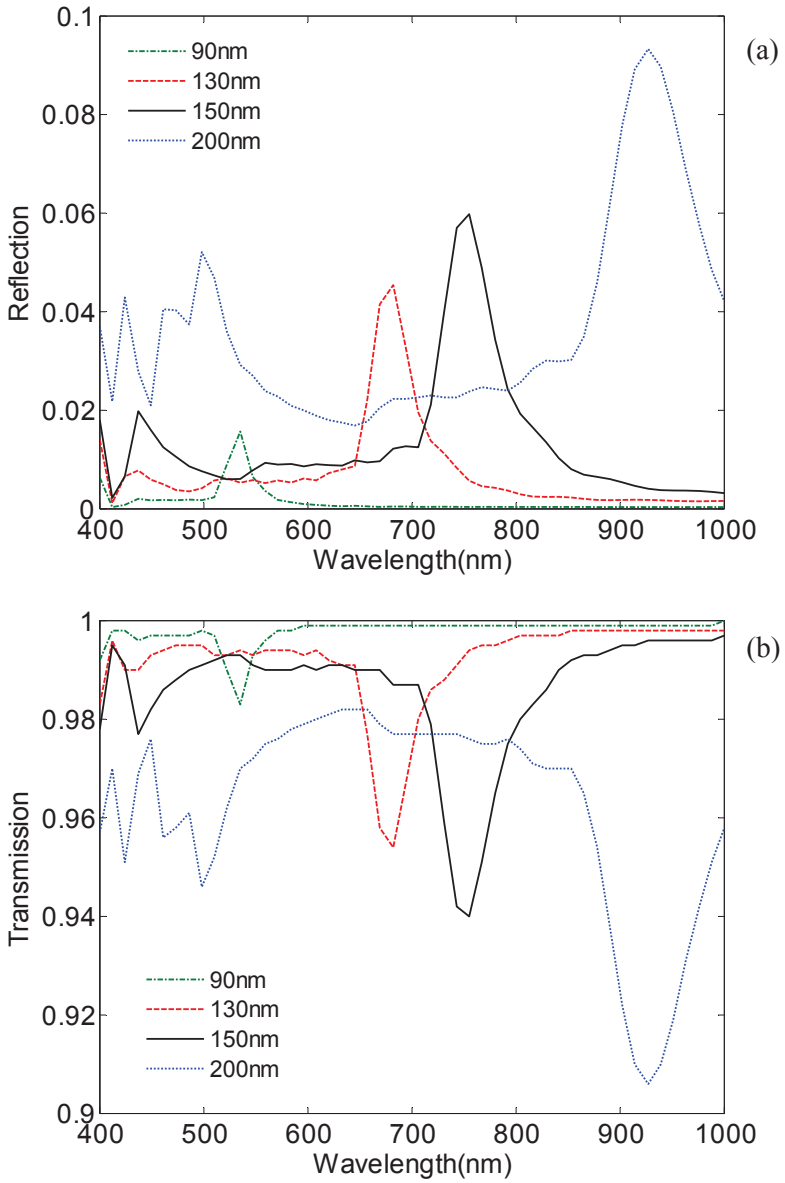

Figure 3.9: (a) Reflection and (b) transmission through 450 nm length of silicon nanowires for different diameters.

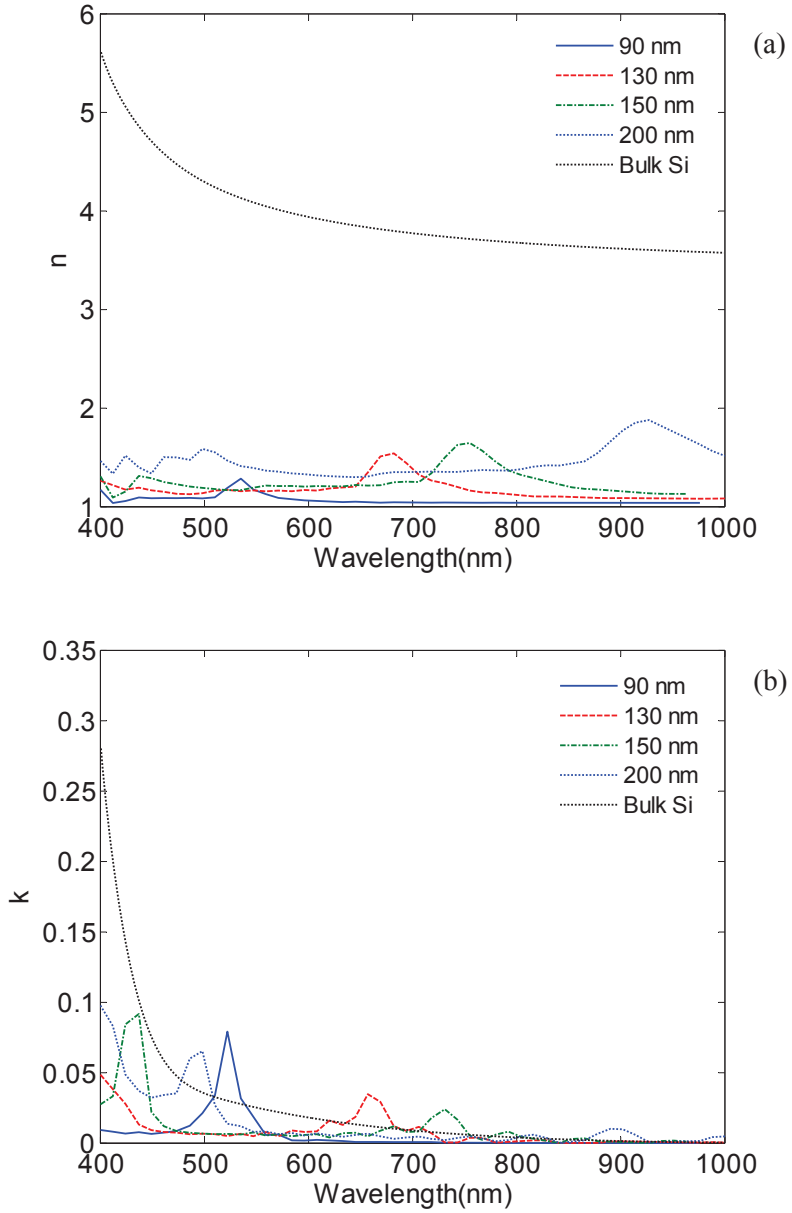

Figure 3.10: Calculated (a) refractive index, n and (b) absorption coefficient, k for different diameters against wavelength.

previously been used in vertical cavity surface emitting laser arrays to generate high intensity spots from multiple lasers [65]. As the diameter is increased, the peaks shift to longer wavelengths and the value of the absorption coefficient at the peak becomes lower because the absorption coefficient of the constituent silicon in the nanowires decreases with longer wavelength. The full-width-half-maximum of these spectral peaks range from 22 nm to 39 nm for the different diameters. If we consider 1 μm long nanowires and bulk silicon with no back reflections, for the diameter of 130 nm at the absorption peak, the absorption from the nanowires is 1.8 times that of the bulk silicon. From these simulations, it is seen that ordered nanowires efficiently trap light only over a small wavelength region, and this wavelength can be tuned by diameter. One advantage of our method is that the simulation we use does not have multiple passes and hence, can be done quickly. This can allow the nanowires to be represented as a bulk material and the calculations of actual structures can be done semi-analytically. Further, the effective values provide a very good understanding of the nanowire material. The results from the calculated absorption coefficient, k, can be used to analyze the reflection features seen in the s-polarization. Figure 3.11 (a)-(c) plot the absorption coefficient and s-polarized reflections overlaid on each other for three different diameters. For diameters of 90 nm, and 130 nm, the abrupt decrease in the reflection is observed right at the place where the absorption peak is present. For 190 nm diameter, there is no absorption peak observed above 600 nm wavelengths and Fabry-Perot resonances are observed in the reflection spectrum. If the absorption increases within the nanowires, light reflected from the backside silicon is reduced. The abrupt changes in the reflection spectrum are observed because coupling that occurs due to the order of the nanowires creates sharp absorption features. For longer wavelengths and smaller nanowire diameters, the refractive index and absorption coefficient both are very low. Thus, the reflection from the air-nanowire interface is small and also the absorption through the nanowires is small. Most of the reflection observed is from the backside silicon and hence, the values approach that of the silicon in the experiment. For 190 nm, there is coherent coupling at $\sim$ 920 nm which makes the reflections from the air-interface stronger due to increase in the refractive index. Thus, a stronger Fabry-Perot cavity is achieved which is again observed in the reflection spectrum. For wavelengths shorter than 400 nm, because of the increase in the absorption of the constituent silicon in the nanowires, the reflections observed are reduced. The good correlation with the experimental data and calculated values strongly suggests the validity of our model. Strong absorption values seen in [43] could also result from the roughness at the nanowire-silicon wafer. The silicon wafer below will act as a slab waveguide for scattered light from the rough surface which could be coupled laterally into the slab modes. Thus, the light measured at the bot-

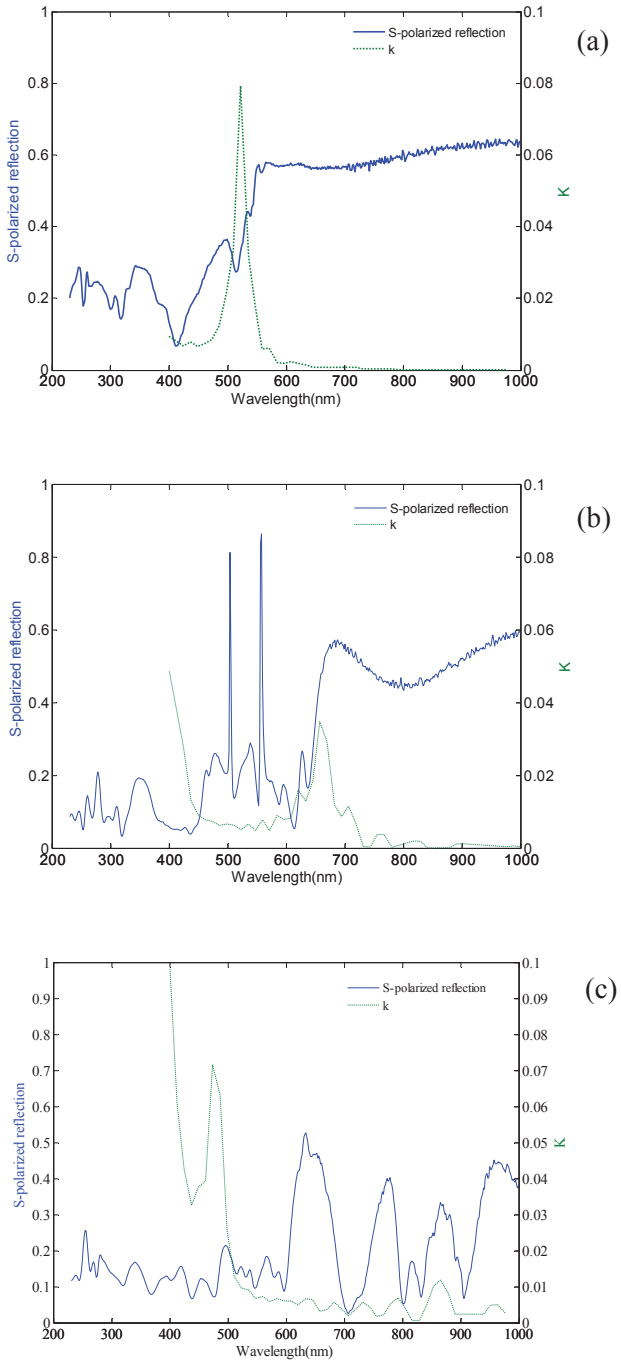

Figure 3.11: S-polarized reflections and calculated k values plotted for diameters of (a) 90 nm (b) 130 nm and (c) 190 nm.

tom could be reduced. The low values of quantum efficiency achieved in [43] may not only be due to surface recombination but due to the fact that silicon nanowires have not trapped light as much as predicted by just transmission measurements. Hence, it is our belief that to fully understand these complex structures, both reflections and transmissions should be measured. Back-side etching of the silicon substrate in order to measure transmissions is currently under progress.

3.3 Polarization Resolved Reflection from Bunched and Ordered Silicon Nanowire Arrays

In previous chapter, we studied mechanical properties of SiNWs. It was observed that for a given length, the nanowires start bunching up below a certain critical diameter due to van der Waal forces between neighboring nanowires and reduced stiffness. Thus by changing the diameter by only a few nanometers around the critical diameter, one could achieve highly vertical or bunched nanowires. This enables us to understand the differences between reflections from bunched versus vertical SiNW arrays as the diameters are very close to each other.

In this section, polarization resolved reflections from ordered and bunched SiNW arrays are measured and compared. It is shown that the reflections reduce considerably for bunched nanowires for the p-polarized input while not changing considerably for the s-polarized input between the ordered and bunched nanowires. The reflection is less than 9% for the whole 200 $nm - 1000$ nm wavelength excitation range for the bunched nanowires in the p-polarized beam. Frequency selective reflection features are observed in the ordered nanowires.

3.3.1 Sample preparation

For this study, SOI wafer was used as a starting substrate. The SOI wafer has a top silicon layer with a 1.5 μm thickness and a buried oxide layer with a 3 μm thickness. The array size for each diameter was 100 $\mu m \times 100$ μm The nanowires were arranged in a cubic lattice with a pitch of 400 nm between them. They were etched to a length of 1 μm. At this length the critical diameter for bunching and vertical phase was 85 nm. Four arrays of different diameters, two below the critical diameter and two above the critical diameter were fabricated. Figure 3.12 shows the SEM images of the nanowires in the arrays. Top view and side view images, in the inset, are shown. While the top view demonstrates the uniformity and the morphology of the

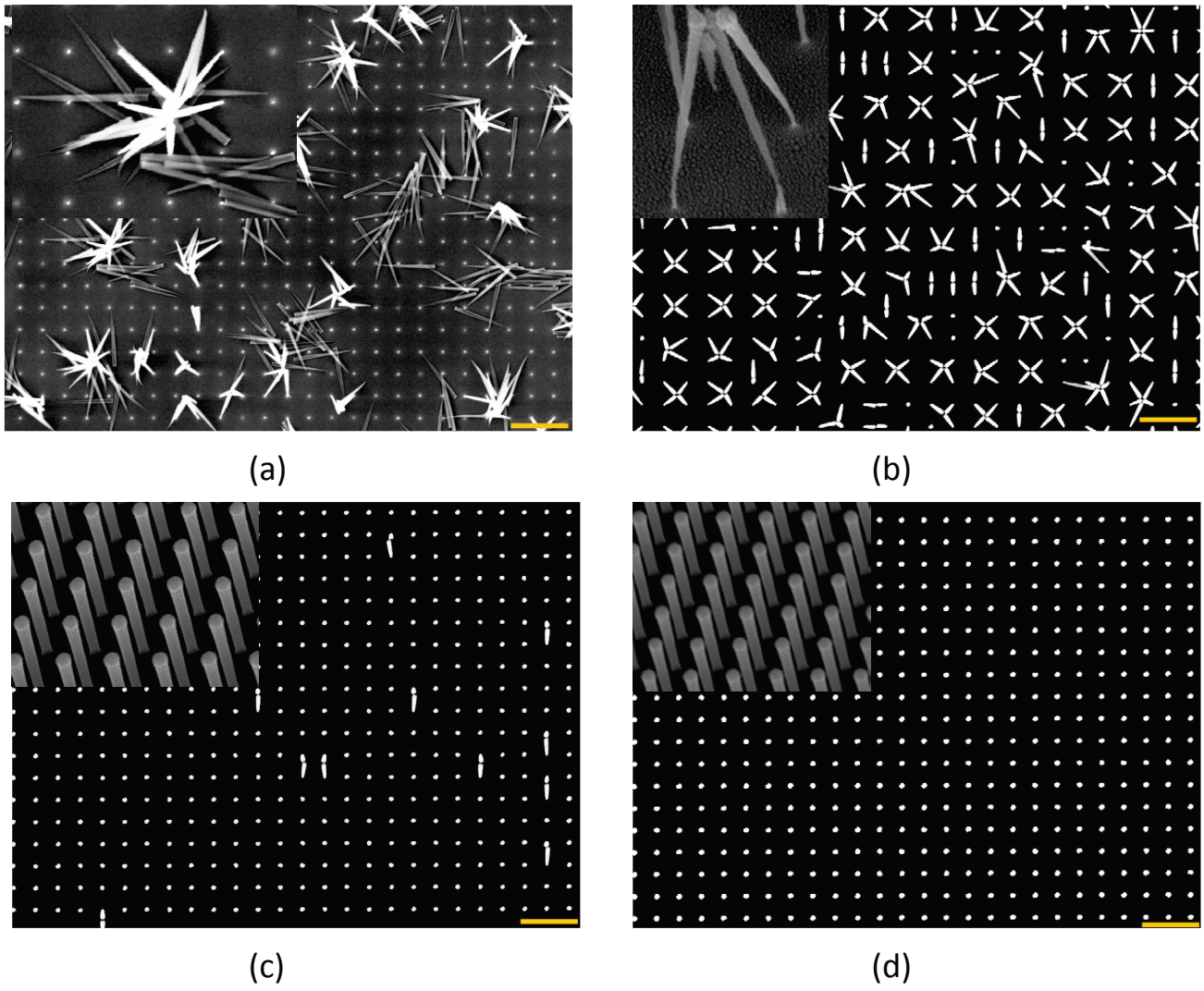

Figure 3.12: SEM images for SiNWs with diameter of (a) 65 nm (b) 80 nm (c) 90 nm and (d) 105 nm. All scale bars are 1μm.

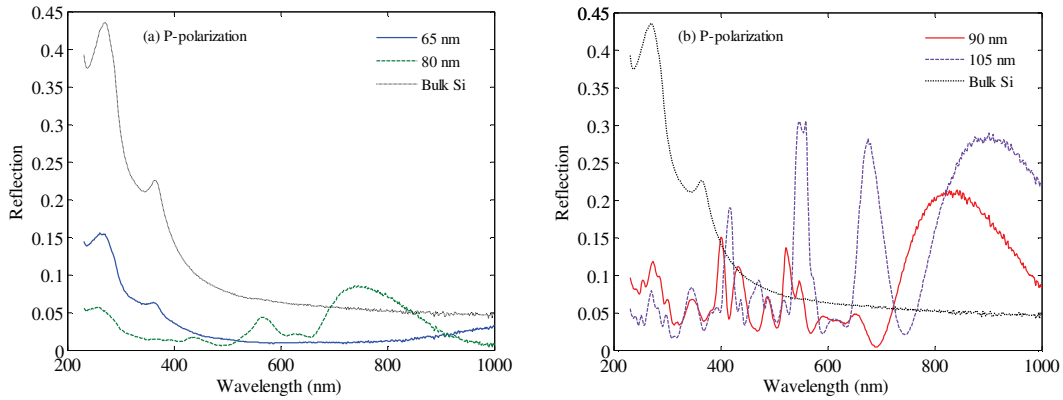

Figure 3.13: Reflections for p-polarized input for (a) bunched nanowires (b) vertical nanowires.

structures, the angled view shows the profile of the nanowires. For the diameter of 90 nm and 105 nm, the nanowires are perfectly vertical over the array. A few of the nanowires for the 90 nm diameters do bunch in pairs which could be due to diameter being locally reduced because of fabrication tolerances. For the nanowires of 80 nm, the nanowires bunch in groups of four creating highly ordered pyramid structures over the array. As the diameter is decreased further to 65 nm, the nanowires bunch together in larger structures and a disordered morphology is observed.

Figure 3.13 shows the reflection spectrums for the p-polarized beams for the four samples. Reflection measurements from the silicon surface on the side of the arrays are also shown. The different reflection spectrum for the p-polarized beams for the four different samples becomes quite apparent. For the smallest diameter nanowires which are highly bunched, the reflection is less than the bulk silicon for the complete wavelength range. However, the features in the spectrum are identical to that of bulk silicon. At longer wavelengths, the reflections from the array start to approach that of the silicon again. This suggests that the observed reflections may be coming from back silicon interface. As the wavelength increases, the feature size of the nanowires start to decrease compared to the wavelength and the scattering decreases. For the bunched nanowires of diameter 80 nm, the total reflection is less than 9 % over the complete spectral range. However, for wavelength range of 690 nm to 830 nm, the reflections are higher than those of the bulk silicon in the back. Also reflection decreases at higher wavelengths instead of increasing, as in the previous diameter. Similar frequency selective features are seen at wavelength of 552 nm and 429 nm. These peaks are absent in bulk silicon as well as the 65 nm diameter nanowire array. While these nanowires are bunched, the pyramids in this sample show some order and

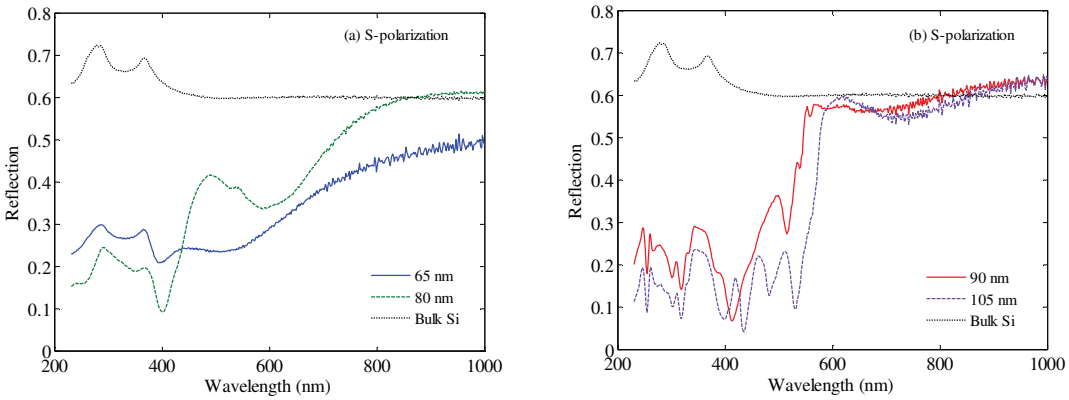

Figure 3.14: Reflections for s-polarized input for (a) bunched nanowires (b) vertical nanowires.

we believe this frequency selective behavior is a result of this order. On the other hand, when the nanowires are vertical at slightly larger diameters, the reflection behavior is quite different. Below 400 nm, the reflection is smaller than bulk silicon. The spectral features also do not fully correspond to those of bulk silicon. Between $400 - 1000$ nm spectral region, frequency selective reflection features start to be observed. As the diameter is increased further to 105 nm, these frequency dependent structures are even stronger. Further, as diameter increases, the reflection peaks start to move towards longer wavelengths.

Figure 3.14 shows the reflections over the band for the s-polarized input beam for the four samples. In all the four samples, the reflections are quite different compared to the p-polarized beam. The reflections reduce significantly below 500 nm as compared to above 600 nm. For wavelengths above 600 nm, the reflection is nearly the same at 60 % for the two ordered nanowire samples where it is approaching these values in the bunched samples. As the diameter of nanowire is changed, there is an abrupt shift with wavelength. For the ordered nanowires, the wavelength at which the shift occurs increases with diameter. Again as the diameter is increased in the vertical nanowires, frequency specific features start to become visible in the shorter wavelengths. The reflections are consistently higher for the s-polarized input compared to the p-polarized light. While there are wavelengths where the s and p-polarized reflections are low and nearly similar in either bunched or vertical nanowires, over the whole band the values could be quite different.

In order to understand these results, SiNWs can be considered to be cylindrical waveguides. In perfectly ordered arrays, coupling between neighboring SiNWs

can occur, like previous section. Depending on wavelength, this coupling becomes destructive or constructive resulting in frequency dependent features in the reflection spectrum. When the diameter is decreased and higher bunching is observed, the reflection is slightly higher in the shorter wavelength region and lower in the longer wavelength region compared to the pyramidal structures. The reflection from bunched nanowires can be explained by considering the nanowires as a tapered effective refractive index structure. In the bunched case, the nanowires provide a large open area on the front surface and the area slowly increases towards the silicon surface at the bottom creating pseudo-adiabatic transitions. At longer wavelengths for the larger bunches, this transition works well, creating a reduction in the reflection. On the other hand, for shorter wavelengths, additional scattering due to the bunching structure itself creates a larger reflection.

In summary, in last three section, we fabricated bunched and vertical SiNWs arrays and measured the polarization resolved reflection spectrum. To our knowledge this is the first time such studies have been conducted which allows us to understand how light behaves in the nanowire arrays. The reflection spectrum is remarkably different for s- and p-polarized beams. The reflection spectrum also suggests that very low absorption happens for these nanowires above 600 nm in the s-polarization. In the p-polarization case, low reflections are seen from disordered bunched nanowires while frequency dependent structures are seen from ordered vertical nanowires. These polarized reflection results provide useful information for various application using SiNWs such as solar cell, photodetector, and antireflection coating. In the next sections we will focuss on enhanced material properties of SiNWs.

3.4 Polarization-resolved photoluminescence from silicon nanowire arrays

3.4.1 Brief Introduction

For this study, two different nanowires were considered, ordered and bunched ones, and their photoluminescence were compared. For the ordered nanowire arrays, SiNWs with average diameters of 42 nm were created. The diameter was chosen such that the mechanical strength of the nanowires allowed them to stand vertical in an array with a slight bunching. In addition, at this diameter there are no quantum confinement effects resulting in no changes in the dipole matrix elements. Therefore, the Photoluminescence (PL) emission effects are mainly due to the role of image forces.

The disordered nanowire array was created by randomly changing the diameter of the nanowires between 30 nm to 80 nm. Due to van der Waal's interactions, some of these nanowires bunched randomly creating a disordered array. For both of the samples, a (100) Si wafer was used as the substrate. Fig. 3.15 shows the SEM image of the etched nanowires. The pitch between the nanowires was 100 nm and the length of the nanowires was 650 nm. The ordered nanowire arrays were arranged in a square lattice and were standing nearly vertical over the array. The disordering was created by the bunching of some of the nanowires with smaller diameter.

3.4.2 Measurement results

PL was measured using a PerkinElmer setup with an excitation wavelength of 325 nm. A schematic of the measurement is shown in Fig. 3.16. Two polarizers were employed at the input and the output enabling us to measure the PL for different excitation and emission polarizations. The incident angle of the beam on the sample was 30 degrees to the normal from the sample and the emission was measured also at 30 degrees angle to the normal. For the s-polarized input beam, the electric field cut across the nanowires and hence, the polarization was perpendicular to the nanowires. For the p-polarized beam, there is an electric field component along the length of the nanowires and another component perpendicular to the nanowires. For an external non-polarized light inside a nanowire with high refractive index contrast, the field inside the nanowire gets highly polarized. Due to the sub-wavelength nature of the nanowires, the field can be assumed to be constant within a nanowire. For an external field of E_0, the parallel component $E_{\parallel}$ is equal to the parallel component of the input field whereas the perpendicular component $E_{\perp}$ is suppressed in the nanowires and can be approximated as [66]:

$$E_{\perp} = \frac{2\varepsilon_0}{\varepsilon_0 + \varepsilon} E_{0\perp} \tag{3.4}$$

where ε_0 and ε are the dielectric permittivity's of air and silicon, respectively. While the equation was initially derived for static electric fields, it remains valid for high frequency fields as well. This increases probability of transition when the light is polarized along the length of the nanowires under an un-polarized light excitation. Consequently, this results in the PL emission with polarization predominantly along the axis of the nanowires.

Fig. 3.17 shows the PL emission for the s and p-polarized output when the input beam was unpolarized for the two samples. For the ordered nanowires, the PL

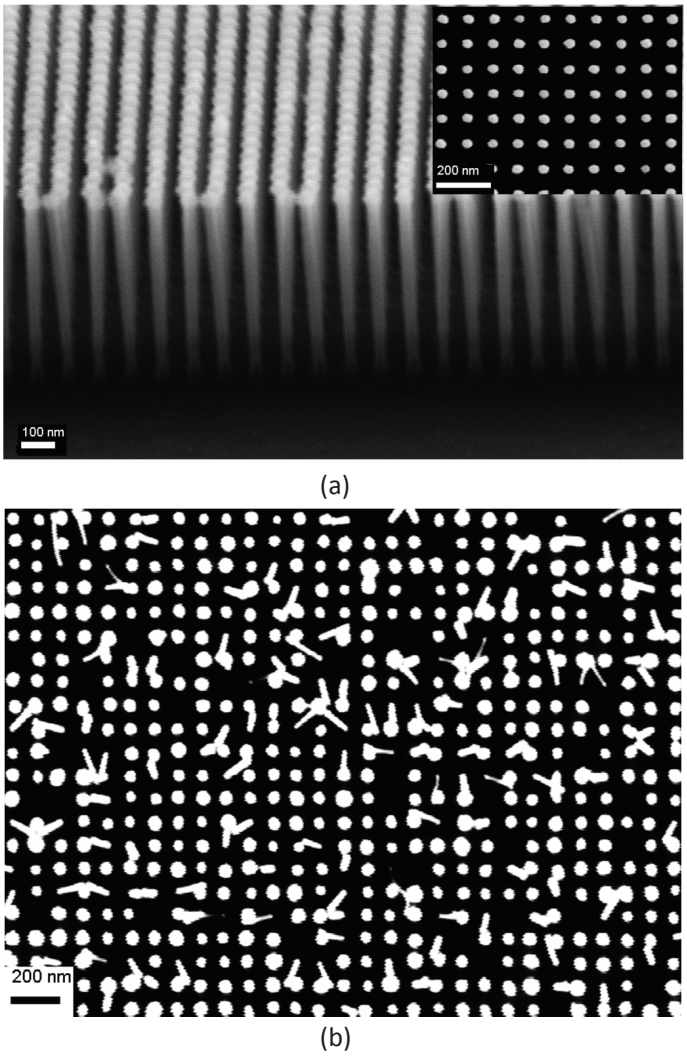

Figure 3.15: (a) SEM image of the etched nanowires for the ordered array of nanowires. The diameter is 42 nm, pitch is 100 nm and the length is 650 nm. The nanowires are arranged in a square lattice. Inset shows the top-view of nanowires after removing that aluminum mask. (b) Top-view SEM image of the etched nanowires for the disordered array of nanowires.

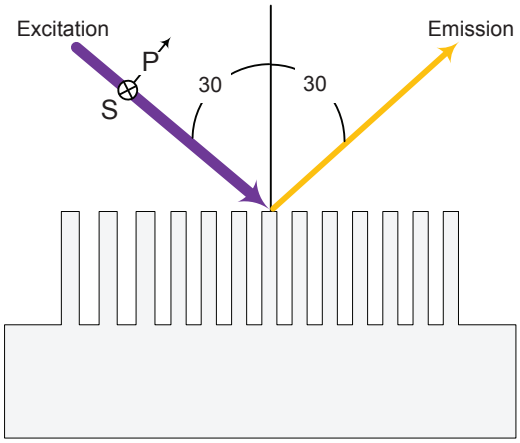

Figure 3.16: Schematic of the PL measurement.

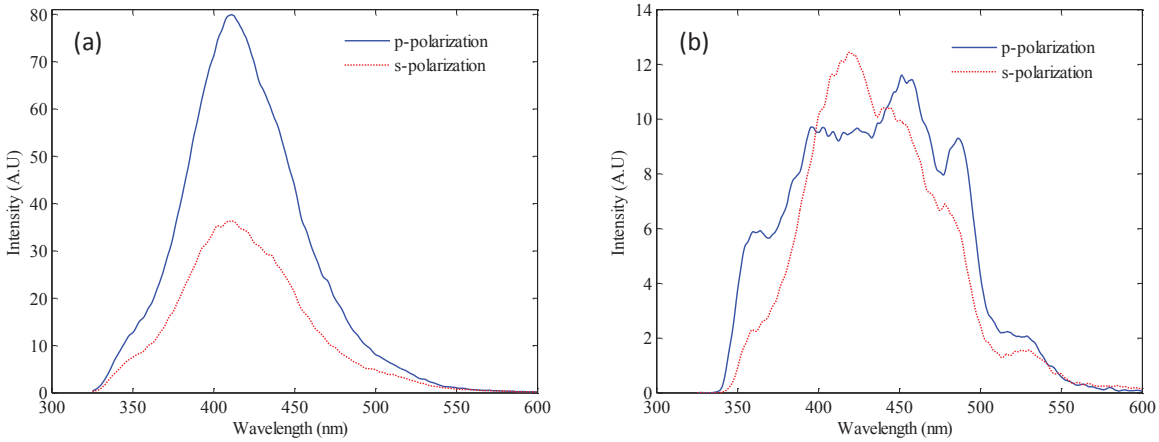

Figure 3.17: (a) Polarization resolved PL emission from ordered SiNW array. (b) Polarization resolved PL emission from disordered SiNW array.

intensity for the SiNWs is higher compared to the silicon by a factor of 50. The spot size of the exciting beam was larger than the array size and the actual enhancement should be larger. If the total PL output is considered, the p-polarized output (which contains the polarization parallel to the nanowires) is larger than the s-polarized output by a factor of 1.8. There is a peak in the near-UV peak which is due to exciton absorptions in the bulk of the nanowires [19]. As shown in Fig. 3.17, the PL emission is stronger in the p-polarization. The ratio of the total PL power within the $325\ nm - 550\ nm$ between the p and s-polarized output is 2.05. By considering the peak values, the ratios become 2.2. We can write the Poynting vectors, S, for the s and p-polarized beams as [66]:

$$S_p = \frac{\nu\omega^4}{\pi\varepsilon_0^2 c^3 x_0}[(\frac{d_\perp^2 + 2d_\parallel^2}{6})sin^2(\theta) + \frac{d_\perp^2}{2}cos^2(\theta)] \tag{3.5}$$

$$S_s = \frac{\nu\omega^4}{\pi\varepsilon_0^2 c^3 x_0}\frac{d_\perp^2}{2}$$

where ν is the density of dipoles per unit length, $d_\perp$ and $d_\parallel$ are the dipole moments in the perpendicular and parallel direction, respectively and are given by:

$$d_\perp = \frac{2\varepsilon_0}{\varepsilon_0 + \varepsilon}d_0 \tag{3.6}$$

$$d_\parallel = d_0$$

where d_0 is the dipole moment of silicon. No quantization was assumed and as such the dipole moments were considered to be the same in all directions. Assuming the relative permittivity of silicon to be 11.68, the ratio between the s-polarized and p-polarized output is 1.88, very close to the ratio of 2.05 achieved for the two polarizations. The small variation could be due to the fact that there is guidance of light within the nanowires at the diameter of 42 nm and the confinement of the structure is higher than the one given by Eq. 3.4. Thus, it is apparent that the near-UV peaks of the PL are excited from the bulk of the material. Further, the peaks for the two polarizations are at the same energy, suggesting that there is no quantization of the dipole matrices. For the disordered nanowires, no preferred polarization of PL is observed and similar intensities are observed in either polarizations. This is because the nanowires are randomly arranged to the polarization axis while an individual nanowire will emit PL preferably with polarization along its length, over the ensemble.

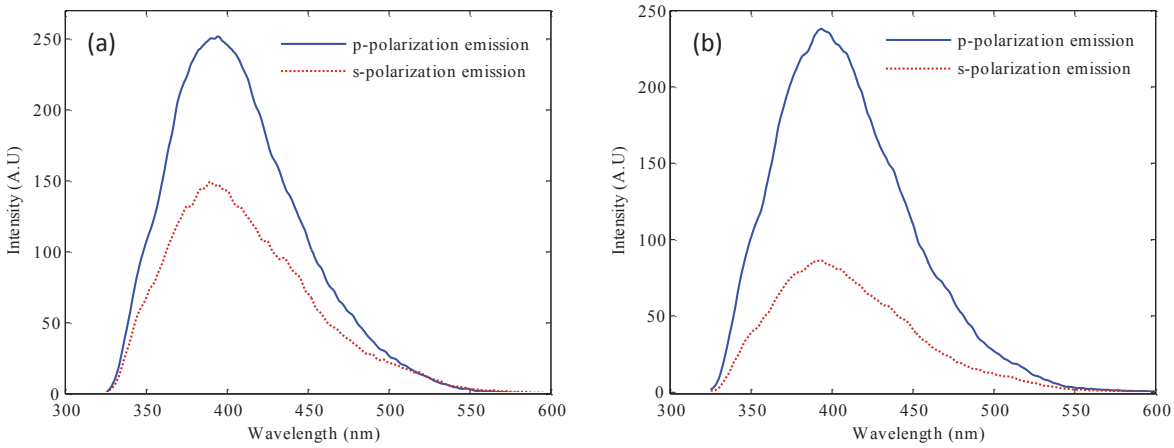

Figure 3.18: (a) Polarization resolved PL output when the ordered nanowires are excited by s-polarized input. (b) Polarization resolved PL output when the ordered nanowires are excited by p-polarized input.

Further the total PL intensity is lower compared to the ordered nanowires by a factor of 6.

Fig. 3.18 shows the PL emission when the ordered nanowires were excited by either p- or s-polarized beams and the emission observed in the s- and p-polarization. As shown, emission is maximum for the p-polarization output for both of input polarizations. Further, the intensity of the peaks is nearly the same for either input polarizations. This is in contrast to disordered nanowires such as black silicon or porous silicon, where the emission is seen along the direction of the input polarizations [67]. However, the contrast between the p- and s-polarized light increased from 1.43 for s-polarized input to 2.76 for the p-polarized input. So while the excitation of the p-polarized output is the same for both the input polarizations, the s-polarized output is preferentially excited by the s-polarized input. The ratio between the peaks is 1.75. Therefore there is a PL memory for s-polarized output. This memory effect could be due to small bending in the nanowires which varies over the array. Figure 3.19 shows the PL when the disordered nanowire arrays were excited by either p- or s-polarized beams and the emission observed in the s and p-polarization. As opposed to the ordered nanowires, strong PL memory is observed with emission higher in the same polarization as with the excitation. This is similar to black silicon or porous silicon studies. The ratio between the peaks is 5.3 and 8.9 for input polarizations of s and p, respectively.

These results can give insightful information for designing active devices based

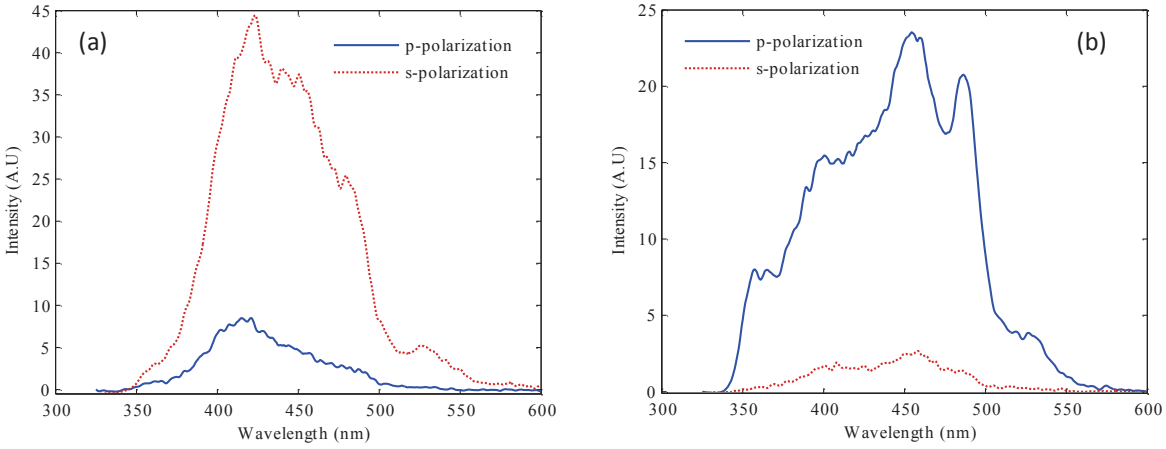

Figure 3.19: (a) Polarization resolved PL output when the disordered nanowires are excited by s-polarized input. (b) Polarization resolved PL output when the disordered nanowires are excited by p-polarized input.

on enhanced PL in array of nanowires. In the next section, we we focus on another weak phenomenon in silicon.

3.5 Second Harmonic Generation

Second-harmonic generation (SHG) is also very weak in bulk silicon due to the inversion symmetry [23] and only an electric dipole response from the surface or an electric quadruple response from the bulk is observed [24]. While progress has been made for non-linear mixing in SOI waveguides, it is based on the third-order nonlinear response [15] and as such requires a large pumping power making their practical use suspect. Consequently, there has been increased interest in achieving second-order nonlinearities in silicon based materials. In this section, the second order non-linearity is demonstrated in second-harmonic generation and rotational anisotropic measurements. Enhancement by at least a factor of 80 was achieved as compared to bulk silicon for the p-polarized input and s-polarized output.

3.5.1 Results and discussion

SHG was studied by exciting the nanowires with a fundamental beam derived from a 1 kHz Ti:sapphire oscillator emitting an average power of approximately 800 mW

(800 J per pulse). These pulses are attenuated to an average power of 0.6 mW (0.6 J per pulse) to avoid damaging the samples. The beam was focused onto the samples using a 0.12 numerical aperture microscope objective with a focal length of 20 cm, at an angle of incidence of $\theta = 60°$. Because of the large incidence angle, the spot size on the sample was approximately 30 $\mu m \times 100$ μm. Reflected and the 390 nm SHG output from the sample was collected using another microscope objective; then the two beams were separated by a dichroic mirror and several filters. SHG signal was measured with a cooled photomultiplier tube and photon-counting electronics. The sample under test was kept at room temperature and atmospheric pressure. It was positioned on a set of translation and rotation stages such that they can be rotated about the surface normal to measure the rotational anisotropic SHG while keeping a particular point in the beam focus. A halfwave plate and polarizer were used to control the polarization state of the fundamental light, and an additional polarizer was used to select which SHG polarization to be measured. The second-order optical nonlinearity was measured through the rotational anisotropic SHG on the nanowire array [24]. For a p-polarized pump, the SHG intensity I_{SHG} for a (100) silicon surface with the fundamental beam intensity of I_{in} can be described as function of the azimuthal angle with respect to crystal orientation as [28]:

$$I_{SHG} = (a + b.cos(4\phi))^2.I_{in}^2 \tag{3.7}$$

where a and b are the isotropic and anisotropic coefficients, respectively resulting from Fresnel coefficients and the contributions due to non-linear optic tensor components. Figure 3.20(a) shows the schematic setup for the measurement. The average power of the fundamental beam was 0.6 mW in these measurements. The SHG signal from bulk silicon is shown in Fig. 3.20(b) for p-polarized input. Figure 3.20(c) shows the azimuthal dependence of the SHG signal for p-polarized input for the nanowire arrays. A theoretical fit to the data is also plotted with good correspondence. While the experimental data conforms the theory, there is an asymmetry in the data which could be resulted from the fact that the bunched nanowires are not symmetrical in geometry. The maximum photon count was 320 per second. The bulk silicon shows a maximum value of few photons (~ 4) per second which suggests an improvement by a factor of at least 80 from the maximum SHG coming from bulk silicon. The comparison was done at the maximum value of SHG signal from bulk silicon and not at a corresponding angle for the two measurements as the signal from silicon is noise limited. These measurements were also done for s-polarized fundamental beam and are shown in Fig. 3.20(d). For this input polarization, the SHG signal is only large at $\phi = 270°$. Similar behavior was observed in platinum nanowires on MgO faceted templates [68] and could arise from the broken symmetry in the

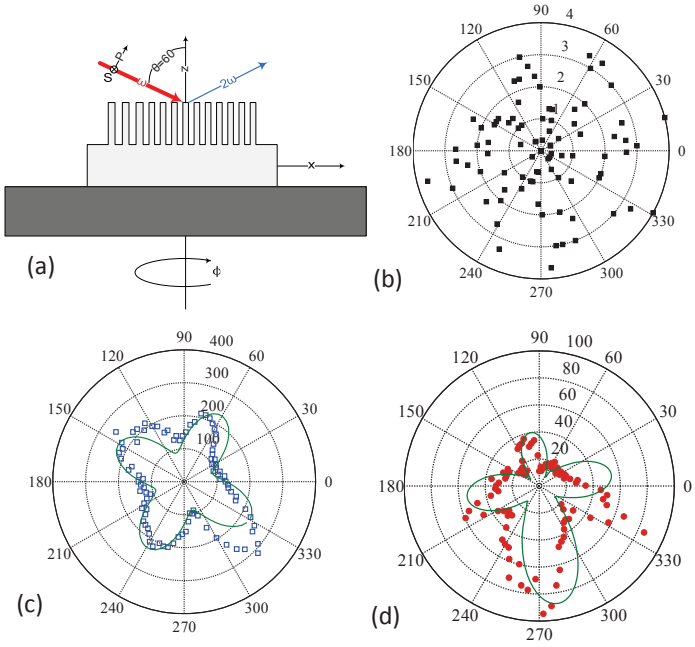

Figure 3.20: (a) Schematic diagram of rotational anisotropic SHG measurement. (b) S-polarized SHG signal from the bulk silicon as a function of azimuthal rotation angle for p-polarized fundamental beam (c) S-polarized SHG signal for p-polarized fundamental beam. (d) S-polarized SHG signal for the s-polarized fundamental beam.

nanowire arrangement in the array. Fitted curve is achieved using equation 3.7 by considering different values of the parameters a and b in the equation for each 90 degree region around peak values. The huge enhancement of the SHG is mainly due to the broken symmetry and electric enhancement within the nanowires and it can exploited to build silicon based nonlinear optic devices and also open the door in studying the other nonlinear characteristics such as third harmonic generation and four wave mixing.

In conclusion, we have demonstrated enhanced SHG in SiNWs. The SHG signal increased by at least a factor of 80 for nanowire arrays with 37 nm diameter as compared to bulk silicon.These results show the promise of using SiNWs as a platform for non-linear silicon optical devices and introduces potential applications in silicon that were not possible before.

3.6 Raman Spectral Measurements and Discussion

In this section, we study Raman spectrum of SiNWs prepared with two different methods. In first case, SiNWs were grown using Vapor Liquid Solid method in a Plasma-Enhanced Chemical Vapor Deposition (PECVD) by our collaborator, Prof. Karim's group. In this method, SiNWs were grown separately on glass and steel substrates and investigated with Raman spectroscopy. In the next method, SiNWs were fabricated by top-down approach as discussed in previous Chapter.

Raman studies of SiNW, grown using VLS, have reported Raman shifts in the single phonon energy to $\sim 505 - 515\ cm^{-1}$ for wires ranging from 10 nm to 30 nm in diameter, as well as an asymmetric line shape [69–72]. It was determined that heating by the laser [69] or lattice stress [72] plays a major role for the observed downshift, and is also responsible for the asymmetric broadening. It is also believed that phonon confinement effects are an additional source of broadening. We study the local intense heating caused by laser power and the role of thermal conductivity of substrate.

We also investigated effects of laser power on Raman spectra of SiNWs prepared by dry-etching. We report for the first time that no shift, or broadening, of the first-order phonon peak in SiNW are observed for the etched nanowires. This suggests that highly ordered SiNW fabricated by dry-etching possess much better thermal conductivity properties than their VLS grown counterparts.

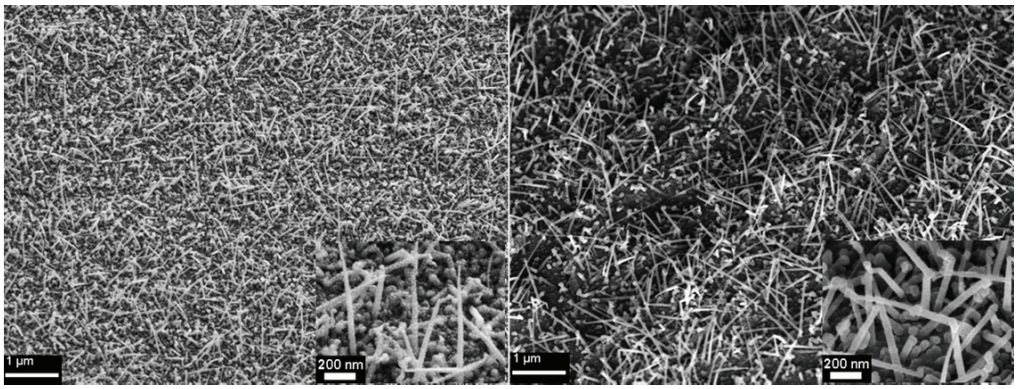

Figure 3.21: SEM images of the silicon nanowires grown on glass (left) and steel (right) substrates. Inset shows a magnified image.

3.6.1 Sample Preparation and Experimental Setup

Sample Preparation

The SiNWs samples were grown by VLS method in a PECVD system either on a Corning 1737 glass substrate or a steel substrate. The growth conditions were kept similar for both the substrates. In the first step, a 2 nm thick layer of tin (Sn) was deposited by e-beam evaporation. Sn nano-droplets were formed by annealing the sample at $400°C$ for 1 hour in the PECVD chamber, and were used as a catalyst for nanowire growth. Silane was used as the gas source for the growth. Further details of the growth process are described in [73]. Figure 3.21 shows the SEM images of the grown nanowires on the two substrates. For the nanowires grown on the glass substrate, the nanowires were coated with 10 nm layer of gold to reduce the charging by an SEM beam while imaging. The average length of the nanowires was 1 μm. Further, the density of the nanowires was larger on the steel substrate as compared to the glass substrate which is thought to arise from the different density of Sn droplet formation during the annealing process.

Raman spectroscopy was measured using a Horiba Raman spectrometer at room temperature in ambient atmosphere equipped with a confocal microscope in the backscattering configuration, with a spectral resolution of 0.3 cm^{-1}. The wavelength of excitation was 632.8 nm using a He-Ne with the electric field polarized perpendicular to the nanowires at normal incidence. The beam was focussed on the samples with a 20× microscope objective with a numerical aperture of 0.4. The incident optical power was changed by using neutral density filters in the beam path to a

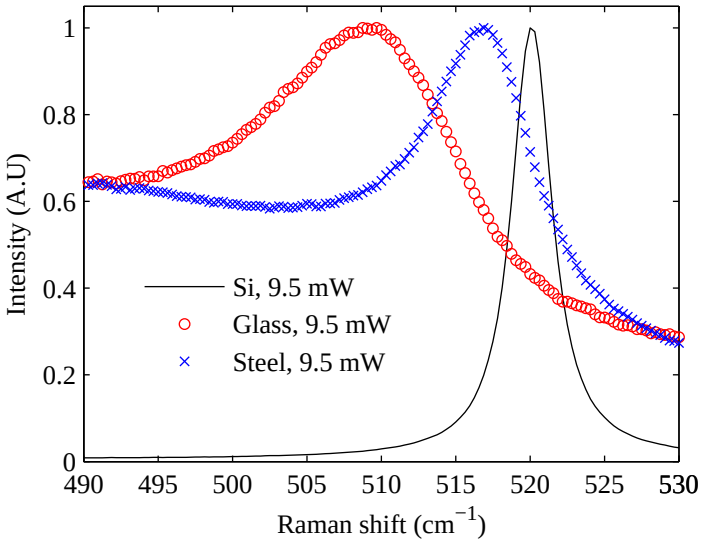

Figure 3.22: Raman spectra for nanowires on the steel and glass substrates. Raman spectrum form bulk silicon is also shown as a reference.

minimum of 0.8 mW. The minimum power for which a signal could be measured was limited by the signal to noise resolution of the detector in the spectrometer.

Results and Discussion

Figure 3.22 shows the measured Raman spectra from the two nanowire samples, and a bulk silicon wafer as a reference, for an incident laser power of 9.5 mW. The intensity at this power is approximately 0.1 mW/cm^2. The spectra have been normalized locally for ease of comparison. The Raman spectra for both of the nanowire samples consist of a crystalline silicon peak and a broadband spectrum attributed to the amorphous silicon [74]. For the crystalline peaks, both the nanowire samples show a red shift in the peak. Each Raman spectrum was fitted by using a Lorentzian line shape with an asymmetry to represent the crystalline peak, a Gaussian function for the amorphous shell and another Gaussian function for the broad background. Asymmetry was introduced in the Lorentzian by using different width on the left and right sides of the peaks. A representative fit is shown in Fig. 3.23 for the nanowires grown on the glass substrate. Using the fit, the peak of the Lorentzian in the crystalline peak and the full width half maximum (FWHM) of the crystalline spectrum can be determined. For the nanowires grown the glass substrate, which has

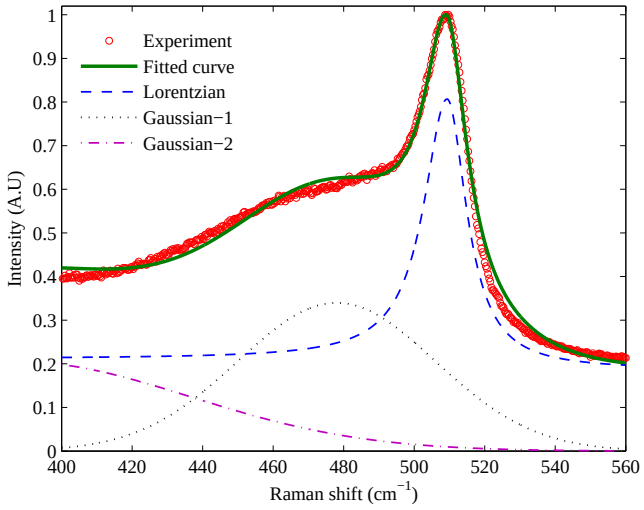

Figure 3.23: Fits to the measured Raman spectrum. A Lorentzian line shape was used to fit the crystalline peak. Two Gaussian functions were used for the amorphous silicon and background. Dotted lines show the individual fit and the green shows the resulting fit.

the lower thermal conductivity, the crystalline Raman peak is at 509.3 cm^{-1} with a FWHM of 14.75 cm^{-1}, and the values compare well with other observations [69, 70]. For the nanowires grown on the steel substrate, the Raman peak is at 517 cm^{-1}, and the FWHM has been reduced to 8.55 cm^{-1}. The spatial confinement effect of the optical phonon wave function has been previously suggested as the reason for red shift of the peaks and asymmetry [75, 76]. Using the spatial confinement effect, the expected red shift in the peaks as compared to the bulk silicon is $1 - 2$ cm^{-1}, not 10.7 cm^{-1} as observed here for the nanowires on the glass substrate. Stress has also been suggested as a contributing factor resulting in an additional expected frequency shift of 2.5 cm^{-1}. On the other hand in [72] local heating of the SiNWs due to laser pulses was suggested as the fundamental criteria for the red shift and asymmetry. Further, it was shown in [70] while thermal conductivity of crystalline nanowires can be as high as that of bulk Si, it can decrease by two order of magnitude in nanowires with amorphous shell. In our experiment, we compared nanowires with similar average core diameters but on two substrates with different thermal conductance (thermal conductivity of steel is $16 - 24$ $W.m^{-1}.K^{-1}$ and for Corning glass is $\sim 0.9 W.m^{-1}.K^{-1}$). Largely different Raman spectra crystalline peaks strongly point to the effect of local heating in the Raman spectra rather than

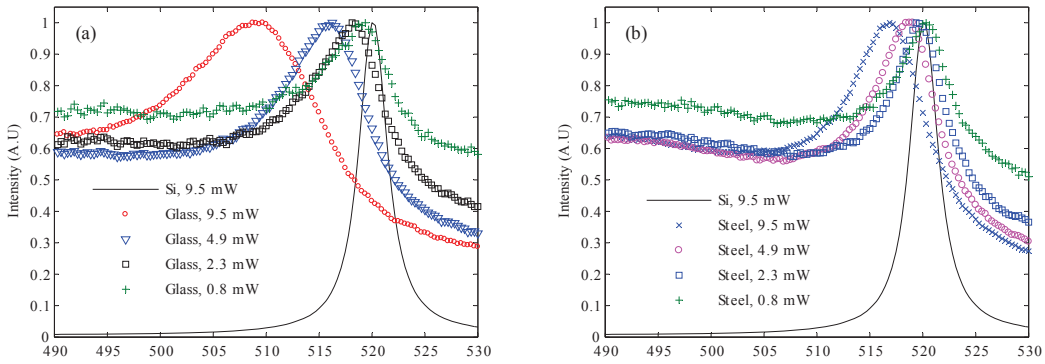

Figure 3.24: Raman spectrum for the SiNWs grown on (a) Corning glass, (b) Steel as the incident power was reduced. A blue shift in the peaks and a reduction in the FWHM was observed.

enhanced anharmonicity and strain.

In order to further confirm the effect of temperature, the input power was reduced using neutral density filters. This should result in decreased heating of the sample. Figure 3.24 shows the Raman spectra, using reduced laser power, for the nanowires grown on glass and steel substrates. From this data, the peak values and the FWHM are calculated and plotted in Fig. 3.25 and 3.26, respectively. As the power is decreased, the red shift decreases for both the samples and less spectral broadening is observed. At the lowest power of 0.8 mW, the peak shifts to 519 cm^{-1} for the glass substrate, which agrees well with the data in [77]. The confinement models predict < 1 cm^{-1} shifts for the nanowires with sub-10 nm diameters. However, in our experiment, at the same power, the first order Raman peak for the nanowires grown on the steel substrate is at 519.9 cm^{-1}. Hence, we conclude that the small shifts observed in the glass substrate at low powers are still coming from thermal effects and not from quantum confinement. For the lowest power of 0.8 mW, the FWHM is 8.5 cm^{-1} and 6.1 cm^{-1} for SiNWs on glass and the steel substrates, respectively, and 3.5 cm^{-1} for the bulk silicon. So while the peak does not show a shift for the steel substrate, there still is a broadening of the Raman spectrum. This broadening could be due to the confinement of the phonon and compares well with the results shown in [78], for similar diameters of purely crystalline SiNWs with no amorphous shell. This again strongly suggests that the shifts observed previously in core-shell nanowires were still due to thermal effects.

In this section, we have shown that the local intense laser heating combined with the poor thermal conductivity of glass substrates affects the Raman spectra of SiNWs.

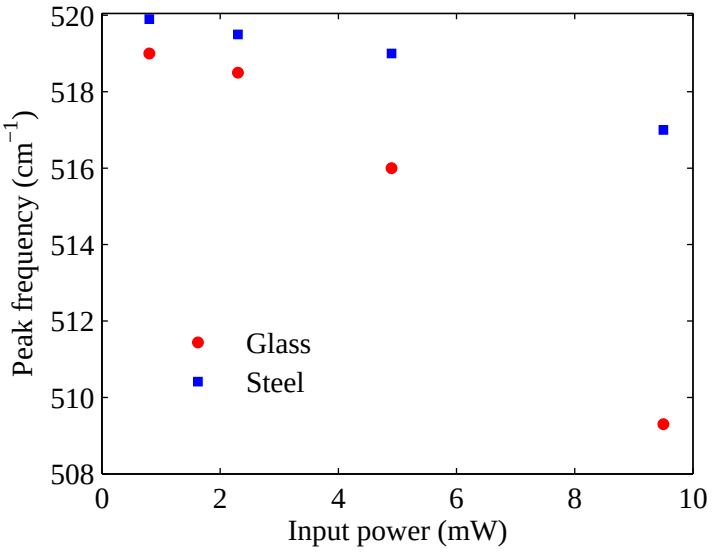

Figure 3.25: Peak of Raman spectrum of samples on glass and steel substrates for different input powers.

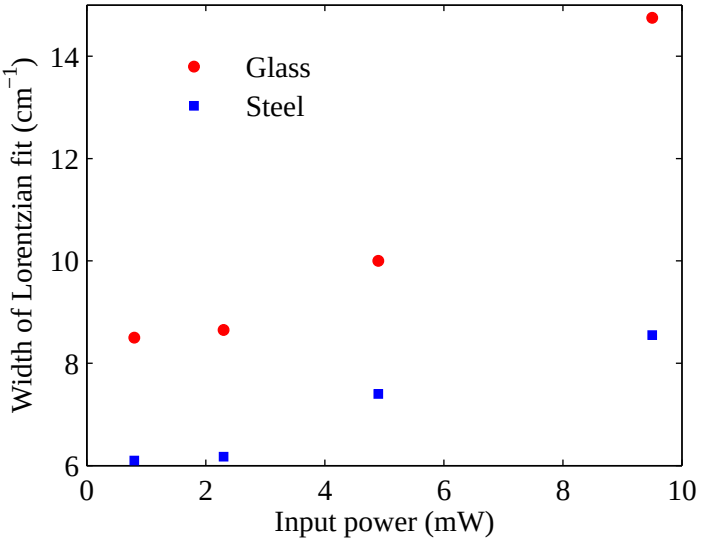

Figure 3.26: Width of Raman spectrum of sample on glass and steel substrates for different input powers.

When similar nanowires were grown on steel which is a better thermal conductor, the shifts in Raman peaks and the asymmetry in the crystalline silicon peak was much smaller, and it was in the order expected from phonon confinement. Peaks due to the amorphous silicon in the shell of the nanowires were also observed. This also suggests that fundamental studies on nanostructures can be carried out by using higher laser powers in the presence of substrates with higher thermal conductivities. The increased Raman signal and improved signal to noise ratios will allow for more accurate measurements of quantum effects in these low dimensional systems. In the next sub-sections, the same experiment has been carried out on SiNWs created by top-down approach.

3.6.2 Enhanced Raman Scattering in SiNWS Prepared by Top-Down Approach

Raman Measurement on SiNWS Prepared by Top-Down Approach

In this section, first Raman spectral of vertical ordered SiNW arrays with diameters ranging from 30 nm to 60 nm are measured. The first order 520 cm^{-1} phonon mode shows no significant shift or peak broadening with increasing laser power, suggesting the excellent defect-free diamond crystalline structure and thermal properties of bulk silicon are maintained. The Raman enhancement per unit volume of the first order phonon peak increases with increasing nanowire diameter, and has a maximum enhancement factor of 7.1 and 70 when compared to the original SOI and bulk silicon wafers, respectively.

A SOI wafer with 340 nm thick (100) top silicon layer was used as the substrate. The buried oxide layer was 1 μm thick. The nanowires were etched in an area of 100 $\mu m \times 100$ μm and were arranged in a square lattice. The pitch between the nanowires was 100 nm and the diameter was changed over 8 different values from 30 nm to 60 nm. In the previous chapter, we have shown that bunching due to van der Walls forces of nanowires fabricated in arrays depends on the diameter to length ratio. As we were interested in vertical nanowire arrays for the present study, the length of the nanowires was kept at 210 nm leaving a 130 nm Si layer at the bottom. This was done to ensure that even the 30 nm diameter nanowires remain vertical in the array. Figure 3.27(a)-(c) show top view SEM images for diameters of ~ 30 nm, ~ 40 nm and ~ 60 nm. A side view image showing the length profile of nanowires with diameter of ~ 40 nm is also shown in Fig. 3.27(d). Highly ordered and vertical nanowire arrays were achieved for all of the diameters. A cross-sectional schematic

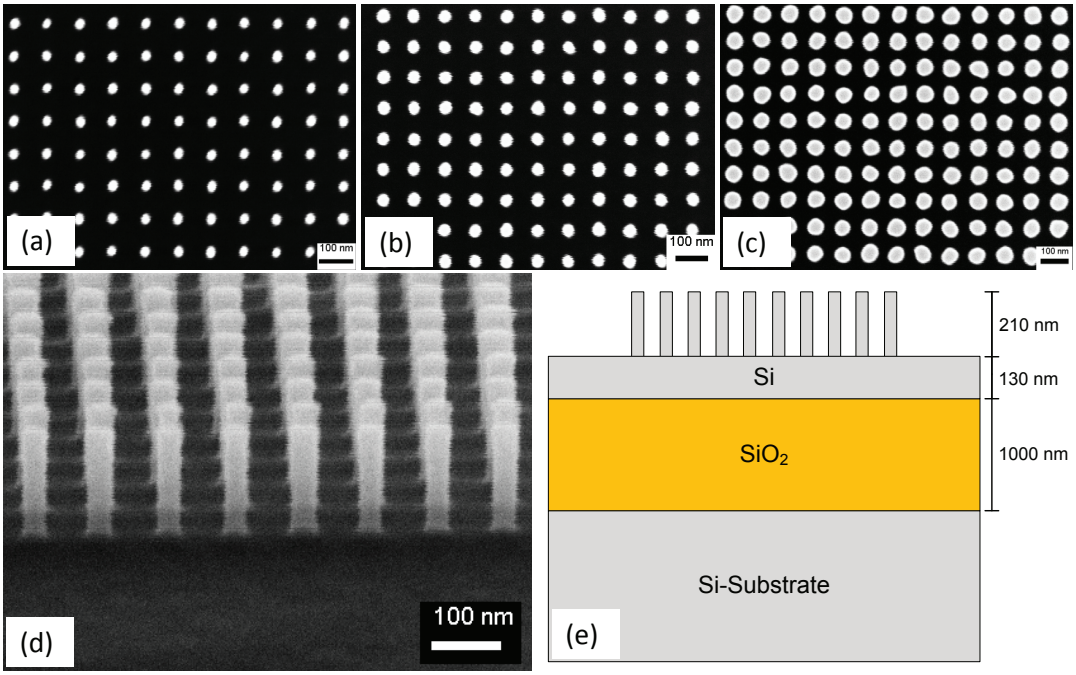

Figure 3.27: Top view SEM images of nanowires for (a) 30 *nm* diameter, (b) 40 *nm* diameter and (c) 60 *nm* diameter nanowires after the etching and cleaning processes. Side view of the 40 *nm* diameter nanowire array showing the length profile is shown in (d). Sample schematic with different layers is shown in (e) [3].

diagram of the whole structure is also shown in Fig. 3.27(e) depicting the nanowire array, residual unetched silicon, the buried oxide layer and the substrate.

In is notable that the same Raman set-up is used for this measurement. The effect of laser heating was investigated by varying the laser power level from 0.8 mW to 9.75 mW using neutral density filters. Besides measuring the nanowire samples of different diameters, Raman spectra were also measured for a bulk silicon sample, the original unetched SOI wafer, and on the SOI wafer next to the nanowire array, where 130 nm of residual unetched silicon was present (see Fig. 3.27 (e)).

Laser heating has been shown to cause a redshift of the 520 cm^{-1} phonon mode to values near 510 cm^{-1}-515 cm^{-1} [77]. Additionally, heating will generally cause symmetric or asymmetric broadening of this phonon peak as well. Measurements were performed on nanowires with diameters of 33, 47, and 60 nm for power levels of 0.8, 4.75, and 9.75 mW and are shown in Fig. 3.28. At 9.75 mW, the intensity of light is $\sim 0.1\ mW/\mu m^2$. At this intensity in VLS nanowires, inhomogeneous heating of the nanowires has been previously predicted [78]. In our experiments, the data were well fitted to Lorentzian line shapes as shown in Fig. 3.28(a) for different diameters at the highest laser power. Measurements over different laser powers for different diameters are shown in Fig. 3.28(b)-(d). Again all the data fit well with Lorentzian line shapes and for a given diameter, no significant shift or broadening of the spectra was observed. This is expected for crystalline SiNWs above diameters of 20 nm as shown in [78]. While the input power could not be increased, light was focussed with a 50× microscope objective on the 30 nm diameter nanowires and no additional shift was observed at the increased intensity. However, with respect to bulk silicon (the peak position is shown by the dashed vertical line in Fig. 3.28(b)-(d), there is a shift of 0.4 cm^{-1} for the nanowires with diameter of 33 nm, and the shift decreases with increasing diameter as expected from phonon confinement based on Richter *et al.* and Campbell and Fauchet (RCF) models [75]- [76]. While there seems to be a consistent reduction in the shift of the peak with increasing diameter, the values are still prone to error due to the 0.3 cm^{-1} resolution of the spectrometer. Nevertheless, these results are in contrast to what have been previously reported for VLS grown nanowires, where an appreciable shift (up to 10 cm^{-1}) is observed, and has been attributed to heating of the nanowires and lattice stress. The full-width half max (FWHM) varies between 3.4 and 3.5 cm^{-1} for the nanowire arrays while it was 3.5 cm^{-1} for the bulk silicon. All the measured values for the FWHM are within the resolution of the experimental setup and no spectral broadening is observed for different diameters or laser powers. Based on these findings, we conclude that the nanowires still possess defect-free diamond crystalline structure, and thus excellent resistance to local heating. This was also confirmed by comparing the Raman spec-

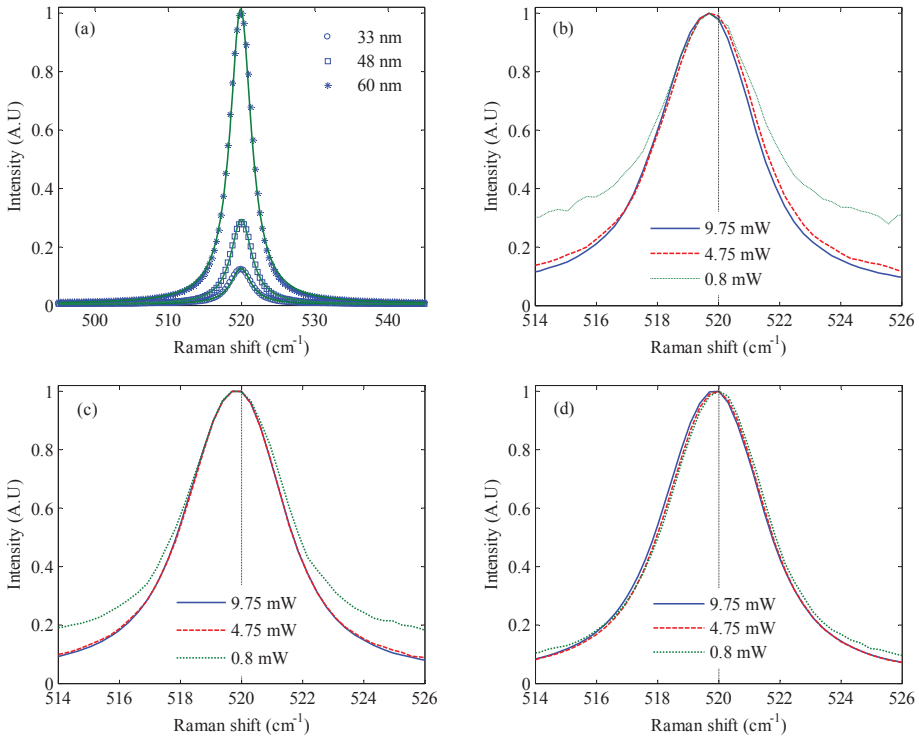

Figure 3.28: Raman spectra for three different laser powers and SiNW diameters. (a) Experimental data and Lorentzian fits for 33, 48, and 60 nm diameter wires at 9.75 mW. (b) SiNWs with a diameter of 33 nm (c) SiNWs with diameter of 48 nm (d) SiNWs with diameter of 60 nm [3].

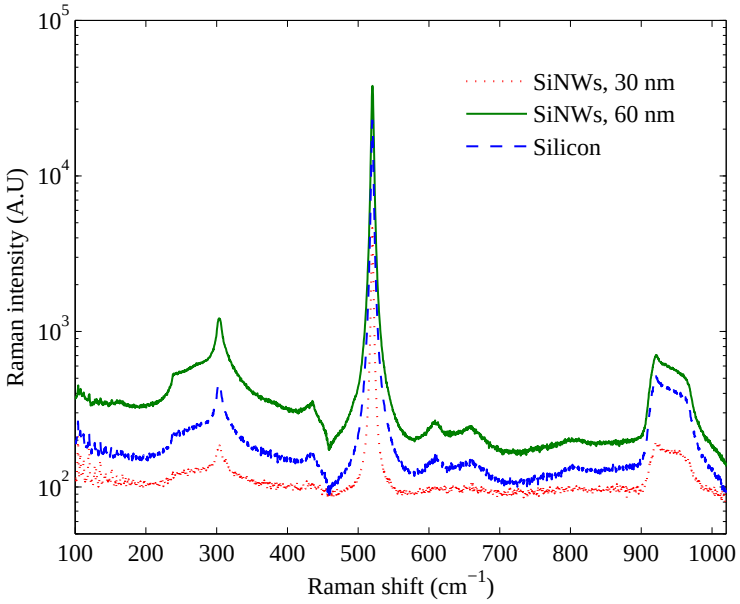

Figure 3.29: Raman spectrum form bulk silicon and nanowire samples of 30 nm and 60 nm diameter showing well defined and similar multiphonon peaks. These peaks were absent in VLS grown core-shell nanowires [3].

trum covering the range from 100 to 1000 $cm^{-1}$for SiNWs and the bulk silicon, and is shown in Fig. 3.29 . All the multi-phonon peaks present in the crystalline bulk silicon were present and well defined in the nanowire samples suggesting the nanowires are indeed crystalline. The same measurement on VLS grown core-shell nanowires did not show the multi-phonon peaks. Local heating due to the laser source has made it difficult to discern spectral details arising from phonon confinement. In this connection, highly ordered etched SiNW arrays could become model systems for studying quantum confinement effects. It is emphasized here that we have not measured the change of thermal conductivities with different diameters. The experiments strongly suggest the values of thermal conductivities are large enough not to cause significant local heating which was previously reported in VLS grown nanowires for similar diameters and input intensities.

The Raman spectrum of the first-order single phonon peak was measured for all nanowire diameters, using a laser power of 9.75 mW. The results are shown in Fig. 3.30. Raman spectra from the bulk silicon wafer, SOI wafer and the residual unetched silicon neighboring the nanowire arrays are also plotted. The 520 cm^{-1} signal arises

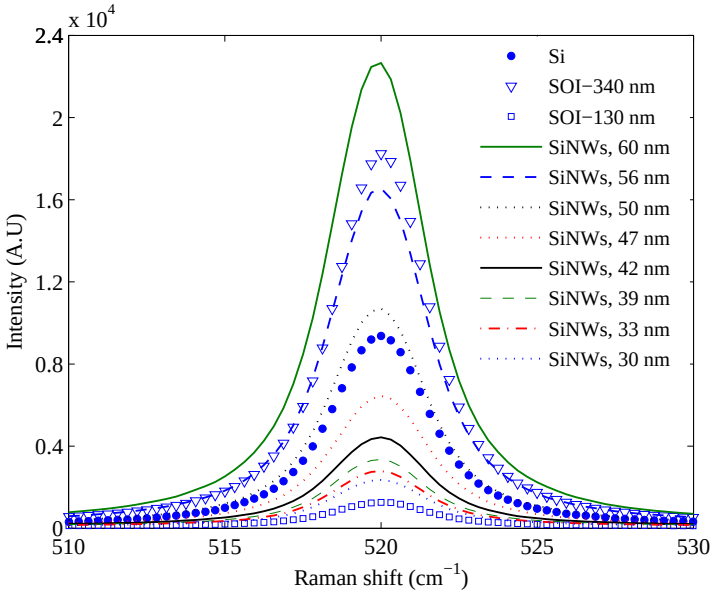

Figure 3.30: Raman spectra for SiNWs, Si and SOI wafer after and before etching [3].

from the scattering of incident light with the first-order optical phonon in the diamond structure of the nanowires. It is observed that as the nanowire diameter increases, the Raman intensity increases from the sample. For the residual unetched silicon neighboring SiNW arrays, the peak intensity is 1260 arbitrary units (A.U), whereas for the 30 nm nanowires (smallest) it increases to 2350 A.U and keeps on increasing monotonically to 22600 A.U for wires with 60 nm diameter. All nanowire samples provide a higher Raman intensity compared to the residual unetched neighboring silicon. For the bulk silicon sample and the original unetched SOI wafer, the peak intensities are 10700 and 18200, respectively. The enhancement in the SOI wafer as compared to bulk silicon could happen due to the reflections from the silicon-oxide interface leading to an increased intensity within the top silicon layer. A measure commonly used for comparing Raman scattering from nanowires is the Raman enhancement per unit volume (REV), defined as $REV = (I_{NW}/V_{NW})/(I_{bulk}/V_{bulk})$ where I_{NW} is the intensity for the nanowires, V_{NW} is the volume of the nanowire, I_{bulk} is the intensity from the bulk silicon and V_{bulk} is the volume of the bulk silicon. Since we etched the nanowires on the SOI wafer, REV was calculated with respect to the SOI wafer and is shown in Fig. 3.31. As the volume of the SOI and nanowires is well defined; we do not need to consider the beam penetration for the length terms as has been done in the previous work [33]. I_{NW} is corrected for the signal resulting from the

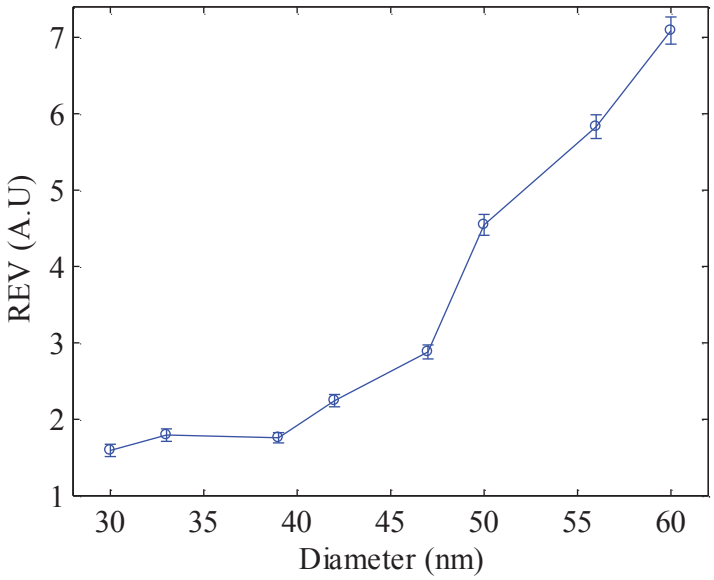

Figure 3.31: REV for different diameter nanowires as compared to that of SOI wafer [3].

residual unetched SOI below the wires. Due to the small diameter and pitch of the nanowires, we are interrogating many nanowires at the same time. This allows for the calculations to be done for a unit cell, defined as 100 $nm \times 100$ nm area, with the nanowire in the center. V_{NW} is simply defined by the cross-sectional area multiplied by the length of the nanowires. V_{bulk} has been defined as the square of the pitch between the wires multiplied by the thickness of the top silicon layer in the original SOI wafer. The silicon layer below the SiO_2 has been ignored, since only a small amount of Raman scattering was observed from the residual silicon neighbouring the nanowire arrays. As seen from Fig.3.31, the REV versus nanowire diameter displays an increasing enhancement for increasing nanowire diameters, with a maximum REV factor of 7.1 over the original SOI. To get REV with respect to bulk silicon wafer, we assumed the beam penetration length in the bulk silicon to be 2 μm dependent on the direct band gap absorption of light at 632.8 nm. With respect to bulk silicon, the REV was 70 for the 60 nm diameter array. The trend in Fig. 3.31 suggests that the filling factor plays a significant role in providing the observed enhancement in the range of SiNW diameters studied. It is interesting to note that the 60 nm diameter wires provided an absolute increase in the intensity over the SOI, and thus the enhancement is real. It is clear that vertically ordered SiNW arrays provide a small enhancement in first order Raman scattering. These findings are in contrast to the

previous study mentioned earlier, where nanowires ranging from $450 - 900\ nm$ in diameter, display a decrease in enhancement with increasing diameter, and a maximum enhancement factor of ~ 100. This may be explained by the fact that nanowires with diameters less than $100\ nm$ act as single mode waveguides, and thus the enhancement characteristics are very different from larger nanowires ($\sim 500\ nm$), which can support multiple modes. While REV is an important parameter for understanding the physics of Raman enhancement, we believe that the actual intensity values are as important from the applications point of view, since devices made of nanowire arrays will ultimately take advantage of this increased intensity. In none of the previous studies which involve nanowire arrays, are the actual Raman scattering intensities mentioned. The $60\ nm$ diameter nanowire array provides an absolute Raman intensity which is larger than the original unetched SOI and the bulk silicon wafers. This absolute increase in intensity can be used to enhance the performance of non-linear optical devices from arrayed nanowires.

The Raman enhancement observed in larger diameter SiNWs has previously been attributed to inelastic scattering of the incident light, and generation of helical surface waves within the nanowires [33]. At smaller diameters in the present study, these helical modes are not observed. Electric field enhancement has previously been used to explain polarization dependence and enhancement of photoluminescence from small diameter ($< 100\ nm$) nanowires [79]. However, in those studies it was assumed that the electric field inside the nanowires is the same constant value independent of the diameter below $100\ nm$. This approximation does not fully explain the present results of increased REV with increasing diameter of nanowires. Additionally, since multiple layers are involved, there are reflections from multiple boundaries which result in Fabry-Perot interferences. In order to simulate the nanowires on a substrate as shown in the schematic in Fig. 3.27(e), the FDTD method was used to quantify the effect of the optical confinement and the interferences from multiple reflections. A plane-wave with a free space wavelength of $633\ nm$ was incident normal to the surface and periodic boundary conditions were used. The simulation was stabilized to the steady-state to account for all of the reflections and their interferences. In the analysis, it was assumed that the results are similar for the incident and Raman wavelengths ($654\ nm$). The amount of reflection from the nanowire surface and optical confinement within the wire are function of the diameter. In Fig. 3.32(a) and (b), the electric field distributions in transverse plane for nanowire arrays of diameters $30\ nm$ and $60\ nm$ are shown visualizing the enhancement due to dielectric mismatch at the boundary. The Poynting vector was calculated and a cut through the diameter for these nanowires is also shown in Fig. 3.32(c). It is clear that the intensity of light is higher in the $60\ nm$ diameter nanowires. Since, Raman intensity is proportional

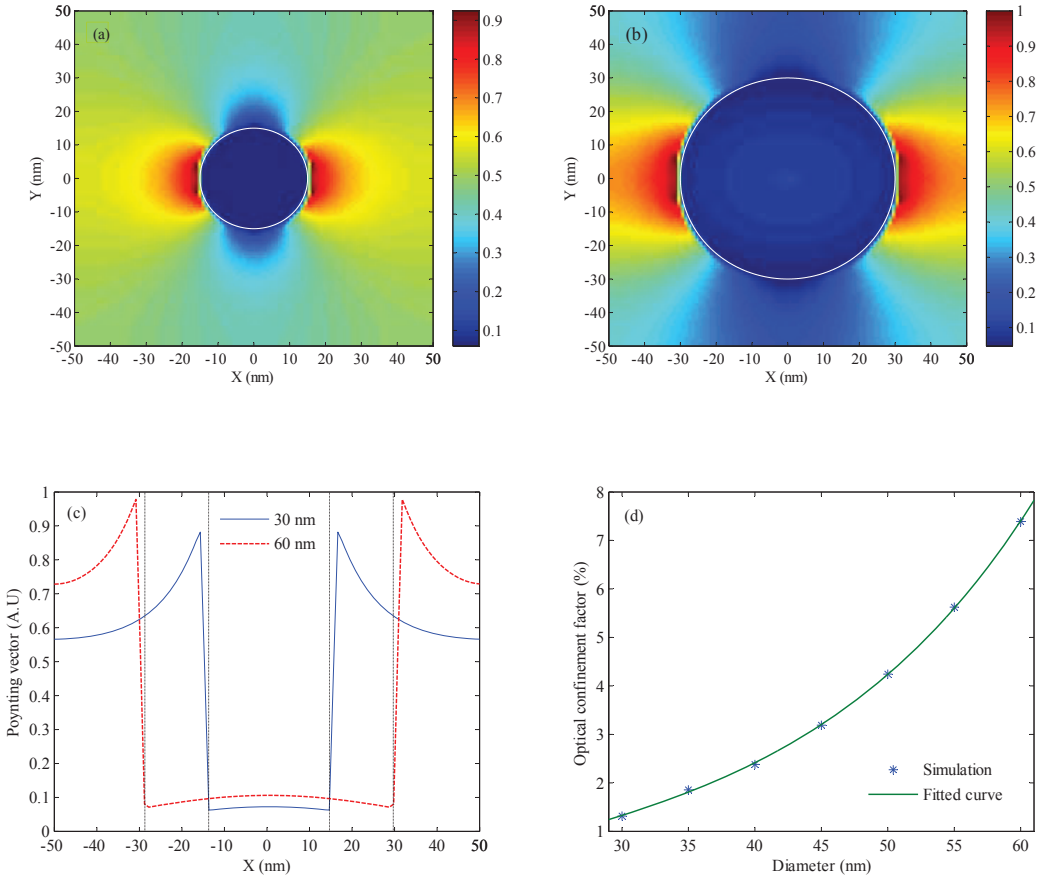

Figure 3.32: (a), (b) Poynting vector distribution in a unit cell of array of nanowires with a pitch size of 100 nm and a diameter of (a) 30 nm and (b) 60 nm. (c) Cut of Poynting vector through the center along x-direction for both diameters. (d) Optical confinement factor versus diameter [3].

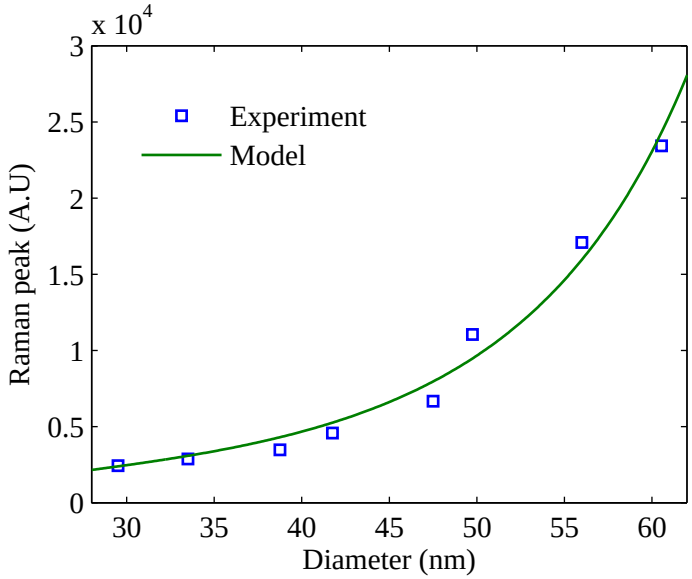

Figure 3.33: Experimental and simulated Raman peak intensities as a function of the diameter of the nanowire [3].

to the electric field intensity, 60 nm diameter nanowires should have a larger REV, which is observed experimentally. From these simulations, the optical confinement factor (normalized amount of the optical power confined within the nanowire) was calculated and plotted in Fig. 3.32(d). As the diameter is increased, the optical confinement factor increases rapidly. Dividing the confinement factor by the area of the nanowire gives the average intensity of the electric field within the nanowire. Since for a given diameter, the electric field is not changing much within the nanowire, this approximation should not result in significant error. If R is the total reflection of the surface of the nanowires, then the Raman intensity per unit volume can be written as:

$$\frac{I}{V} = \kappa(1-R)^2(\frac{\Gamma}{A})^2 \tag{3.8}$$

where I is the intensity, κ is an empirical constant depending on the efficiency of Raman scattering, Γ is the confinement factor, and A and V are the area and the volume of the nanowires, respectively. Figure 3.33 shows the experimentally obtained values of peak intensity as a function of nanowire diameter along with the values predicted by the model. The constant κ was determined once for the nanowires of 30 nm diameter and then kept the same for all other calculations. The predicted

values from the model match the experimental results remarkably well. Electric field enhancement, due to the increased confinement of light, for increasing diameter of nanowires can be used to understand enhanced Raman scattering from SiNW in arrays.

In [33], they have shown as the nanowires diameter was increased, the REV decreased very quickly. However, our results showed an opposite trend in which the REV increases with increasing diameter was observed. This strongly suggests that there should be an optimal diameter for which the nanowires will generate the maximum Raman scattering, due to maximum confinement of light. This is the topic of next discussion.

Optimizing Raman Scattering Enhancement by Changing Nanowires Parameters

In this section, SiNWs with varying diameters, pitches and lengths are investigated for Raman enhancement. An increase in absolute intensity of Raman by a factor of 15 was achieved for 1.1 μm long SiNWs with diameters of 150 nm and pitch of 400 nm. An oscillatory behaviour in the Raman intensity was also observed with diameter, which is a result of constructive and destructive interferences within the array. This is the first time that oscillatory behaviour in the Raman scattering intensity as a function of nanowire diameter is observed, which has been previously predicted by theoretical models [32]. For nanowires with length of 800 nm a maximum REV of 723 is achieved for SiNW diameters around 135 nm, and was found to be independent of the pitches studied. The experimental REV results are supported and modelled quantitatively using FDTD simulations.

In the first experiment, nanowires of length 800 nm were investigated. Figure 3.34 (a) shows the actual peak Raman intensities measured from SiNW arrays as the diameter and pitch was changed. The intensity from bulk silicon is shown as a dashed horizontal line for comparison and is 3787 arbitrary units (A.U). Highest peak intensity of 47564 A.U. was achieved for nanowires with diameter of 135 nm with pitch of 400 nm. An increase by a factor of 12 was achieved in actual peak intensities, which is 6 times higher than the maximum value reported in previous section. For the nanowires with a pitch of 200 nm, the intensity monotonically increases with increasing diameter. For the other pitch values, the intensity shows an oscillatory behavior with diameter. For SiNWs arranged 400 nm apart, the maximum Raman intensity is achieved at a diameter of 135 nm. For diameters which deviate slightly from this value, a sharp drop in the intensity is observed. Overall, for nanowire

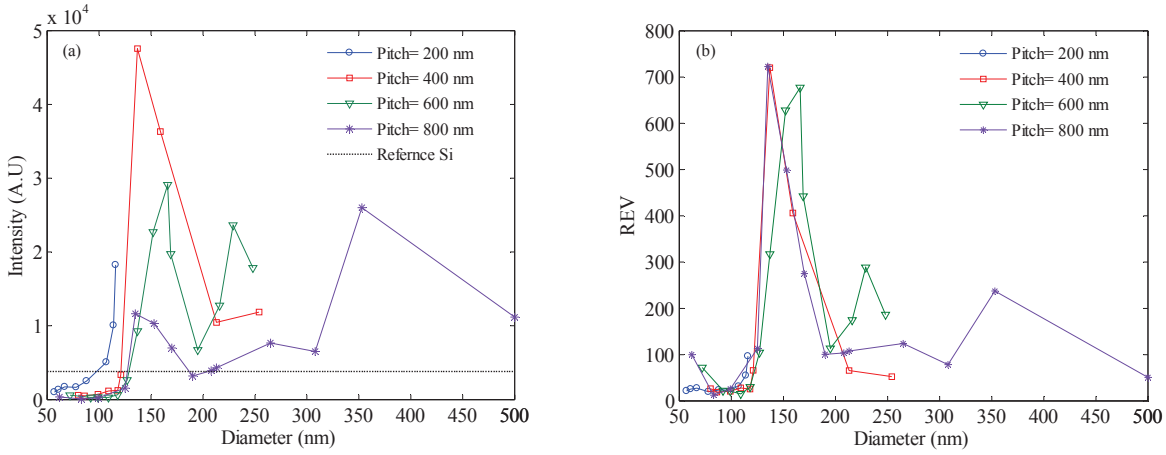

Figure 3.34: (a) Raman intensity versus diameter for different pitches. Raman intensity of silicon is shown as a reference. (b) REV versus diameter for different pitches as compared to that of Si wafer for two different samples.

diameters above 120 nm, the peak intensity is consistently larger than that of bulk silicon. A 600 nm spacing results in two peaks at diameters of 166 and 229 nm, and at diameters of 135 nm and 353 nm for an 800 nm pitch. Figure 3.34 (b) shows the calculated REV for the samples in Fig. 3.34 (a). A maximum REV of 723 times is achieved for diameters 135 nm whether the pitch is 400 nm or 800 nm. The calculated REV is always greater than that of Si for all the samples due to the dielectric mismatches which are occurring at the Si-Air interfaces. REV for a wire spacing of 600 nm is at a maximum for a diameter of 166 nm. However, this array did not have a diameter close to 135 nm and it is unknown whether the point was missed. Interestingly for a pitch of 800 nm, the highest REV is not achieved at the diameter with the highest absolute intensity. Hence, while REV is important to understand why enhanced Raman is achieved, it may not give the complete picture from the application point of view. For example, if the goal is to achieve highest Raman scattering, then for pitch of 800 nm, a diameter of 353 nm is more appropriate as compared to 135 nm where the highest REV is achieved.

In the second experiment, the length of the nanowires was increased to 1.1 μm from 800 nm. Only the pitch of 400 nm was considered for this study. Also, diameters were fabricated with a 5 nm variation in order to appreciate how the Raman intensity changes around points of interest. Figure 3.35 shows the peak intensities as the diameter is changed for the array. Intensity from bulk silicon is also shown as a reference. A maximum peak intensity of 59427 $A.U.$ was observed for the diameter

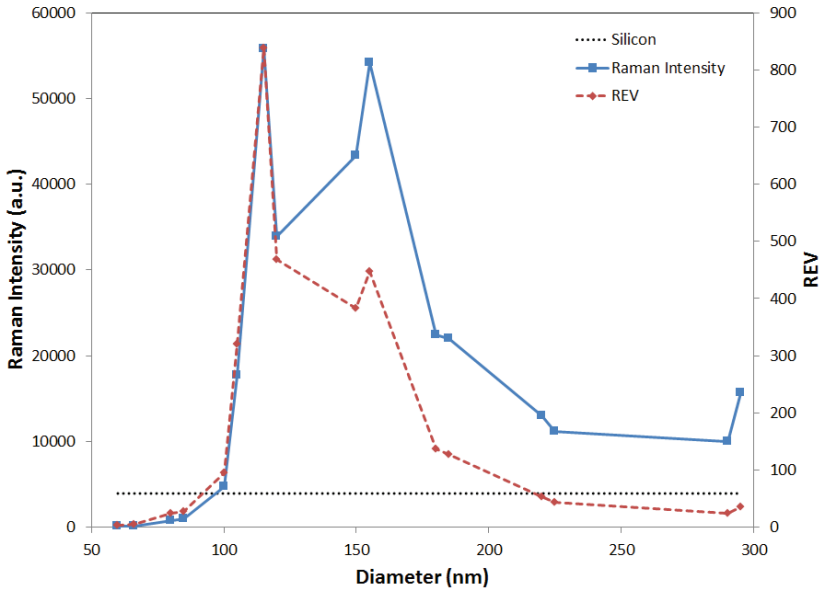

Figure 3.35: Raman intensity and REV versus diameter for pitch size of 400 nm. Raman intensity of silicon is shown as a reference.

of 115 nm, corresponding to an intensity increase by a factor of 15 compared to bulk silicon. Figure 3.35 also plots the REV for the same sample, where a maximum REV of 838 was obtained from the arrays. This represents one of the highest REV factors reported from vertical SiNW arrays. For shorter length nanowires, the diameter at which the maximum REV is achieved is larger by about 20 nm. Additionally the Raman intensities peak at two different diameter values: 115 nm and 155 nm. Interestingly as the diameter is changed from 100 nm to 120 nm, sharp changes in Raman intensities and REV factors are observed, suggesting that the electromagnetic coupling within the array is very sensitive to the diameter.

In order to understand the enhancement observed in the Raman spectra, SiNWs can be modelled as cylindrical optical waveguides. When they are placed together in an array, electromagnetic coupling between the neighboring nanowires allows for increased confinement within the SiNW, thereby increasing the electric field intensity. In order to gain further insight, FDTD simulations were carried out for semi-infinite nanowires with varying diameters. Figure 3.36 shows the electric field distributions within the nanowires for diameters of 100, 115, and 130 nm. At 115 nm, a high confinement of the electric field is observed. Calculated confinement factors as the diameters are increased are plotted in Fig. 3.37 . An increasing diameter should

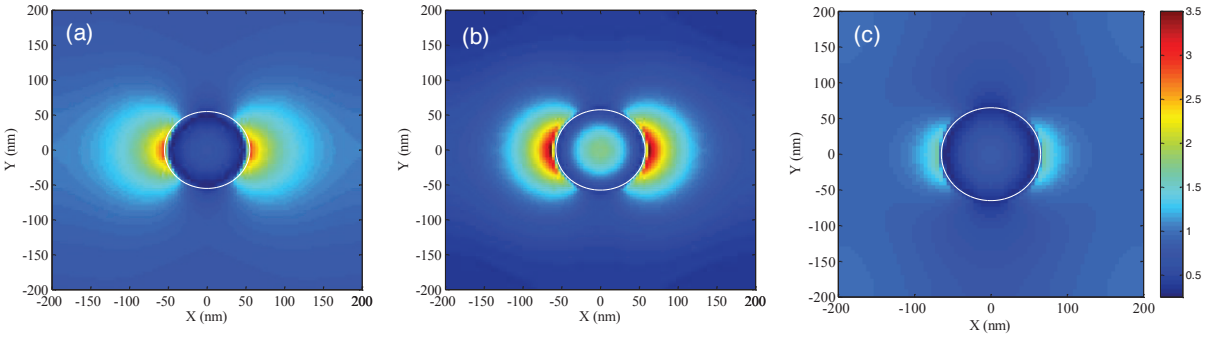

Figure 3.36: FDTD simulations for the electric field distributions for the diameters of (a) 100 nm, (b) 115 nm, (c) 130 nm. The simulations were carried out for semi-infinite nanowires.

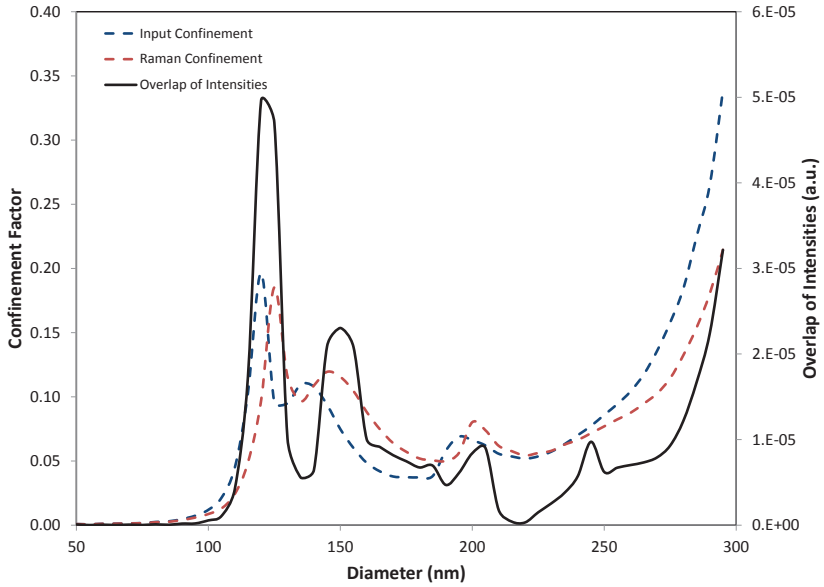

Figure 3.37: Calculated confinement factors for the input signal and the Raman signal as the diameter of the nanowires is changed.

result in the confinement factor within each SiNW to increase. However, when the nanowires are considered to be in an array, an increase in confinement factor occurs at the diameter of 120 nm due to constructive coupling between the nanowires. Further, the nanowire arrays also act like a Fabry- Perot cavity due to the reflections from the SiNW/air and SiNW/silicon interface. The SiNW arrays represent an effective medium which will have a refractive index that will vary with different diameters, and consequently the Fabry- Perot resonances peaks also shift with diameter. Such a shift would result in the diameters where maximum enhancement is achieved to vary with changing length. This idea is validated because the 800 nm long nanowires display a maximum REV at a diameter of 135 nm, whereas the 1.1 μm long nanowires have the maximum REV at 115 nm. It is well known that the Raman scattering intensity is directly proportional to the intensity of the incident field applied. It has been demonstrated that due to increased confinement of the incident field within a small area, an enhancement of the Raman signal can be observed. However, since a resonant structure is used, the enhancement will be different for the Raman scattered and incident light. In this connection, referring to Fig. 3.37, the maximum confinement factor is shifted to a larger diameter. In a recent work [80], Raman enhancement has been modelled by multiplying the local intensities of the incident beam and the Raman signal for a single nanowire. A similar methodology was adopted here. FDTD simulations were conducted to calculate the electrical field distributions for the incident beam and the Raman signal. The model was modified to also include the effect of the Fabry-Perot cavity. First, the nanowires were assumed to be semi-infinite to only consider the effect of the coupling. The intensity of the light for the two different wavelengths was locally calculated as a proportion of $|E_{i,R}|^2$,where $|E_i|$ and $|E_R|$ are the electric field amplitudes for input and Raman signals, respectively. The effect of the overlap was calculated as $|E_i|^2|E_R|^2$ for each grid point within the cross-section. Nanowires below the diameter of 150 nm act like single mode waveguides, and the distributions for both the input and the Raman signals are similar. However, as the diameter is increased, the waveguides become multi-mode, and the resultant electric field distributions start to become localized within the nanowires. The degree of this localization is different for the incident and the Raman signals. Thus, while the confinement factor increases, the overlap between the individual elements actually decreases. The normalized overlap of the optical intensity over a nanowire was calculated as:

$$OL = \frac{\Sigma_{nanowire}|E_i|^2|E_R|^2}{\Sigma_{unitcell}|E_i|^2 \times \Sigma_{unitcell}|E_R|^2} \tag{3.9}$$

The value of OL is also plotted in Fig. 3.37. The highest value is achieved

at a diameter of 120 nm, approximately at the average of the peak values for the confinement of the input and Raman signals. However, the REV at 120 nm is lower than that of 115 nm. This is where the Fabry- Perot cavity comes into effect. A new simulation was performed to calculate the transmission through the nanowires in the cavity. Direct band gap absorption has previously been neglected in the Raman studies of these nanowires [3]. In these simulations, the absorption value of the nanowires is taken into account. Due to a Fabry-Perot resonance, the transmission through the 115 nm diameter NWs is larger than the transmission through 120 nm diameter NWs, resulting in an increased REV. The REV factors were estimated by the following calculations:

$$\frac{I}{V} = \kappa \frac{OL}{A^2} T_i T_R \tag{3.10}$$

where I is the intensity of the Raman, V is the volume of the nanowires, A is the cross-sectional area of the nanowires, T_i and T_R are the transmission through the nanowires for the incident and Raman wavelengths, respectively, and κ is an empirically determined factor. The overlap term OL was divided by the square of A to get an average intensity over the nanowire diameter. The constant was calculated for the diameter of 60 nm, and held fixed for the simulations involving other diameters. The comparison of the model with the experimental results is plotted in Fig. 3.38. A very good match with the experimental data is observed over the complete diameter range. All the features within the nanowires are well accounted for with the methodology presented. Figure 3.38 also plots the modeled results by using only the individual confinement factors as has been previously reported [3]. A good match is obtained with the experimental data except for the diameters around 130 nm. As can be seen in Fig. 3.36(c), the electric field confinement is very weak for the incident signal at this diameter. Since this is a resonance effect attributed to electromagnetic coupling between the nanowires, it is therefore sensitive to input wavelength. This effect is captured by the overlap of the intensities, which reduces the modeled REV considerably. When considering the individual CFs for both the incident and Raman scattered light, even though the CF is reduced for the input electric field, the CF associated with the Raman signal is still high, and smaller changes in REV are expected.

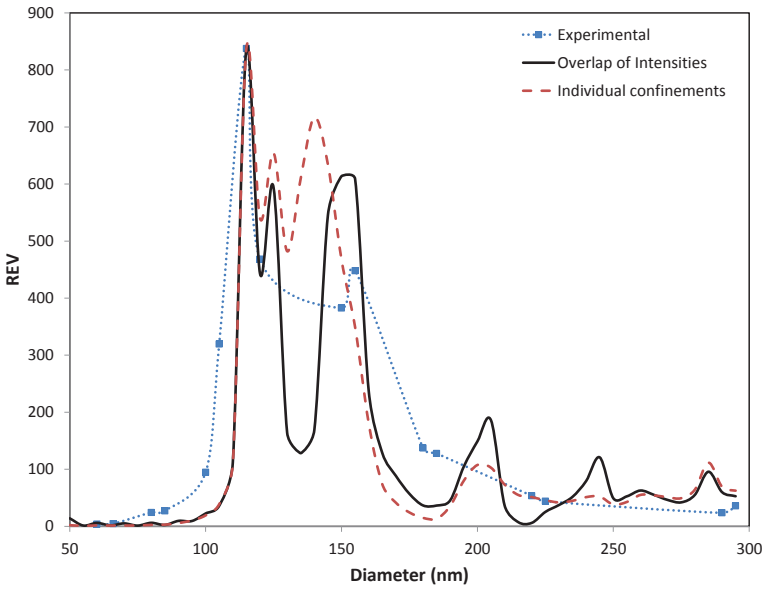

Figure 3.38: Modeled REV versus the experimental results showing very good agreement over the complete diameter range. The expected values if the confinement of individual fields was considered is also plotted.

Chapter 4

Silicon Nanowire Optical Waveguide (SNOW)

In this chapter, a novel optical waveguide is proposed consisting of arrays of Silicon Nanowires (SiNWs) in close proximity. It is shown that such a structure can guide an optical mode provided the electric field is polarized along the length of the nanowires. Furthermore, such guidance can happen even if the nanowires are arranged randomly albeit at a higher scattering loss. On the other hand, high radiation losses are observed if the electric field is polarized in the transverse direction to the nanowires. The optical radiation loss is calculated for different structures using Finite Difference Time Domain (FDTD) method. In all simulation optical communication wavelength of 1550 nm is assumed. It is also shown that the arrayed nanowire region can be approximated using an effective-index bulk waveguide. The approximation allows for design and optimization of optical structures using integrated optics methodology resulting in significant savings in time and resources. The advantage of the proposed waveguide structure is that it allows for increased optical confinement while using the enhanced optical interactions of nanowire structures compared to single nanowire photonic waveguide for smaller diameter where nanowire is a poor waveguide. For the SiNW with a diameter of 50 nm, an optical confinement factor of 33 % was achieved in the proposed waveguide as opposed to 0.1 % that is achieved for a single nanowire photonic waveguide. A radiation loss of 0.12 cm^{-1} is achieved for nanowires of the same diameter spaced 75 nm apart. While our analysis is done on SiNWs at 1550 nm, the proposed structures can be extended to other materials and wavelength regimes which can find various applications.

4.1 Motiviation

In recent years, silicon photonics has offered low cost optoelectronic solutions for applications ranging from telecommunications, biosensing to chip-to-chip interconnections. As such various devices have been demonstrated on silicon like optical amplifiers [12], modulators [13], optical switches [81, 82] and four-wave mixers [83]. Most of the demonstrated devices use silicon ridge waveguides with small cross-sectional dimensions of approximately 450 $nm \times 250$ nm to increase the optical confinement [84, 85]. This allows for designing waveguide bends with reduced diameters and increased diffusion of carriers in optical switches reducing the effective carrier lifetime [82]. An etchless process in the fabrication of such waveguides has also been demonstrated in order to reduce the loss due to scattering from sidewall roughness [86]. These devices take advantage of the increased optical fields within the core of the waveguide. Using a comprehensive theory for describing the nonlinear propagation of optical pulses through silicon waveguides including the effects of polarization, increased nonlinear effects have been calculated for waveguide geometries with high confinement [87]. However, the fundamental material properties of the silicon do not change in this regime. Further reduction in the dimensions of the silicon core is not possible as below a certain dimension, the optical mode starts to loose confinement [88]. An extension to these works by going to the regime of nanowires is promising because it has been observed that different optical-carrier interactions are enhanced in the nanowire regime due to the quantum confinement and increased optical intensity. Nassiopoulos *et al.* [21] and Huo *et. al.* [22] have demonstrated room temperature electroluminescence from SiNWs of diameters smaller than 10 nm due to band-to-band electron-hole recombination. Cloutier *et al.* [89] have shown optical gain and stimulated emission in a periodic nanopatterned-silicon structure at cryogenic temperatures. In addition, Chen *et al.* [90] have reported stimulated emission at a bandgap energy of 1.1 eV in a nanostructured silicon p-n junction diode using current injection at room temperature. Shiri *et al.* [91] have theoretically shown that for SiNWs smaller than 10 nm in diameter, direct bandgap is achieved and the bandgap can be switched from direct to indirect by application of strain. Nonlinear effects of bulk silicon can also be enhanced using nanosized structures. It has been experimentally shown that the spontaneous Raman scattering can be enhanced by three orders of magnitude using SiNWs and silicon nanocones instead of bulk silicon provided the nanowire diameter is less than 130 nm [32]. As shown in previous chapter an enhanced second order nonlinear signal can be achieved using SiNWs. Furthermore, SiNWs due to their large surface area have found promising applications in biosensing area. For example, Li *et al.* [92] have demonstrated highly

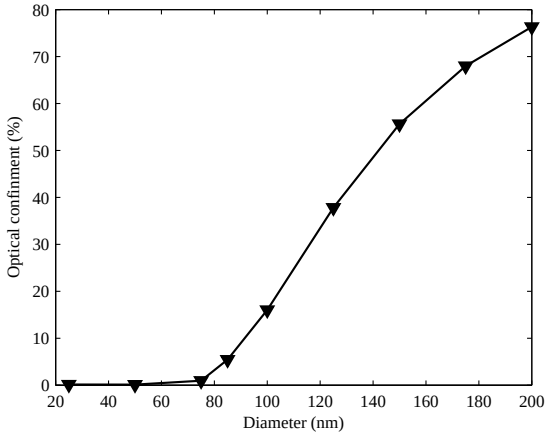

Figure 4.1: Optical confinement factor versus diameter of single nanowire silicon waveguide surrounded by air at wavelength of 1550 nm [4].

sensitive and sequence-specific DNA sensors using SiNWs. SiNW-based biosensors have also shown fast response and high sensitivity to glucose [45]. Zhu *et al.* [93] have reported p-n junction diode arrays on a Si substrate which could find promising applications in nanoelectronics and optoelectronics.

An important criterion of nanowires for applications in optoelectronics devices is the guidance of light through them. Barrelet *et al.* [94] have explained an approach for guiding and manipulating light in sub-wavelength Cadmium Sulfide (CdS) nanowires with diameter of 200 nm. They have also quantitatively investigated losses through straight and bent single nanowire waveguides. Also, it has been shown that semiconducting nanowires can work as nanoscale lasers [95], where high refractive-index contrast between the nanowire and surrounding media provides an optical cavity for lasing. Most of these works consider nanowires of several 100 nm in diameter. However, the increased material properties in SiNWs described above are only observed for diameters less than 100 nm. A main disadvantage of SiNWs is the lack of optical confinement especially when the diameter is less than 100 nm. Using a single nanowire as an optical waveguide suffers from two main issues, namely, low coupling efficiency and low optical confinement. While the low coupling efficiency may be corrected using tapers [88], the devices still suffer from critical alignment tolerances making their practical applications a suspect for photonics. Figure 4.1 shows the calculated confinement factor for a SiNW surrounded by air as the diameter of the nanowire is changed. The free-space wavelength for this calculation is 1550 nm. The confinement factor was calculated by solving for the eigen mode

of a silicon cylinder using Full-Vectorial Beam-Propagation method and calculating the optical power ratio within the silicon core. As the diameter of the nanowire is reduced below 75 nm, optical confinement factor starts to decrease appreciably and is less than 1 %. The low confinement factor results in the fact that though the intrinsic properties of nanowires increase, the overall device performance is not greatly enhanced [96]. As such, there has been some work in increasing the confinement in nanoscale devices. Plasmonic waveguides consisting of metal nanoparticles have been considered as optical waveguides [97, 98]. In principle metal nanoparticles can be attached to the surface of nanowires to increase the confinement factor. However, such waveguides suffer from increased optical loss. For example, transmission losses through nanoparticles due to resistive heating is about 6 $dB/\mu m$ [98], while still having critical alignment requirements. Further, the increased optical interactions have been observed when the electric field is polarized along the length of the nanowires [99]. This suggests that a single nanowire waveguide will not be able to take advantage of the increased effects as the major component of the electric field needs to be transverse to the direction of propagation, which in a single nanowire waveguide is along the length of the nanowire.

To overcome aforementioned issues, a novel optical waveguide is proposed consisting of closely packed arrays of SiNWs on a Silicon-on-Insulator (SOI) substrate. In the region where the diameter of the nanowires is much less than the free-space wavelength, the nanowires act like meta-material inclusions [100]. It is shown that such a structure can guide an optical mode, provided the electric field is polarized along the length of the nanowires (the same polarization for which enhanced optical interactions are observed in nanowires). Furthermore, the guidance happens even if the nanowires are randomly arranged, albeit with an increased loss. We also show that the SiNW region can be approximated by an effective index using a weighted average method. This allows us to use conventional waveguide methods to design and optimize the waveguide structures resulting in significant savings of resources and time. The advantage of our proposed structure is that it allows us to use the enhanced optical interactions of SiNWs while achieving optical confinement and coupling efficiency of conventional optical waveguides. In our designs, we consider crystalline-SiNWs with diameters of tens of nanometers and lengths of 1 micron, which are achievable with current nano-fabrication techniques [48, 101, 102]. Since the nanowires can be placed randomly, maskless methods of creating SiNWs demonstrated for solar cells [103] can also be applied for fabricating the waveguides resulting low-cost fabrication.

The rest of this chapter is organized as follows. In section 4.2, we conceptually describe the proposed device structure. Further, we simulate light interaction with single SiNW for different diameters and polarization to understand the conditions

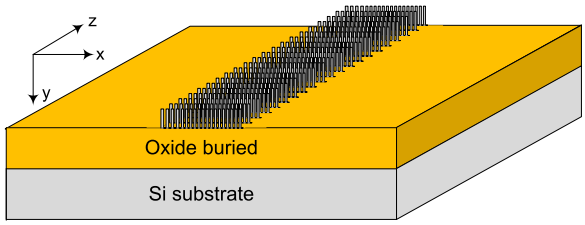

Figure 4.2: 3-D schematic diagram of SOI rib waveguide using arrays of SiNWs [4].

for which our proposed device will work. Then, we simulate the proposed structure for different SiNW diameters and nanowire spacing. Furthermore, we introduce the effective index method for the SiNW region. In section 4.3, we show this structure can guide the light even over a bend. As an application, we design a biosensor using proposed waveguide and results are presented in section 4.4.

4.2 Silicon Nanowire Optical Waveguide (SNOW)

The proposed structure is shown in Fig. 4.2. A SOI wafer is considered as a starting substrate and etched into an array of nanowires. In the vertical direction, the refractive index difference between the silicon and insulator substrate allows for transverse guiding of the optical signal. Since the goal is to increase the optical confinement factor within the SiNWs, the length of the nanowires needs to be large to have high confinement in the vertical direction. We have considered nanowires of 1 μm length which provides greater than 95% confinement in the vertical direction. In the lateral direction, if the nanowires are placed closed together, the optical mode will see an average refractive index, higher than the surrounding, thereby guiding light. The proposed structure may look similar to Photonic Bandgap (PBG) structures. However, there is no bandgap as in PBG, and the nanowire scattering points are much smaller than the ones used in PBG (at least $5-10$ times smaller), in the range where increased optical effects have been observed in SiNWs. In order for the structure to work effectively with low radiation loss, an individual nanowire should not diffract the light. This can be observed if the phase front of an optical wave passing through them is not distorted. So it is instructive to look into how an optical wave interacts with a single nanowire and whether a condition can be achieved where the phase is not modified by the SiNW. While this may not provide a quantitative analysis, it does help to conceptualize how the proposed structure is working and the regime in which it will work well. For the calculations, free-space wavelength of 1550 nm is

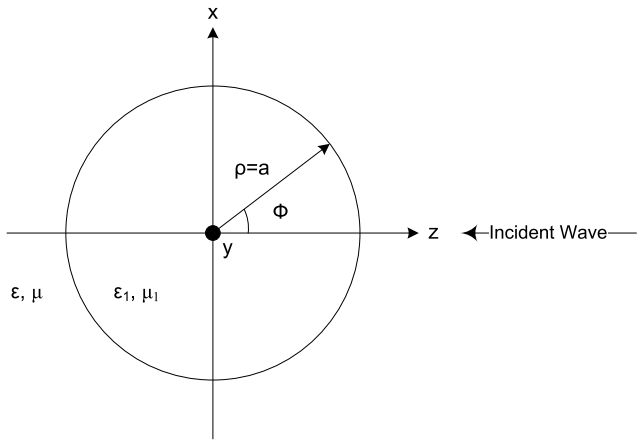

Figure 4.3: Cross section of the SiNW cylinder, a is the radius of the nanowire [4].

considered. However, the analysis can be easily extended to other wavelength regimes or different materials.

4.2.1 Light interaction with single SiNW

We are interested in how the SiNW alters the amplitude and phase front of an optical wave incident along the perpendicular-cross-sectional plan of the SiNW, shown in Fig. 4.3. Since it is interesting to see how the SiNW scatters light in the x-z plane, the SiNW is considered to be infinite in the y-direction, parallel to the nanowire. A plane wave is incident on the nanowire from the z-direction. Cylindrical co-ordinates are used to solve the problem. This kind of interaction can be treated as a scattering problem because of the small diameter of the nanowire compared to the wavelength used for the analysis i.e. 1550 nm. Due to the cylindrical shape of the nanowire, the scattering problem is a canonical boundary value problem. Such a problem can be solved by separation of variable approach and the solution is dependent on the polarization of input electric field.

For the case when the electric field is polarized in the y-direction ($H_y = 0$ and $E_y \neq 0$), the problem can be considered to be 2-dimensional. Assuming $E_y \neq 0$ results in nonzero E_y, H_ρ, and H_ϕ components. The incident magnetic vector potential is chosen as a plane wave propagating along the z direction:

$$A_y^i = e^{-ikz} = e^{-ik\rho cos\phi} \tag{4.1}$$

resulting in an incident electric field of:

$$E_y^i = E_0 e^{-ikz} \tag{4.2}$$

By choosing cylindrical coordinates the incident field will be a periodic function of ϕ with a period of 2π. Due to the periodicity of incident magnetic vector potential $A_y^i(\rho, \phi)$, it can be expanded as a Fourier series,

$$A_y^i(\rho, \phi) = \sum_{n=-\infty}^{\infty} B_n e^{in\phi} \tag{4.3}$$

where

$$B_n = \frac{1}{2\pi} \int_0^{2\pi} e^{-ik\rho cos\phi - in\phi} d\phi = i^{-n} J_n(k\rho) \tag{4.4}$$

thus $A_y^i(\rho, \phi)$, is given by:

$$A_y^i(\rho, \phi) = \sum_{n=-\infty}^{\infty} i^{-n} J_n(k\rho) e^{in\phi} \tag{4.5}$$

When the incident field hits the SiNW, some part of it will be scattered, A_y^s, and the other part, A_y^t, will be transmitted through the SiNW. The scattered magnetic vector potential A_y^s has to satisfy Helmholtz equation while $\rho \geq a$ and $k = \omega\sqrt{\mu\varepsilon}$.

$$[\frac{1}{\rho}\frac{\partial}{\partial\rho}(\rho\frac{\partial}{\partial\rho}) + \frac{1}{\rho^2}\frac{\partial^2}{\partial\phi^2} + k^2]A_y^s(\rho, \phi) = 0 \tag{4.6}$$

Equation (4.6) can be solved using the separation of variables technique. Thus, the scattered magnetic vector potential will be a Hankel function of the first kind [104]:

$$A_y^s(\rho, \phi) = \sum_{n=-\infty}^{\infty} i^{-n} a_n H_n^{(1)}(k\rho) e^{in\phi} \tag{4.7}$$

which is an outward traveling wave fading out as the distance from the SiNW increases. Similar solution leads to the transmitted magnetic vector potential as follows [104]:

$$A_y^t(\rho, \phi) = \sum_{n=-\infty}^{\infty} i^{-n} b_n J_n(k_1\rho) e^{in\phi} \tag{4.8}$$

Considering continuity of tangential electric and magnetic field at the boundary a_n and b_n can be determined. Therefore, substituting $A_y^i(\rho,\phi)$, $A_y^s(\rho,\phi)$, and $A_y^t(\rho,\phi)$ from previous equations to the following equation:

$$E_y = \frac{i}{\omega\mu\epsilon}(\frac{\partial^2}{\partial z^2} + k^2)A_y \qquad and \qquad H_\phi = -\frac{1}{\mu}\frac{\partial A_y}{\partial \rho} \tag{4.9}$$

and by considering continuity of E_y and H_ϕ at $\rho = a$, a_n will be obtained as:

$$a_n = \frac{\sqrt{\frac{\epsilon}{\mu}}J_n'(K_1a)J_n(ka) - \sqrt{\frac{\epsilon_1}{\mu_1}}J_n'(k_1a)J_n(ka)}{\sqrt{\frac{\epsilon_1}{\mu_1}}J_n'(k_1a)H_n^{(1)}(ka) - \sqrt{\frac{\epsilon}{\mu}}J_n(k_1a)H_n^{(1)'}(ka)} \tag{4.10}$$

similarly for b_n, we have:

$$b_n = \frac{\sqrt{\frac{\epsilon}{\mu}}H_n^{(1)}(k_a)J_n'(ka) - \sqrt{\frac{\epsilon}{\mu}}H_n^{(1)'}(k_a)J_n(ka)}{\sqrt{\frac{\epsilon_1}{\mu_1}}J_n'(k_1a)H_n^{(1)}(ka) - \sqrt{\frac{\epsilon}{\mu}}J_n(k_1a)H_n^{(1)'}(ka)} \tag{4.11}$$

$$= \frac{-\frac{2i}{\pi\omega\mu a}}{\sqrt{\frac{\epsilon_1}{\mu_1}}J_n'(k_1a)H_n^{(1)}(ka) - \sqrt{\frac{\epsilon}{\mu}}J_n(k_1a)H_n^{(1)'}(ka)} \tag{4.12}$$

Using the mentioned equations, the total electric field distribution in amplitude and phase is solved for different diameters ranging from 600 nm to 20 nm. The amplitude of the electric field is shown in Fig. 4.4 for different diameters whereas the phase distribution is shown in Fig. 4.5.

The wavelength of the incident light is 1550 nm within the telecom regime. For wider nanowires, some part of electric field is scattered and another part is coupled to the SiNW. This coupled part transmits through the SiNW and again at the boundary of SiNW and air experiences scattering and transmission. The coupled part sees a multi-mode interference effect to give a spatial interferometric distribution. If the nanowire diameter was further increased, whispering gallery modes [105] were clearly observed. The diffraction is also seen in the phase plot for the larger nanowires. As the phase is altered outside the nanowires, if the larger diameters are placed together, constructive or destructive interference can take place. PBG structures operate based on this diffraction. However, the picture interestingly changes when the nanowire diameter is less than 100 nm. This is observed in both the amplitude and phase. The change of the electric field inside and around of SiNW is small. Also

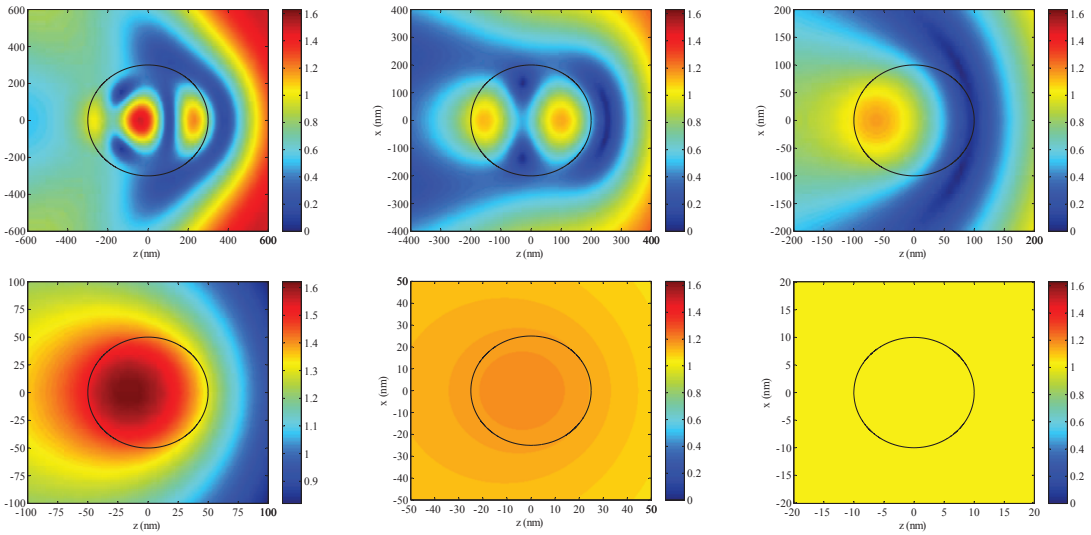

Figure 4.4: Amplitude of electric field in y direction (E_y) for SiNWs with diameters of (from top to right) 600 nm, 400 nm, 200 nm, 100 nm, 50 nm and 20 nm, at wavelength of 1550 nm [4].

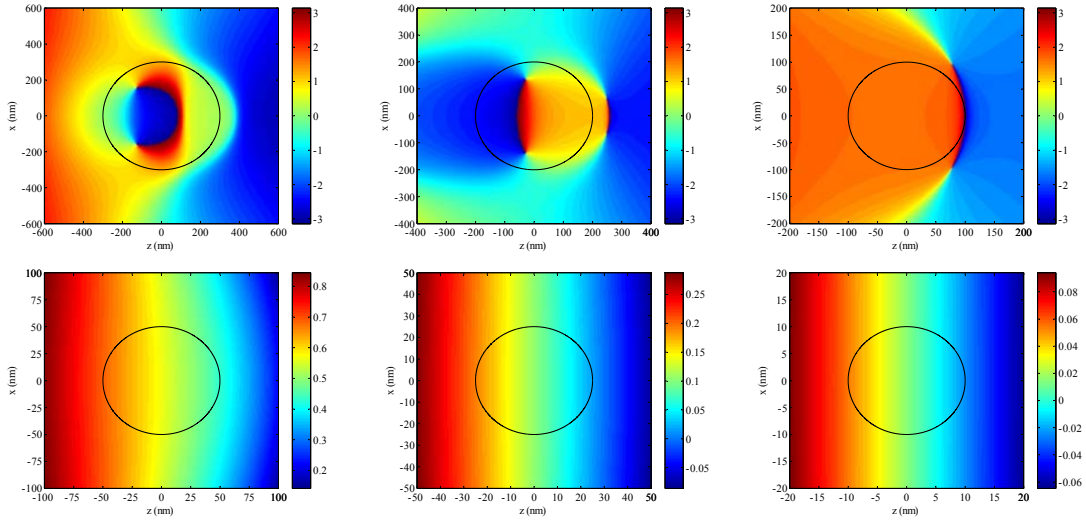

Figure 4.5: Phase of electric field in y direction (E_y) for SiNWs with diameters of (from top to right) 600 nm, 400 nm, 200 nm, 100 nm, 50 nm and 20 nm, at wavelength of 1550 nm [4].

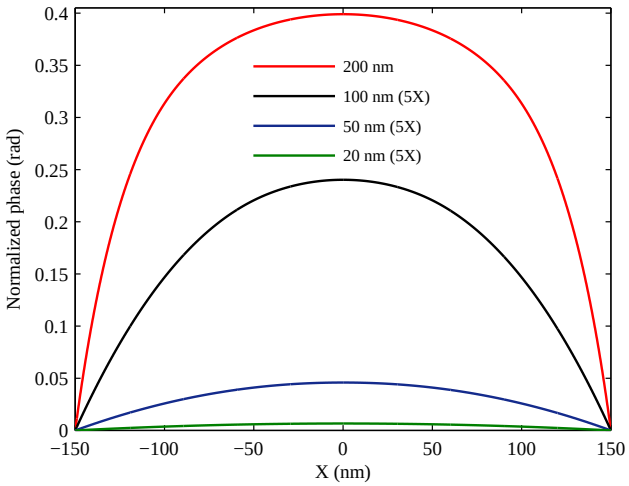

Figure 4.6: Cross-section of the phase front at the center of the SiNWs with diameters of 200 nm, 100 nm, 50 nm and 20 nm, at wavelength of 1550 nm [4].

the phase front is not modified by the nanowire. In fact for a diameter of 20 nm and 50 nm, there is negligible distortion of the phase of the electric field. This can be observed from Fig.4.6 which plots the cross-section of the phase front at the center of the nanowire. For this figure, the magnitude of the phase front for nanowires of smaller diameters has been multiplied by a factor of 5 for ease of visualization. It is observed from the figure that the phase front is nearly flat for diameters of 50 nm and 20 nm. This suggests that for these diameters, our proposed SNOW structure will work effectively if the electric field is polarized along the length of the nanowire. It is also instructive to look into how the interaction happens when the magnetic field is polarized along the length of the nanowire ($E_y = 0$ and $H_y \neq 0$). The incident electric vector potential is chosen like the previous case and the solution steps are also similar. Figure 4.7 and Fig. 4.8 show the amplitude and phase of the interacting magnetic field for different diameters, respectively. For this polarization it is observed that phase distortion happens even when the diameter of the SiNW is 20 nm. We believe that this is due to the discontinuity of the electric field along the boundary and the discontinuity changes as the field propagates through the nanowire. This suggests that the SNOW structure will be a poor guiding medium for this polarization of optical wave. For most of the applications, this is not an issue as the enhanced optical interactions which we want to take advantage of are also observed in the $E_y \neq 0$ polarization.

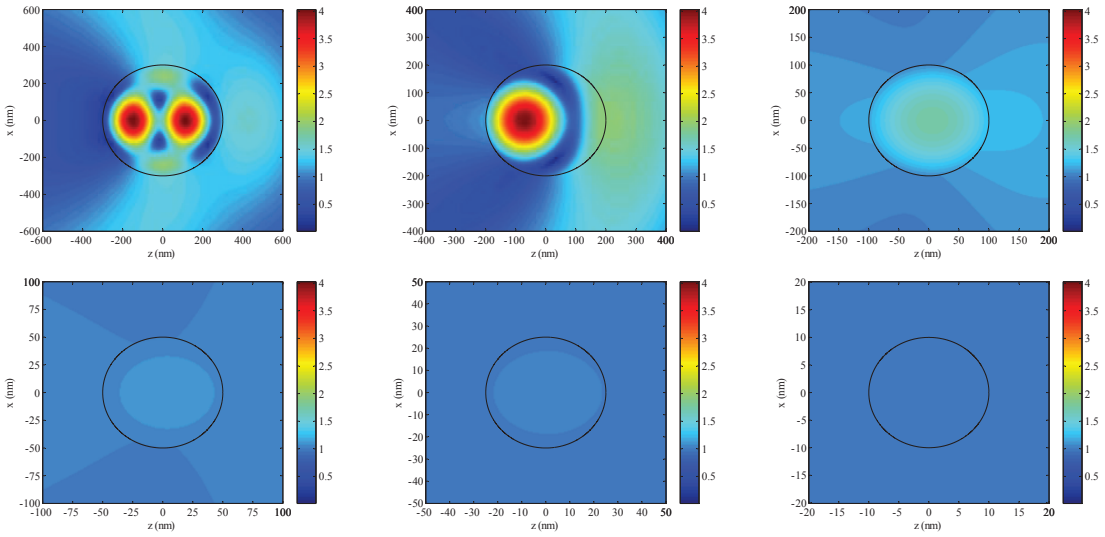

Figure 4.7: Amplitude of magnetic field in y direction (H_y) for SiNWs with diameters of (from top to right) 600 nm, 400 nm, 200 nm, 100 nm, 50 nm and 20 nm, at wavelength of 1550 nm [4].

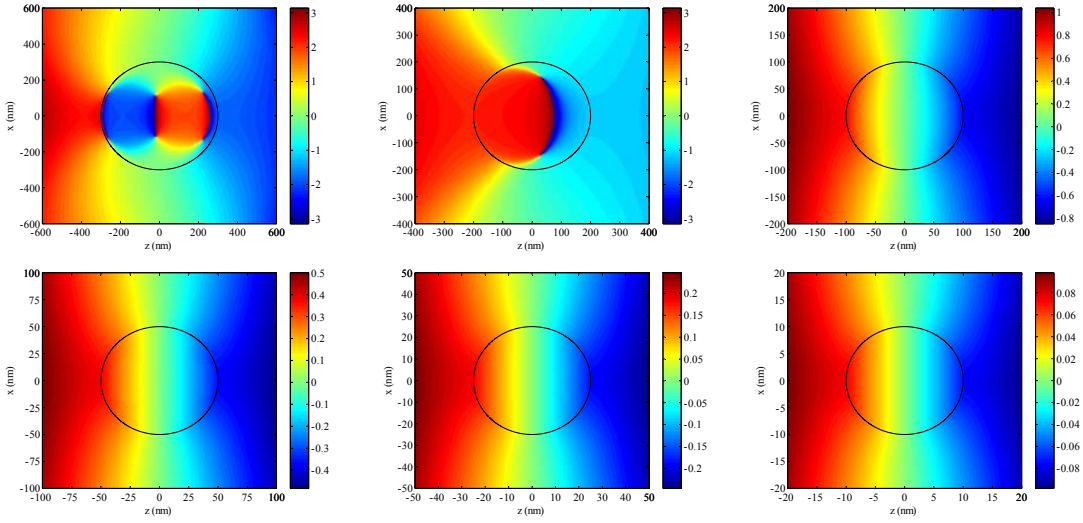

Figure 4.8: Phase of magnetic field in y direction (H_y) for SiNWs with diameters of (from top to right) 600 nm, 400 nm, 200 nm, 100 nm, 50 nm and 20 nm, at wavelength of 1550 nm [4].

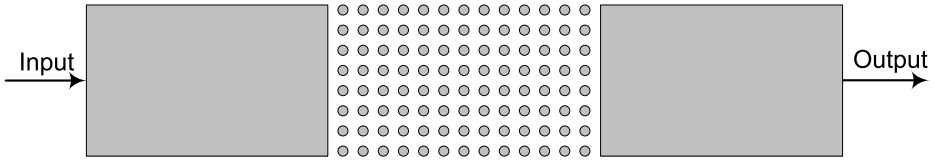

Figure 4.9: Schematic diagram of a FP cavity using arrays of SiNWs sandwitched between two bulk silicon waveguides [4].

4.2.2 Finite Difference Time Domain (FDTD) Analysis of SNOW

In order to verify that the array of nanowires can guide optical signal, the structure is simulated using FDTD method. In the first simulation, arrays of nanowires are located between two bulk-silicon waveguides. The top view of the simulated structure is shown in Fig. 4.9. The input waveguide is excited by a Continuous Wave (CW) power at wavelength of 1550 nm. Eventually, the optical signal is coupled to an output silicon waveguide after passing through the SNOW region. The width of the all waveguides is 260 nm, in order to keep the silicon waveguide single mode. The length of the bulk Si waveguides is 1 μm and the length of SNOW part is 6 μm. The diameter of the SiNWs in the SNOW region is 20 nm and the separation between the SiNWs is 30 nm. Figure 4.10 shows the mode propagation when the electric field is polarized along the length of the SiNWs. Such a polarization is equivalent to the quasi-TM mode for a conventional ridge waveguide in the same orientation. As can be seen from the figure, at the intersection of the silicon waveguide and SiNWs, radiation of optical field occurs. This is expected as there is a modal change between the two waveguides. However, once coupled, the array of SiNWs is guiding the optical power. Further, a Fabry Perot (FP) cavity effect is seen in the SNOW region because of different effective indices in the two regions creating reflections at the boundary and increasing the intensity of the wave within SNOW region over multiple passes in the FDTD.

A very simple approximation can be used to calculate an effective index for the nanowire region. The approximation is modified from [106] which calculated the effective index for a multiple quantum well region. For the approximation it is assumed that the electric field is constant in a single cell consisting of the SiNW along with the surrounding medium. For the electric field polarized along the length of the nanowires, the TE mode calculation for quantum wells is used as the electric field is polarized along the unconfined axis of the quantum well, this being the same case for SiNW. The resulting approximation for the effective-index is shown in the equation

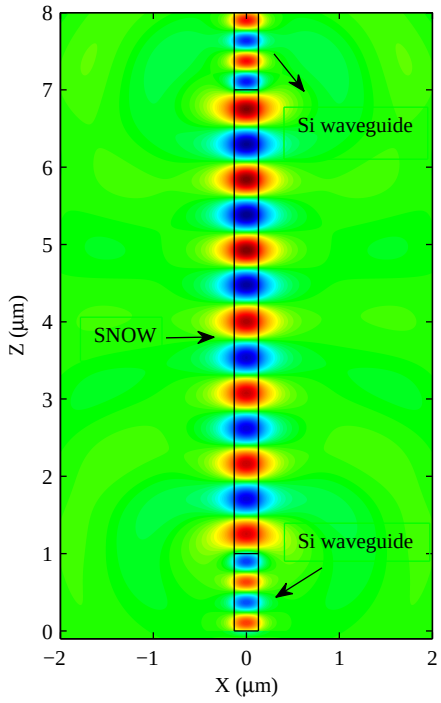

Figure 4.10: Longitudinal electric field of arrays of SiNWs with diameter of 20 nm and pitch of 30 nm when they are located between two bulk silicon waveguides with the same width, at wavelength of 1550 nm. The electric field is polarized along the length of the nanowires [4].

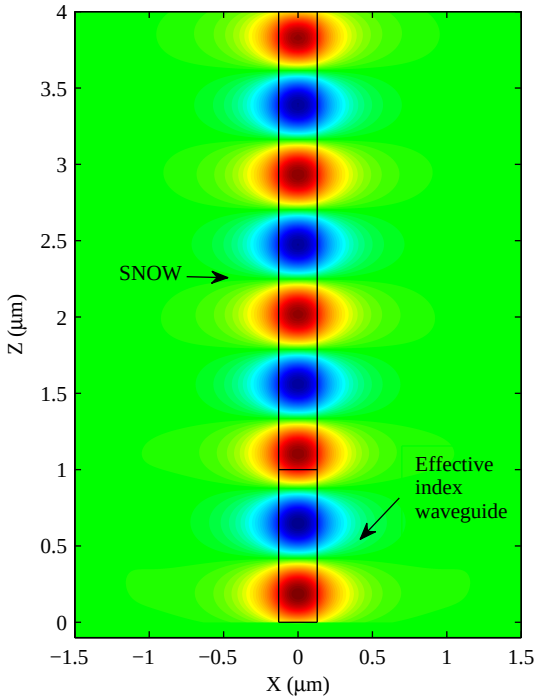

Figure 4.11: Longitudinal electric field of arrays of SiNWs with diameter of 20 nm and pitch of 30 nm when they are butt joint to a waveguide with an index equal to the effective index of the nanowire region, at wavelength of 1550 nm.The electric field is polarized along the length of the nanowires [4].

below:

$$n_{rep} = \sqrt{\frac{n_{Si}^2 \times A_{Si} + n_{surround}^2 \times A_{surround}}{A_{Si} + A_{surround}}} \tag{4.13}$$

where n_{Si} and $n_{surround}$ are refractive-index of silicon and surrounding medium respectively, and n_{rep} is the refractive-index calculated by average index method. Also, A_{Si} and $A_{surround}$ represent the area of silicon and surrounding medium, respectively. For the current analysis, the surrounding medium is air but it can be replaced by another dielectric. Figure 4.11 shows a FDTD simulation when the nanowire region is excited by an optical waveguide with an index equal to the effective index of the nanowire region calculated above. The two waveguides are of the same width. From the figure it is easily observed that negligible reflection and radiation are seen at the butt joint of the two waveguides, showing that the optical mode shape and propaga-

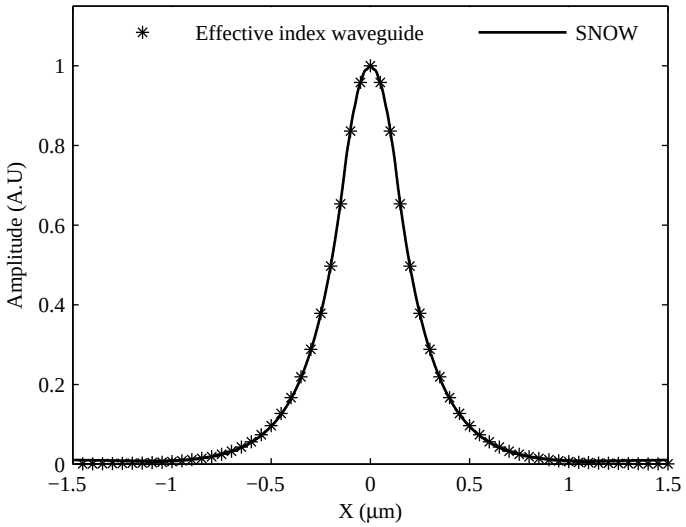

Figure 4.12: Optical mode shape of optical waveguide and SNOW region [4].

tion constants do not change and that the approximation does work well. To further evaluate this, the mode shape of optical waveguide and SNOW region (calculated after transmission of optical wave through SNOW), are also plotted in Fig. 4.12. A very good overlap using the proposed effective-index method and for the optical mode after propagation through SNOW region observed in Fig. 4.12, further confirming the accuracy of the effective-index calculation. Similar overlap is also seen in the vertical direction for the optical mode. This approximation can play an important role in design of optical structures using SNOW as it can allow for treating the structure only as an averaged bulk waveguide for design and optimization. Therefore, conventional integrated optics formulation can be used. The initial designs and simulations can be done using beam propagation and analytical methods before final validation with FDTD resulting in a significant time saving.

Using the effective-index waveguide as the input waveguide, and measuring optical power at different regions for the SNOW waveguide, we analyzed the optical loss using the cut-back method by calculating transmitted optical power at different lengths in the SNOW region. The input to the SNOW region is the optical mode for the dielectric waveguide using effective index approximation. While the cut-back method is mainly used experimentally, it allowed us to calculate the propagation loss of the SNOW region and coupling efficiency between the two waveguides in a single simulation. Further, by measuring multiple lengths, we could check the accuracy of

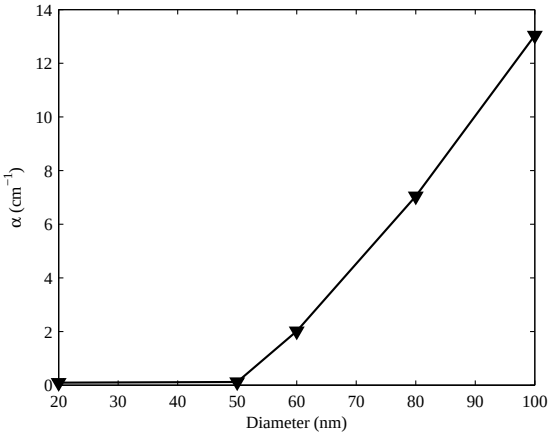

Figure 4.13: Variation of loss versus diameter of SiNWs when diameter/pitch ratio is kept unchanged, 1 : 1.5 [4].

the analysis especially for the structures with low propagation loss. We have analyzed the dependence of loss for the two important parameters of SNOW region, i.e. the diameter of the nanowires and the pitch between the nanowires. Figure 4.13 shows how the loss changes as the diameter of the nanowire is increased. For this simulation, the number of SiNWs in an array and the ratio of the diameter to the pitch (1 : 1.5) were kept constant. It is observed that for the nanowire diameters less than 50 nm, the loss is lower than 0.12 cm^{-1}, but starts to increase appreciably as the diameter increases to 100 nm. The increased loss is due to scattering of light by the nanowires. This result mirrors the understanding we got in Fig. 4.4 and 4.5 from looking at light scattering from a single nanowire. It needs to be mentioned that the loss calculation for diameters less than 50 nm is limited by the grid size. For these calculations, a grid size of 2 nm is used in all dimensions limited by the memory of the computer. Hence, the values provided here provide an upper limit on the propagation loss.

Figure 4.14 shows the loss as the spacing between the nanowires is increased. The diameter of the nanowires is 50 nm. From Fig. 4.4 and 4.5, it is clear that the results for smaller diameters will be better. It is seen that the loss increases once the separation increases beyond 150 nm. Since the SNOW waveguide is acting like an effective index medium, the electric field within a unit cell should be nearly constant [100]. As the pitch is increased, the assumption that the electric field within a unit cell containing the SiNW is constant is no longer valid, thereby resulting in increased scattering loss. Diameter of 150 nm corresponds to approximately to one tenth of the free-space wavelength. This suggests that beside the diameter, there is

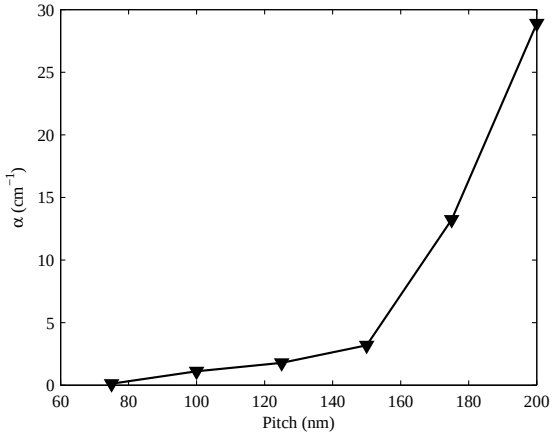

Figure 4.14: Variation of loss versus pitch of SiNWs in the array [4].

an additional parameter (pitch) which can be altered to change the effective index of the SNOW region thereby optimizing the mode shape and confinement in the SiNW region while not increasing the loss appreciably.

The different calculated optical parameters for the structures are summarized in Table I. Overlap integral between the mode after propagation through SNOW region and the optical mode of the effective-index waveguide is shown in the table. High value of the overlap integral ($> 99\%$) for different pitches suggests the efficacy of the effective-index approximation for the SNOW region in a wide range of pitches. The optical confinement factor for different waveguide structures is also summarized in the table. The confinement factor is the ratio of the power confined to the SiNWs in the SNOW region compared to the input power. The table also summarizes the optical confinement factor within the SiNWs for the SNOW. It is seen that the optical confinement within the SiNWs has increased appreciably in the SNOW structures compared to a single nanowire waveguide of the same diameter. For example for the diameter of 50 nm and diameter:pitch ratio of $1 : 1.5$, an optical confinement factor of 33% is achieved. Compared to this, for a single nanowire of 50 nm surrounded by air, the confinement factor is $\sim 0.1\%$. Furthermore, even if the diameter is reduced, similar confinement factors can be achieved if the diameter:pitch ratio is kept constant. Thus, the SNOW structure allows for increased optical confinement of optical mode while the increased optical interactions of SiNWs can also be utilized in these structures. Moreover, from the effective-index approximation it is clear that the confinement factor within the SiNWs is mainly dependent on the diameter:pitch ratio. Consequently, if for some applications small nanowire in diameter is required a

Table I. Different calculated optical mode parameters for the SNOW with diameter of 50 nm.

Structure #	1	2	3	4	5	6
Pitch (nm)	75	100	125	150	175	200
Overlap integral *	0.9996	0.9987	0.9987	0.9987	0.9981	0.9939
Optical confinement factor within SiNWs	32.93%	18.47%	11.80%	8.19%	6.01%	4.38%
Optical confinement factor of SNOW	94.36%	94.11%	93.96%	93.85%	93.77%	89.41%

*Overlap integral between modes in weight index waveguide and SNOW region.

reasonable optical confinement can be achieved by adjusting the pitch to increase the overall performance of the device while taking the advantages of nanowire properties. All the analysis has been done for SiNWs with high vertical confinement, since the goal of the work is to propose a waveguide structure where confinement is increased in the SiNWs. By decreasing the SiNWs length (typically below 300 nm), the confinement is reduced in the vertical direction and the mode will become less quasi-TM like (i.e. the H_z component will increase) which could result in higher radiation loss due to polarization coupling which may occur.

Furthermore, we are interested to see whether the SNOW region will guide light if the nanowires are arranged randomly. We did a simulation where the nanowire diameter was 20 nm and the average separation between the nanowires was 30 nm. We assumed up to 100 % change in the origin of SiNWs in all planar directions in a random distribution with equal probability over the range of the pitch. Figure 4.15 shows longitudinal mode propagation in this case. The results are similar to what was achieved when the SiNWs are located in an ordered fashion showing that guidance still happens. It is reiterated here that in a PBG structure with disordered scattering points no light will be guided [107]. The optical loss in this case was 2.91 cm^{-1} as compared to 0.094 cm^{-1} for ordered nanowires of same dimensions. Again the loss measurement is the upperbound as the grid discretization is more critical in a random arrangement. While the loss has increased, it is still comparable to PBGs and is not a hindrance in many applications especially optical sensing. Unordered SNOW region will allow to use low cost fabrication schemes including maskless etching like in black silicon [103] and Vapor Liquid Solid (VLS) grown nanowires [19] provided the nanowires are vertical. However, if the SiNWs are not vertical in these processes, there will be an excess loss due to depolarization of the light with respect to the nanowire axis.

We also simulated the optical mode propagation for the SNOW structure when

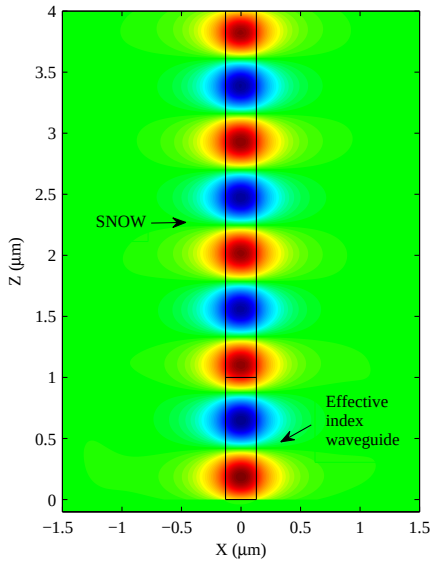

Figure 4.15: Longitudinal electric field of arrays of SiNWs when they are randomly located and butt joint to a waveguide with an index equal to the effective index of the nanowire region, at wavelength of 1550 nm. The boundary of the SNOW region and effective index waveguide has been highlighted [4].

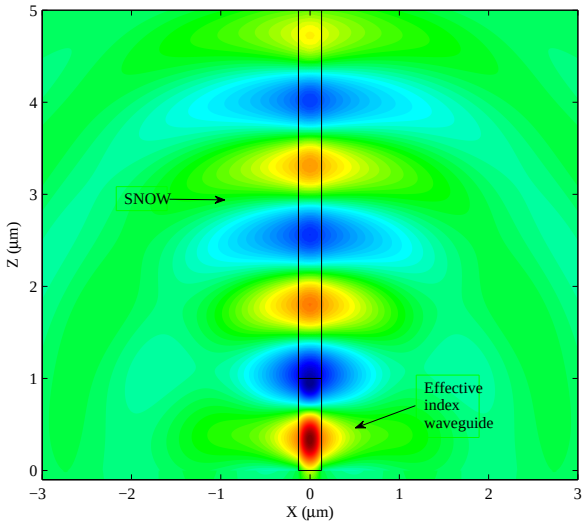

Figure 4.16: Longitudinal electric field of arrays of SiNWs when they are butt joint to a waveguide with an index equal to the effective index of the nanowire region, at wavelength of 1550 nm and magnetic field polarized along the length of the nanowires [4].

the magnetic field is polarized along the length of the nanowires. This polarization corresponds to the quasi-TE mode for the conventional ridge waveguides. Figure 4.16 shows the mode propagation through the SNOW region for SiNW diameter of 20 nm. High radiation loss is observed in this case with a loss of $\sim 400\ cm^{-1}$. This mirrors the understanding from Fig. 4.7 and 4.8 which suggest that for this polarization, the optical field is going to suffer scattering. This suggests the SNOW can be used to fabricate ultra short polarization filter within a photonic integrated circuit. In the next section, performance of SNOW in bend configuration will be discussed.

4.3 Bend-Waveguides on SNOW Structures

Since the SNOW structures consist of small inclusions; there is a concern of increased radiation through the bend due to scattering of light from the nanowires. In this section, we show that bend waveguides with small radii can be achieved and the SNOW region acts like an effective-index medium even over a bend. We analyze the radiation loss through the bend for varying radii of the bend, and pitch between

the nanowires and compare the loss with a conventional bulk waveguide with core equal to the effective-index for the SNOW. Interestingly, the bend waveguide can be optimized for loss by arranging the nanowires appropriately. Furthermore, the effect of wavelength and sidewall roughness on propagation loss are also studied. Bend waveguides are important building block for implementations of various photonic components such as ring resonators, power splitters, array waveguide gratings, and Mach-Zehnders. Low loss bends in SNOW allow for these structures to be used in integrated optics.

4.3.1 Device description

Figure 4.17 shows the top-view schematic of the SNOW structure with a bend. Vertical SiNWs are etched into a SOI wafer. Since we are interested in high optical confinement, we have considered the length of the SiNWs to be larger than 500 nm providing more than 95 % optical confinement in the vertical direction. Cylindrical co-ordinates are used to define the bend in the structure. The parameters defining the structure include the width of the SNOW region (W), the diameter of the nanowires (D), the pitch in the radial direction (P_ρ) and the pitch in the angular direction (P_ϕ). For this section, we consider a nanowire diameter of 50 nm for all the structures. The width of the SNOW region is 0.65 μm for $P_\rho = 75$ nm, same as what were considered in previous section for straight waveguides. The wavelength of operation is 1550 nm and the electric field is polarized along the length of the nanowires, polarization for which we have previously shown guidance through straight waveguides. This corresponds to quasi-TM mode for conventional waveguides. The bends are analyzed using FDTD method with a grid size of 2 nm for SNOW structure and 10 nm when it is substituted by an effective-index medium. Between the grid points, the refractive index is linearized to decrease the effect of grid size. The grid size was varied by a factor of 2 to see the numerical accuracy of the results and beyond 2 nm, there was minimal change in loss calculation. CW excitation was used to analyze the structures. In the following, the performance of device is analyzed numerically.

4.3.2 Simulation results and discussion

Bend loss

For the first simulations, we considered that P_ρ and P_ϕ are equal to 75 nm. This pitch provided the lowest loss in straight waveguides. The effective-index of the SNOW

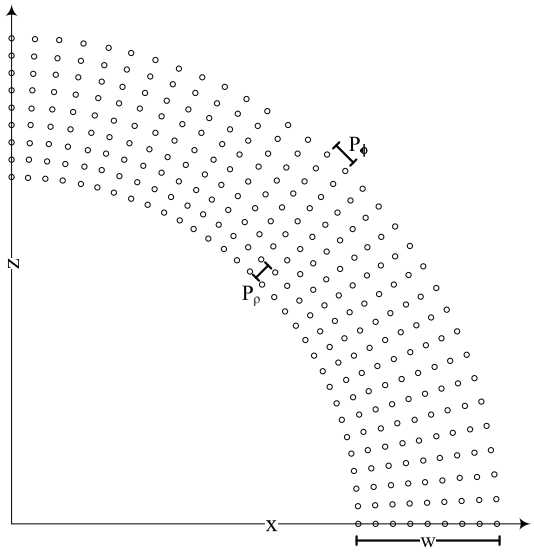

Figure 4.17: Top-view schematic diagram of bend waveguide with SNOW [5].

region is approximately 2.2 that still provides a high-index contrast waveguide and thus, small bend radius should be possible with low loss. Figure 4.18 shows the lateral distribution of electric field in the bend SNOW for a radius of 5 μm. The excitation is a CW source located at the beginning of the right side of the 180° bend SNOW and the light propagates counter-clockwise. The figure demonstrates that the SNOW structures can bend the optical wave. Radiation loss was calculated by monitoring the decay of power along the bend and is plotted in Fig. 4.19 for varying radius of the bend for a 360° turn. For a radius of 5 μm, the radiation loss per turn is less than 5×10^{-4} dB and increases to 0.05 dB for a bend radius of 2 μm. Also plotted in the same figure is the radiation loss if the SNOW region was substituted by an effective-index waveguide. The effective-index is calculated by a weighted average of the silicon permittivity and the surrounding medium (air); the weights being equal to the area of the individual materials [4]. As seen, a good agreement between SNOW and effective-index waveguide is achieved. This shows that the SiNW inclusions do not create much scattering even over a bend and the losses mainly come from the radiation through the bend itself.

We also analyzed the structures for varying P_ϕ . Figure 4.20 shows the loss for a bend radius of 2 μm when P_ϕ is varied and P_ρ is kept constant at 75 nm. The loss is low till a value for P_ϕ of 125 nm but increases appreciably after that and is equal to 0.56 dB per 360° turn for P_ϕ of 150 nm. It is to be noted that the effective-index

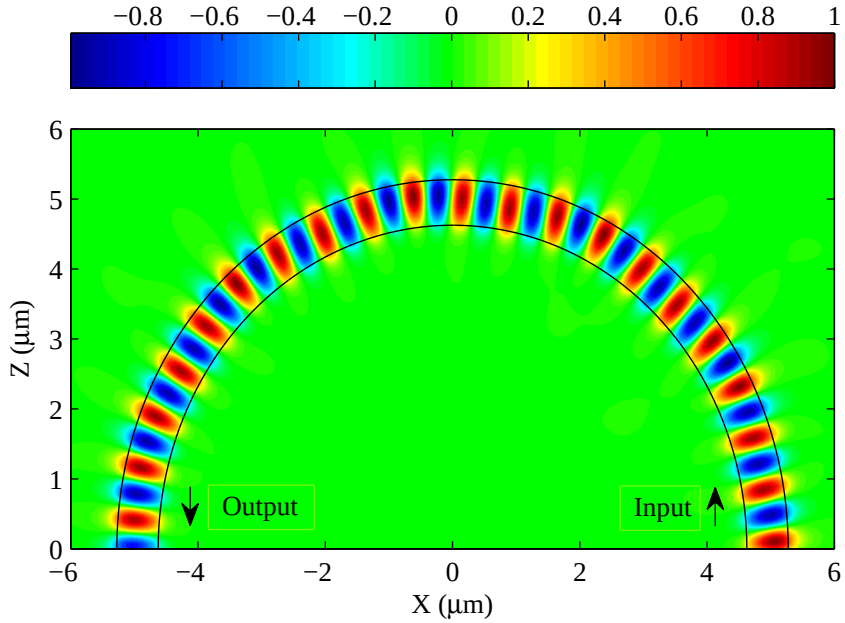

Figure 4.18: Lateral electric field distribution for a bend SNOW with a radius of 5 μm, at wavelength of 1550 nm. SiNWs have diameter of 50 nm and pitch of 75 nm for both P_ρ and P_ϕ. The electric field is polarized along the length of the nanowires [5].

reduces as the value of P_ϕ increases. For a value of P_ϕ of 150 nm, the effective-index reduces to 1.7 instead of 2.2. Also plotted is the loss for the bend if an effective-index bulk waveguide is used, where the effective-index is calculated for the corresponding pitch. The loss increases in the same fashion suggesting that the increased loss is due to decreased waveguide confinement and not due to scattering from individual SiNWs as they are placed further apart.

The loss further increases if both P_ρ and P_ϕ are changed simultaneously because of reduced confinement. As an example for $P_\phi = P_\rho = 100$ nm, the loss increases to 1.81 dB for a bend radius of 2 μm. Since SNOW structures do not need the SiNWs to be arranged in an ordered fashion and since the inclusions work as an effective-index waveguide, one can think of designing the bend for reduced loss by improved waveguide design. The idea is to have the increased effective-index in the inner part of the bend while having a reduced effective-index on the outer part. This should result in pushing the optical wave towards the inner part of the waveguide

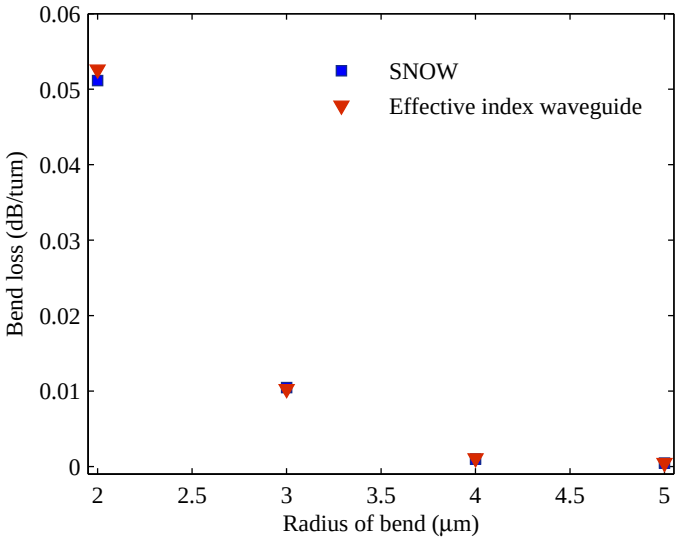

Figure 4.19: Loss for various radii of bend SNOWs over a 360° turn [5].

counteracting the effect of the bend which pushes the optical wave to the outside. The change of the effective-index can be achieved by changing either of P_ρ or P_ϕ over the waveguide width. We calculated the loss for a bend radius of 2 μm when the P_ϕ changed from 80 nm to 120 nm over the waveguide width in a linear fashion and P_ρ was kept constant at 100 nm. The average of P_ϕ was 100 nm. The radiation loss was 1.41 dB per 360° turn compared to a value of 1.81 dB if the both pitches were kept constant at 100 nm.

Effect of operational wavelength

Figure 4.21 shows the bend loss versus wavelength for a bend radius of 2 μm. Both pitch sizes are 75 nm. By increasing the wavelength, optical confinement decreases because of reduction in the normalized frequency and reduction in refractive index of silicon. Consequently, the bend loss increases due to reduced optical confinement. However the loss is still low over a wide wavelength region spanning 100 nm. This also clearly shows the SNOW bends are not working like PBG structures.

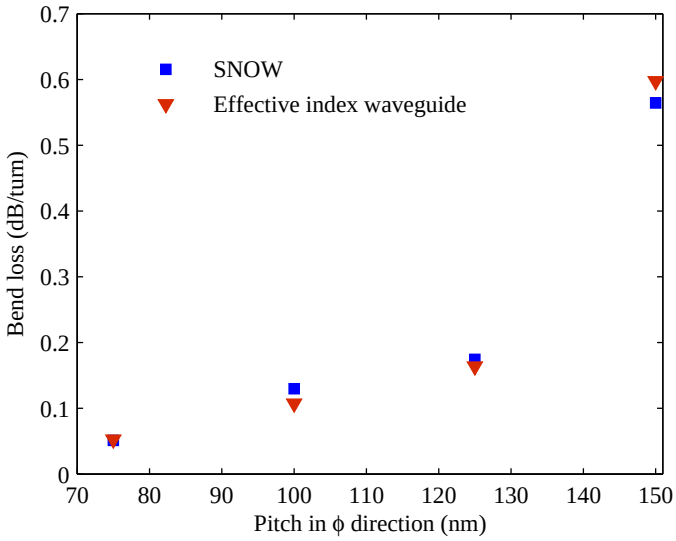

Figure 4.20: Loss for various pitches in ϕ direction of bend SNOWs over a 360° turn. P_ρ is kept constant at 75 nm. The loss for effective-index waveguide is also plotted showing that the loss mainly comes from reduced waveguide confinement [5].

4.3.3 Effect of sidewall roughness

A main area of concern for the SNOW devices is the scattering of the light due to sidewall roughness. Sidewall roughness in photonics band gap structure is a major source of optical loss [108]. Similarly, in silicon photonics devices, owing to the high-index contrast between a silicon waveguide and its surrounding medium, sidewall roughness results in significant scattering losses [8]. For example it has been shown that for a 200 nm wide SOI waveguide, the loss due to roughness of 2 nm is 2.6 dB/cm [109]. Besides, the propagation loss may change strongly from one waveguide to another on the same wafer. Such variations are inevitable due to the manufacturing process fluctuations. Therefore, this is important to consider these variations in the designs.

We considered the effect of sidewall roughness on performance of SNOW. We assumed different amounts of perturbation from 2 nm to 7 nm on sidewall of each SiNW. Effect of sidewall roughness can be simulated by considering a systematic perturbation of the index profile. We did this by drawing the structure in a grid equal to value of the perturbation in a mask design software. The resulting structure is then converted to an index profile. To reiterate, the index is linearized between

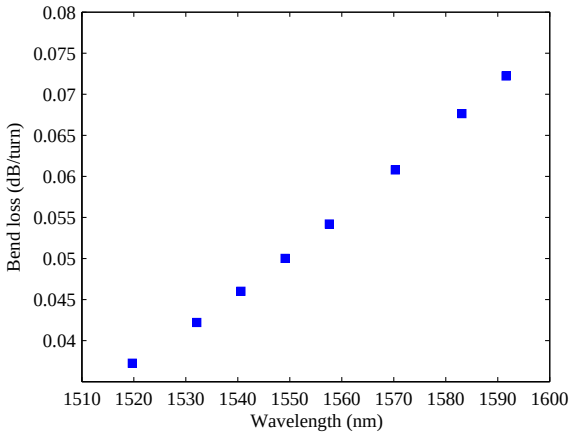

Figure 4.21: Loss for various wavelengths for a SNOW with bend radius of 2 μm [5].

the grids. To visualize it, the profile index of a SiNW is shown in Fig. 4.22 for

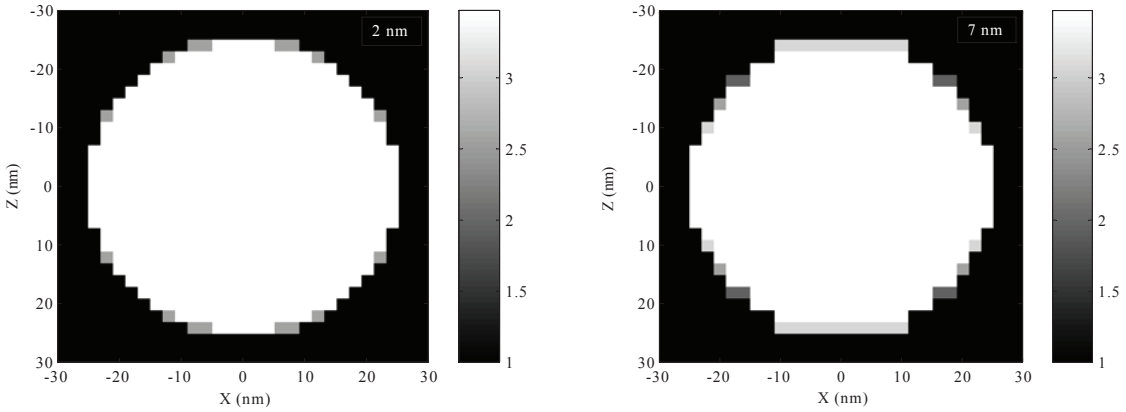

Figure 4.22: Profile index of a SiNW by considering a sidewall roughness of 2 nm (left) and 7 nm (right) [5].

perturbations of 2, and 7 nm.

Figure 4.23 shows the calculated bending loss for various sidewall roughness. Bending loss for no sidewall roughness is also provided for comparison purpose. The excess loss due to sidewall roughness is quite small as opposed to what was achieved for photonics crystal showing another advantageous of SNOW. Further this loss is lower than that for side wall roughness of 2 nm in SOI waveguide. We believe the loss is low because each individual nanowire in the array has very low optical con-

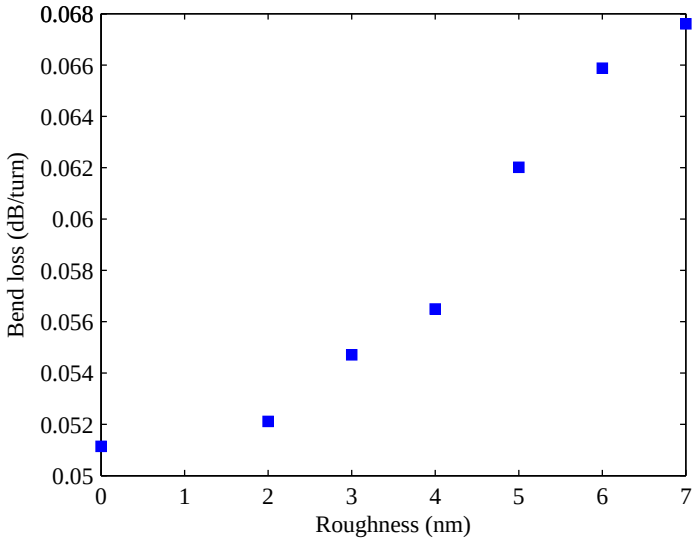

Figure 4.23: Radiation loss for a bend radius of 2 μm for various sidewall roughness, the reference point of zero is provided for comparison [5].

finement and a small perturbation in each individual nanowire does not change the phase. Further, since SNOW is acting as an average waveguide, the roughness on individual inclusions get averaged out over many. A reduction in roughness-induced propagation loss due to decreasing optical confinement has been previously shown to occur as the waveguide width is reduced below 260 nm for SOI waveguides [109]. In next section a design of bio-chemical sensor based on SNOW structure will be presented.

4.4 Optical Bio-Chemical Sensors on SNOW Ring Resonators

Optical biosensors have attracted considerable attention in the last decade because of their promise to contribute to major advances in medical diagnosis, environmental monitoring, drug development, quality control, and homeland security [110]. Compared to electrical transducers, optical sensors provide significant advantages because of their small size, immunity to electromagnetic interference, ease of multiplexing using wavelength encoding, and capability of remote sensing [111]. Optical sensors can be broadly characterized in two categories: fluorescence based detectors and

label-free detectors. In fluorescence based detectors, the target molecules are labeled with fluorescent tags such as dyes and the fluorescence is detected in presence of the targeted molecule. This allows for extremely sensitive detection down to a single molecule [112]. However, the process is laborious and may also affect the function of the biomolecules. Further, precise quantitative measurements are difficult as the number of flourophores attached to the targeted molecules cannot be controlled [113]. In contrast, in label-free detection the targeted molecules are detected in their natural form. The targeted molecules are surface attached to the optical sensor using probe molecules and the attachment is detected by measuring the change in optical properties for the sensor. Sensors based on SOI photonic wire waveguides have attracted considerable attention because of compatibility with CMOS fabrication and possibility of integrating detection and decision on the same chip leading to *laboratories on a chip* [111]. Further, guided-wave sensors allow for integration of multiple sensors on a single chip. As such, different sensors based on directional couplers [114], Mach-Zehnder interferometers [115], Bragg grating based Fabry-Perot resonators [116], microdisks [117], microtoroids [118], photonics crystal cavities [119], microring resonators [120], and slot waveguides [121] have been demonstrated. In these sensors, the targeted molecule is probed by light guided through a solid medium using the evanescent field. The lower refractive-index surrounding medium (typically water with refractive-index ~ 1.3253) is displaced by higher refractive-index organic molecules ($n \sim \ 1.45 - 1.6$) changing the effective-index of the propagating mode resulting in a spectral shift of the resonant cavity which can be measured directly. Mach-Zehnder interferometers, Fabry-Perot resonators, microdisks, photonic crystal cavities, and ring resonators have been demonstrated using silicon photonics. Mach-Zehnder interferometers suffer from low Q and the requirement of large interaction length to increase the sensitivity. Bragg-reflectors for Fabry-Perot resonators are difficult to fabricate in high-index contrast materials resulting in high insertion losses. Photonics crystal cavities are also difficult to produce with low propagation losses and it is difficult to couple light in and out of these waveguides reproducibly. Microdisks have higher whispering gallery modes which can overlay on the fundamental characteristics making detection difficult. As such, ring resonators offer most attractive solution as they provide low insertion loss, single mode cavities, and small form factors. Ring resonators offer a compelling solution as multiplexing different sensors on a single chip using wavelength is possible by simply changing the diameter of the ring in the resonator. Biochemical sensors based on SOI photonic waveguides have been studied extensively. In [120], a 70 $nm/refractive-index\ unit(RIU)$ sensitivity was achieved for bulk changes of refractive-index and a 625 pm shift of wavelength was achieved for label-free sensing of proteins. The sensitivity can be further increased by

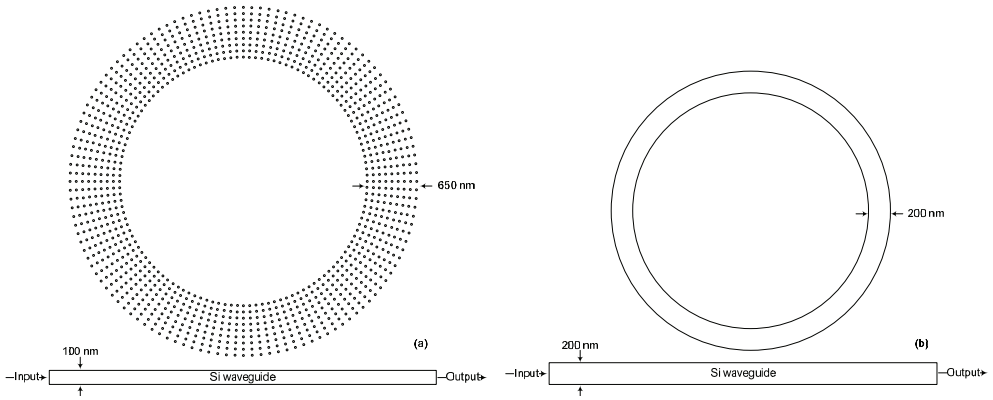

Figure 4.24: Schematic of (a) the proposed ring resonator with SNOW, (b) a conventional Si ring resonator [6].

using a slot-waveguide which is an optical waveguide guiding light in a subwavelength-scale low refractive-index region sandwiched between two ridges of high index region material. This enhances the transverse electric field in the slot thereby increasing the interaction of the optical field with the targeted molecules. An increased sensitivity of 298 nm/RIU was achieved with a foot-print of 13 $\mu m \times 10$ μm [121]. However, the problem with slot waveguides is the difficulty with introduction of fluids within the slot region. Further since the slot waveguide works in the quasi-TE mode, it is lower modal-index waveguide compared to SOI waveguides.

In this section, we propose and analyze novel ring resonator based bio-chemical sensors on SNOW and show that the sensitivity of the sensors can be increased by an order of magnitude as compared to SOI based ring resonators. The advantage of SNOW is apparent from the fact that it is a hollow core waveguide and thus it is possible to introduce the bio-chemical agents in the region of highest optical field intensity. As shown in previous section, even over a bend, the effective-index approximation works well. This allows for designing and building of ring resonators on the SNOW for biochemical sensing applications.

4.4.1 Proposed Sensor Structure

The proposed structure is shown in Fig. 4.24. A SOI waveguide is used as a bus waveguide feeding into a ring consisting of SNOW. Use of SOI waveguides allows for conventional input and output optical coupling into the structure resulting in low insertion losses. The bus waveguide has a width of 100 nm and has the same

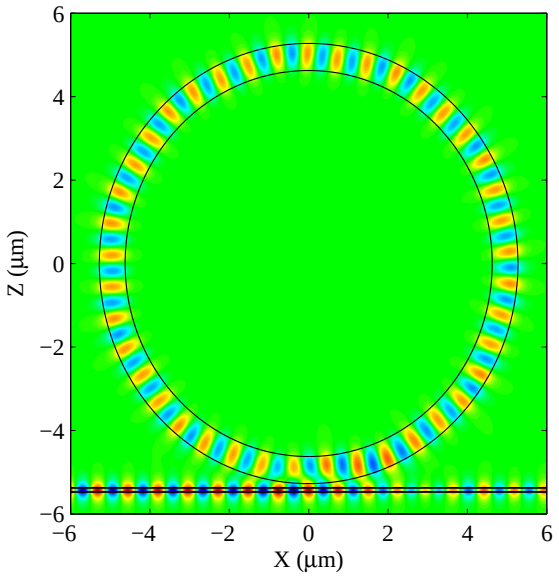

Figure 4.25: Lateral cut of the FDTD propagation of electric field through the SNOW ring resonator [6].

height (700 nm) as the SNOW ring. At this width, the bus waveguide is purely single mode. Separation between the waveguides is adjusted to be 100 nm between the end of the bus waveguide and the first nanowire in the SNOW to achieve critical coupling condition for the ring resonator.

Figure 4.25 shows the lateral cut of the FDTD propagation of the electric field through the ring resonator at a wavelength of 1550 nm (not the resonance wavelength) over a few cycles within the ring. One can clearly see that the SNOW ring is guiding the electric field with very little radiation happening in the structure.

Figure 4.26 shows the lateral cut of the electric field through the SNOW structure for the parameters defined in Table I. The lateral cuts for a straight SNOW and over a bend are shown. Lateral cut for the 200 nm wide straight SOI waveguides is also shown. Within the effective-index waveguide, the confinement factor for the SNOW is 94 % resulting in the low bend losses as shown previous section. The confinement factor for the optical mode within silicon in the SNOW region is only 32 % whereas for a 200 nm SOI waveguide, it is 76 %. The optical mode is better guided in the SNOW region as compared to the 200 nm SOI waveguide, and the modal power in the surrounding region is larger in the SNOW as compared to the 200 nm SOI. Thus,

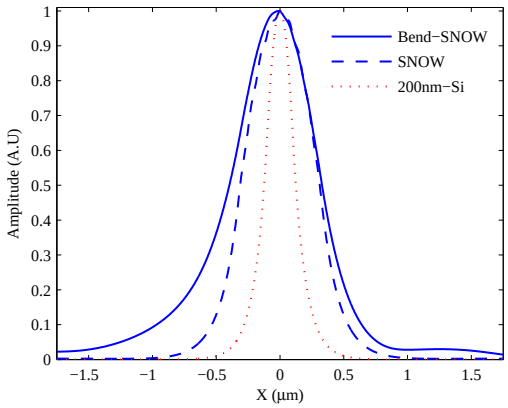

Figure 4.26: Lateral electric field cuts for the SNOW with width of 650 nm for both bend, with a radius of 5 μm, and straight structures and the silicon waveguide with width of 200 nm at wavelength of 1550 nm [6].

Table I. Device parameters for simulated SNOW and standard SOI ring resonators.

Device Parameters	SNOW Ring Resonator	SOI Ring Resonator
Width	*650 nm*	*200 nm*
Ring Radius	*5 μm*	*5 μm*
Height	*700 nm*	*300 nm*
Nanowire dimension	*50 nm diameter, 75 nm pitch, 9 row*	*N.A.*

it should be possible to increase the sensitivity while still achieving compact devices.

4.4.2 Sensor Characteristics for Bulk Refractive-Index Change

We first calculated the response of sensor for bulk change in the refractive-index of the surrounding medium. The SNOW structure is compared with a SOI waveguide ring resonator where the width of the SOI waveguide is 200 nm, similar to [120]. The geometric parameters for the two compared devices are shown in Table I. For the first set of simulations, the refractive-index of the surrounding medium was changed and the effective-index of the guided optical mode through SNOW was calculated. Figure 4.27 shows the change of effective-index of the optical mode as a percentage with respect to the value of effective-index as the surrounding refractive-index is changed from 1.0 to 1.6 for the SNOW and the 200 nm SOI waveguide at a wavelength of

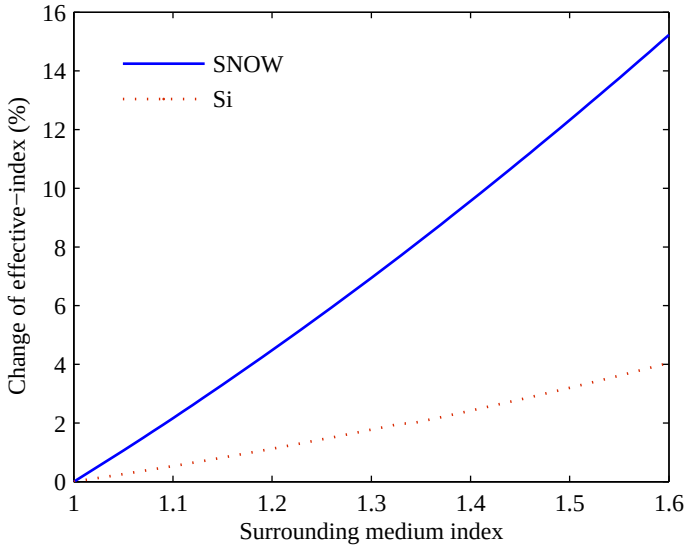

Figure 4.27: Change of effective-index as a percentage for SOI and SNOW ring resonator as the surrounding index is changed [6].

1550 nm. For the SNOW, the effective-index changes by a factor of approximately 4 larger as compared to a 200 nm SOI waveguide for the same change in surrounding refractive-index. In a ring resonator the change of the resonance wavelength is approximately given by [121]:

$$\Delta\lambda = \frac{\Delta n_{eff}\lambda}{n_g} \tag{4.14}$$

where Δn_{eff} is the change of the effective-index due to the change of the refractive-index of the surrounding medium, λ is the initial resonance wavelength and n_g is the group index. This suggests that an improvement in sensitivity of 4 is expected if one uses a SNOW ring resonator as compared to a 200 nm wide SOI waveguide resonator.

Figure 4.28 shows the response of the ring resonators for SNOW and SOI when the surrounding index is changed from 1.0 to 1.05. A wavelength shift of 12.2 nm is achieved for the SNOW ring resonator resulting in a sensitivity of 243 nm/RIU. For the 200 nm SOI waveguide, the wavelength shift for the same refractive-index change is 3.14 nm resulting in a sensitivity of 63 nm/RIU. This compares well with the experimental value of 70 nm/RIU for a slightly higher bulk refractive-index [120]. An

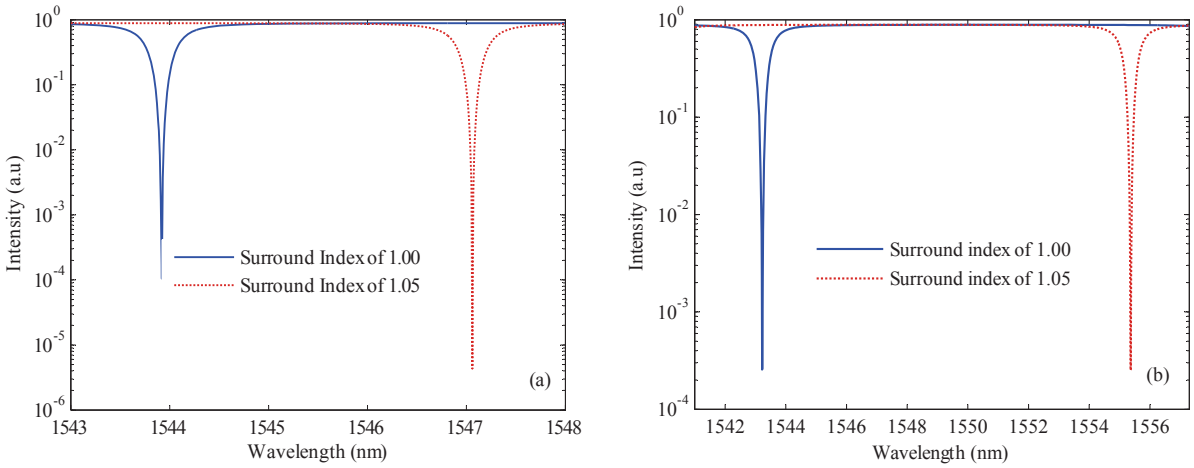

Figure 4.28: (a) Shift of resonance wavelength for SOI ring resonator when the surrounding index is changed from 1 to 1.05. (b) Shift of resonance wavelength for SNOW ring resonator when the surrounding index is changed from 1 to 1.05 [6].

improvement by a factor of 3.9 is seen in the sensitivity for the SNOW ring resonator compared to the 200 nm wide SOI waveguide for bulk change of refractive-index.

We also studied the effect on sensitivity as the width of the SNOW region is changed. The ring resonator coupling was adjusted individually to achieve critical coupling. Figure 4.29 shows the change of sensitivity for the SNOW ring resonator as the width of the effective waveguide is varied. The diameter and pitch for the SiNWs are kept the same. An increase of sensitivity is observed when the waveguide width is decreased, reaching a value of 335 nm/RIU for a width of 300 nm. The surrounding index is again changed from 1 to 1.05. An improvement by a factor of 5.3 is observed as compared to the SOI waveguide. The behavior exhibited by the SNOW ring resonator is similar to that of the SOI ring resonators as the width is decreased. This is because of the increased evanescent field as the width is decreased.

4.4.3 Sensor Characteristics for Surface Attachments

In optical sensors, surface sensing plays an important role for a wide range of biochemical applications including DNA hybridization, antigen-antibody reactions, protein attachments etc. A layer of receptor molecules is surface attached to optical sensor and selective attachment is done for the targeted molecule. Since the refractive-index of the molecules is different from the surrounding medium which is typically water

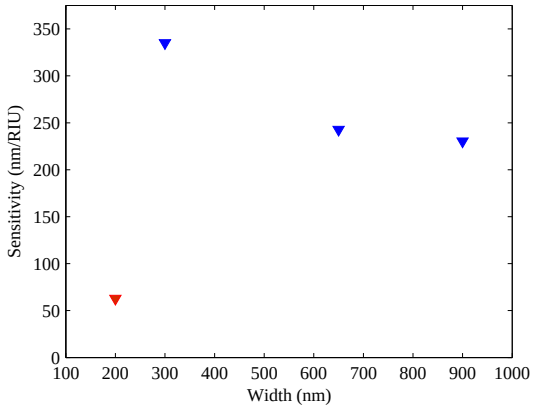

Figure 4.29: Change of sensitivity as width of SNOW is changed. Sensitivity for a 200 nm SOI is also shown [6].

based, a change of index happens at the surface of the sensor which is measured for detecting the presence of the molecule. The SNOW ring resonator was simulated for surface attachment of the molecules. A molecule layer with the test thickness was assumed to be attached the surface of the SiNWs. Water was considered as the surrounding medium with a refractive-index of 1.325 at a wavelength of 1550 nm [122]. The refractive-index of the molecule attached is considered to be 1.6, similar to 3-aminopropyltriethoxysilane (APTES) which have been measured previously by Saini *et al.* [123] and controllably attached different thickness on the surface. Structure parameters were summarized in Table I and compared. Figure 4.30-(b) shows the response of the SNOW sensor when 0.1 nm and 1 nm of the molecule layers are uniformly attached to the surface of the nanowires. Wavelength shift of 0.35 nm and 3.1 nm and are achieved with a 0.1 nm and 1 nm attachment of the molecule, respectively. For these thin layers, the surface attachment increases linearly with the thickness of the molecule layer. Figure 4.30-(a) shows the response if the 200 nm SOI waveguide was used for the detection. For the SOI waveguides, surface attachment was assumed over all the exposed surfaces of silicon including the sides and the top of the waveguide. Only a 1 nm layer attachment was considered. A wavelength shift of 0.15 nm is achieved for the attachment of 1 nm layer thickness. This shows an improvement by a factor of 20.5 with the SNOW ring resonator.

The dependence of the width for the SNOW was also considered. Figure 4.31 shows the percentage change in the effective-index of the SNOW structure as the waveguide width is changed from 300 nm to 1000 nm for a 1 nm thickness of the attached molecule layer. As opposed to the change in bulk refractive-index, the

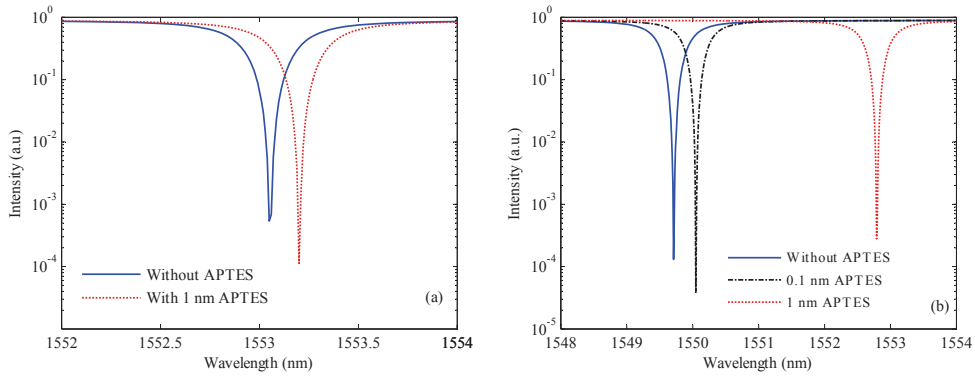

Figure 4.30: (a) Wavelength shift as 1 nm of layer is surface attached to the SOI waveguide (b) Wavelength shift as 1 nm of layer is surface attached to the SNOW ring. Wavelength shift due to a layer attachment of 0.1 nm is also shown [6].

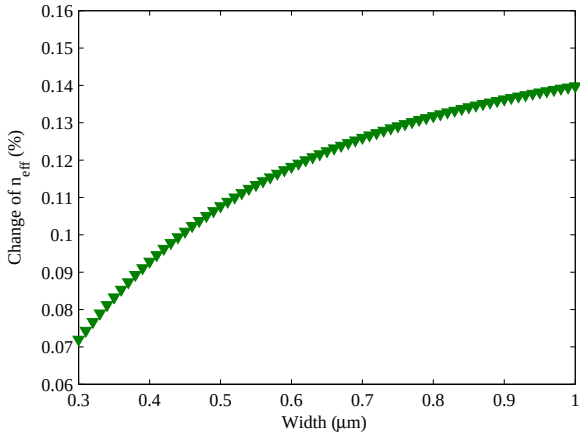

Figure 4.31: Change in the percentage of the effective-modal-index for 1 nm thickness of attached layers as the SNOW width is increased [6].

behavior is different and the sensitivity increases as the width is increased. This is because the sensor is not working in the evanescent field but within the core of the optical mode. As the width is increased, the optical mode gets more confined within the SNOW region resulting in higher interaction with the surface attached material.

Chapter 5

Novel Optical Sensors by SiNWs

In this chapter, vivid colors are demonstrated in silicon nanowires (SiNWs) with diameters ranging from 105 nm to 346 nm. The nanowires are vertically arranged in a square lattice with a pitch of 400 nm, and are electromagnetically coupled to each other resulting in frequency dependent reflection spectra. Since the coupling is dependent on the refractive index of the medium surrounding the nanowires, the arrays can be used for sensing. A simple sensor is demonstrated by observing the change in the reflected color with changing refractive index of the surrounding medium. A refractive index resolution of 5×10^{-5} is achieved by analyzing bright-field images captured with an optical microscope equipped with a charge coupled device camera.

5.1 Introduction

SiNWs also offer an increased surface to volume ratio, a property which can be used for sensing applications. This property has been demonstrated in porous silicon based optical interferometric biosensors [46], and and fluorescence sensors based on SiNWs [47]. In all of these experiments, an expensive measurement system is required such as spectrometers and tunable lasers, as they work by means of measuring the spectral changes in presence of the detectants. In recent years, another property of SiNWs has come to light: they reflect vivid colors. This result was first observed in a horizontal single SiNW on a substrate which were excited with incident light normal to the nanowires [124]. The vivid colors were a result of strong resonant light scattering due to the high refractive index mismatch between the SiNWs and the surrounding medium. Subsequently, colors with bright-field microscopy were also

observed in vertical single SiNWs due to a different physical mechanism [49]. The reflected colors resulted from the guided modes within the SiNWs coupling selectively with the substrate modes. In both cases, the colors were created by individual SiNWs with no coupling or diffractive effects. In this chapter, vertical arrays are fabricated where the nanowires are electromagnetically coupled to each other, and it is shown that as in [49] for individual nanowires, vivid colors can be generated for coupled arrays also. We demonstrate a very simple refractive index sensor by introducing controlled refractive index fluids within the nanowire arrays, capturing an image with a charge-coupled device (CCD) camera through bright-field microscope, and analysing the image for its red, green and blue content using the RGB additive model [125]. Using this simple setup, a refractive index resolution of 5×10^{-5} is achieved and compares well with integrated optics based sensors [126]. Changes in the background color are measured, where there are no nanowires present, and no change with refractive index is observed. Measurement of the same refractive index fluid is also achieved in a repeatable manner. The sensitivity to refractive index does not vary monotonically with diameter which strongly suggests that coupling plays a critical role in achieving these results. Furthermore, the color change is studied with temperature and a low sensitivity to temperature is measured.

5.2 Results and Discussion

A Silicon on Insulator (SOI) wafer was chosen since after etching of the nanowires, the residual silicon below can behave as a slab waveguide, enhancing the substrate modes. The diameters of nanowires were varied from 105 nm to 346 nm by changing the dosage in the EBL writing process. The nanowires were arranged in a square lattice with a pitch of 400 nm in arrays of 100 $\mu m \times 100$ μm. Figure 5.1 shows the scanning electron microscope (SEM) image for the 105 nm and 346 nm diameter nanowires. The SEM images show excellent uniformity in the diameter and position of the nanowires along with their vertical nature. In Chapter 2, we have shown that there is a critical diameter-length ratio above which the nanowires will remain vertical. In this study, the lowest diameter was chosen to be above the critical diameter for the length of the nanowires to make sure they are vertical.

Figure 5.2 shows bright-field optical microscope images of twelve sets of nanowire arrays. Each square consists of a 100 $\mu m \times 100$ μm array of nanowires of a specific diameter. The diameter increases in a raster scan along the rows. The difference in the colors of each square is clearly apparent and vivid colors covering the whole visible range could be obtained by changing the diameter. In order to understand

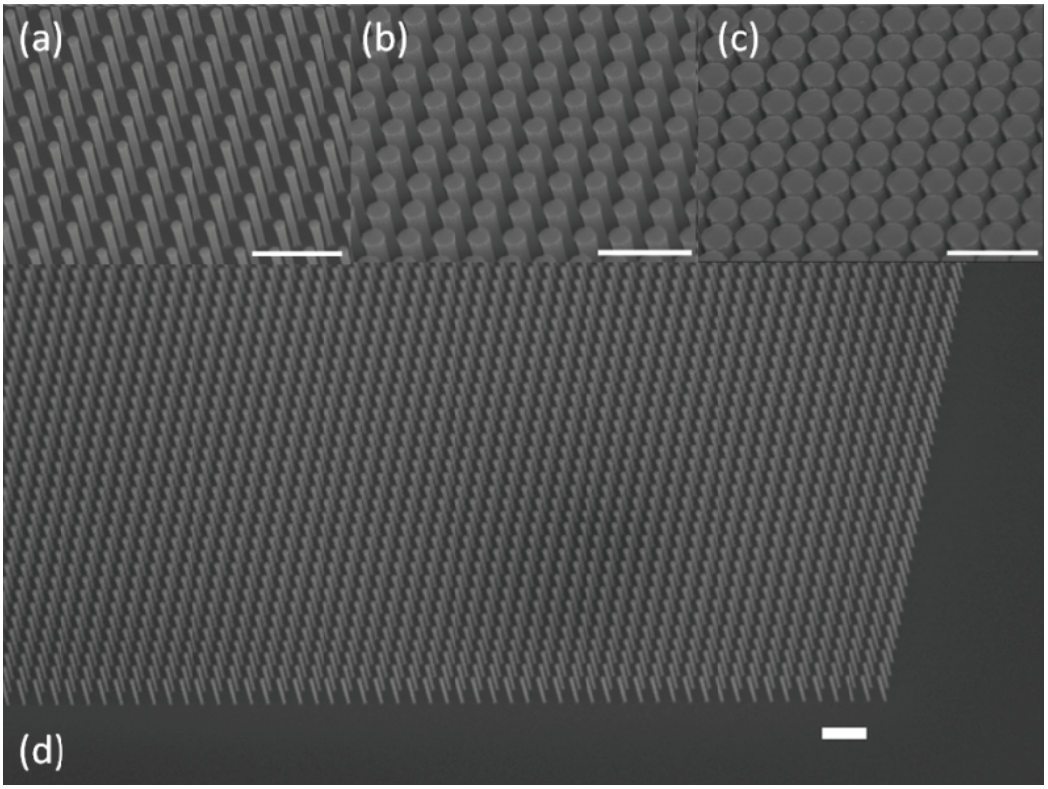

Figure 5.1: SEM images taken at 45 degree angle for nanowires with average diameters of (a) 105 nm (b) 230 nm (c) 346 nm (d) 105 nm. All scale bars are 1 μm [7].

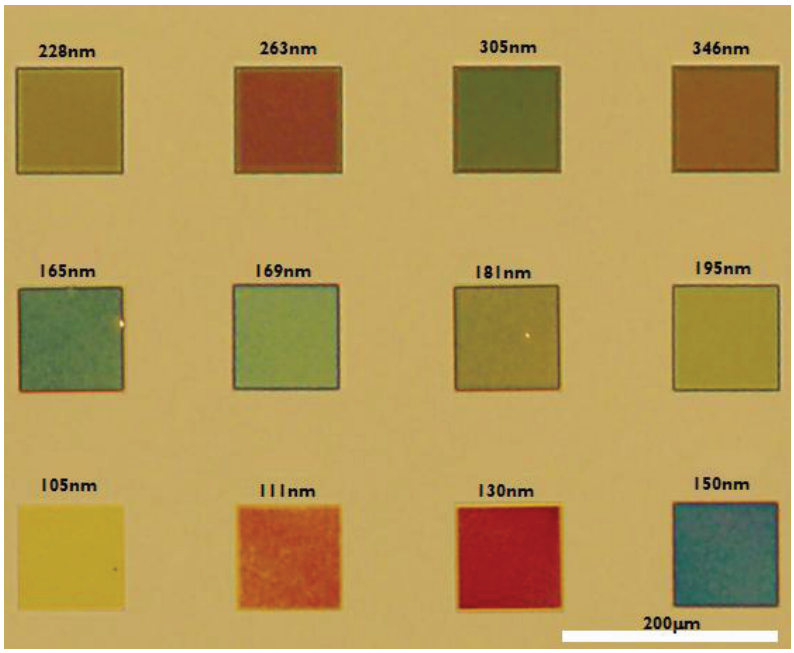

Figure 5.2: Bright-field optical microscope image of twelve different nanowire arrays. Vivid colors dependent on diameter are achieved. The scale bar is 200 μm [7].

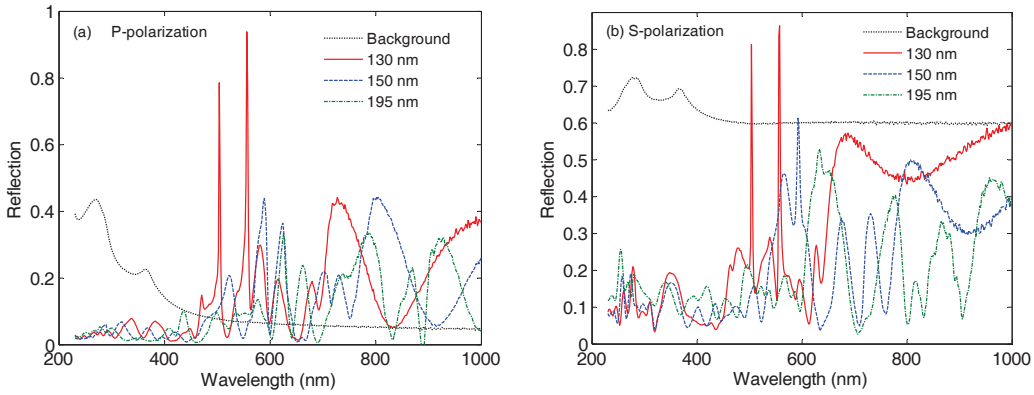

Figure 5.3: Reflections from SiNW array for three different diameters for (a) p-polarized input (b) s-polarized input. Reflection from bulk silicon (background) around the arrays is also shown [7].

whether the colors arise from single nanowires like in [49] or from other phenomena including coupling between the nanowires, polarization resolved reflections were measured using a focused beam with a J. A. Woollam M-2000 ellipsometer. The incident angle was 65° and the spot size of the beam was approximately 25 $\mu m \times 60$ μm, with a spectral resolution of 1.5 nm. Figure 5.3 (a) and (b) show the reflection spectrum for a few of these diameters in both p- and s-polarization, respectively. The reflections from the bulk silicon substrate are also shown for comparison. The measured reflection spectra are quite dissimilar to [49], where only one reflection minimum was observed which varied with diameter. For p-polarized incident light, the SiNW arrays exhibit higher reflections, and display frequency selective features resembling Fabry-Perot modes above the wavelength of 450 nm as compared to bulk silicon. For the s-polarized input, the reflections are generally lower, however some unique features are still observed. For the diameter of 130 nm, an increase in reflection occurs above the wavelength of approximately 645 nm as compared to below it. Above this wavelength, reflections approach that of silicon. A similar behavior is observed for the 150 nm diameter, except now the wavelength where this change happens is at approximately 780 nm. As the diameter is increased further to 195 nm, this transition is no longer observed. Additionally, multiple frequency bands in the reflection spectrum are observed where the peak separation corresponds to the Fabry-Perot modes of a 1 μm long cavity. As the diameter is increased, the number of these frequency bands also increases. For the diameter of 130 nm, the very sharp resonance like spectral features were observed at wavelengths 504 nm and 556 nm for both s-

and p-polarized inputs. For the diameter of 150 nm, similar sharp reflection peaks are observed around 592 nm. The widths of these spectral features were not resolved with our instrument. As the diameter is increased to 195 nm, these sharp features disappear. A few other nanowire diameters were measured, and while some show these sharp spectral features, others do not. Since the reflection features are highly dependent on the diameter of SiNWs and vary significantly as diameter is changed, the sensitivity should not change monotonically with diameter. This is in contrast to what one would expect for independent nanowires where the surrounding medium is only being interrogated by the evanescent fields.

Multiple phenomena occurring within the nanowire arrays result in the features observed in the measured reflection spectra. Firstly, the nanowire arrays act like a two dimensional dielectric grating [127,128]. SiNWs with residual silicon of the SOI wafer can support guided slab modes resulting in a resonant coupling between the incident wave and the guided modes. Due to the diffraction of light by the two dimensional periodicity, coupling of the incident wave with guided modes can occur in any direction within the grating waveguide [127]. This coupling has a resonant nature due to phase matching requirements. Different diffraction orders allow for the resonance to occur at different wavelengths. The reflection peaks can approach unity provided the material is loss-less. The reflection peaks have a bandwidth of less than 2 nm [128]. The behaviour of an array of SiNWs as a two dimensional grating results in the sharp reflection peaks as seen in the 130 nm and the 150 nm diameter nanowires. SiNWs on bulk silicon do not support the guided modes because of the lower effective index, and hence, we chose to use the SOI wafer as the modes are guided within the unetched silicon slab. For wavelengths where this resonance is not achieved, the SiNWs act like an effective index medium creating a Fabry-Perot cavity between the SiNW-air and the SiNW-silicon interfaces. However, near-field coupling between the neighboring nanowires can create another resonance effect. Similar coupling in photonic lattices has previously been investigated in vertical cavity surface emitting lasers (VCSELs) arrays for creating diffraction limited fields from multiple devices [65]. In order to confirm the effect of coherent coupling, a finite difference time domain (FDTD) simulation over the entire wavelength range was performed. Since the optical properties of silicon vary over the wavelength range between the Fabry-Perot peaks, it becomes difficult to ascertain the role of coupling versus Fabry-Perot interferences in the reflection spectrum. Hence, in the first simulation the nanowires were considered to be semi-infinite by using a perfectly matched layer boundary at the bottom, allowing one to see the effect of the near field coupling between the nanowires. Figure 5.4 plots the simulated reflections from these nanowires as the diameter is changed. For all diameters, we see a peak in the reflection spectrum which changes in value

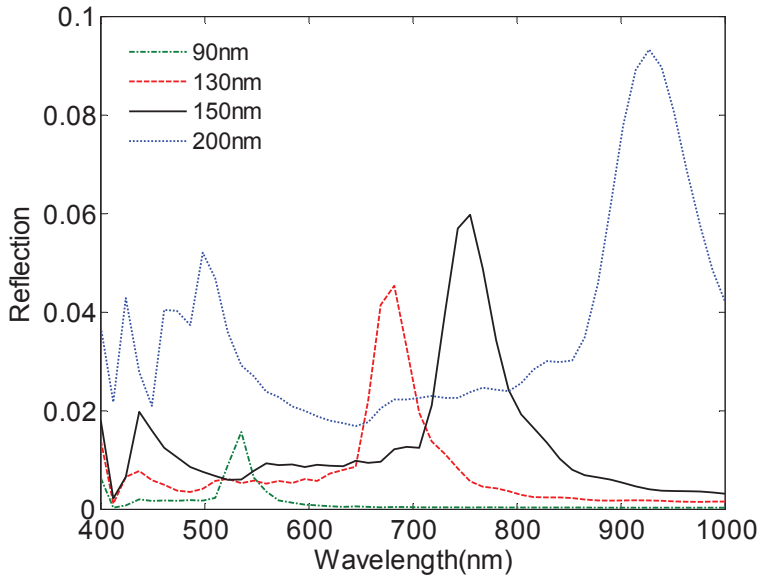

Figure 5.4: Reflection from semi-infinitely long silicon nanowires for different diameters [7].

and position depending on the diameter. As the diameter is increased, the intensity of the reflection peak increases and shifts towards longer wavelengths. Further, the reflection peak has a resonance-like bandwidth with full-width half maximum values of $\sim 50\ nm$ for diameters of 130 nm and 150 nm and $\sim 75\ nm$ for the diameter of 200 nm. The peaks observed in the simulations exactly correspond to the wavelengths where the reflection sharply starts to approach that of bulk silicon are observed in the experimental s-polarized reflections. The resonant near field coupling increases the confinement of light within the SiNWs thus creating a larger index mismatch, increasing the reflection from the array. The absorption within the nanowires also increases at the same place due to the increased confinement. Thus, the incident beam is better absorbed within the nanowires and sees less of the SiNW-Si interface. Since, the reflection values from semi-infinite nanowires are small themselves, the reflection from the nanowire-silicon interface plays an important role in producing the observed spectrum. The effect of the Fabry-Perot modes created between the air-nanowire interface and nanowire-silicon interface was also simulated using the complete structure. The electric field distributions within the nanowires are shown in Fig. 5.5 (d-e), for three different diameters, for an incident wavelength of 630 nm. A very strong enhancement of the electric field is observed for the 115 nm diameter as compared to the diameters near this value. Electric field distribution for the same

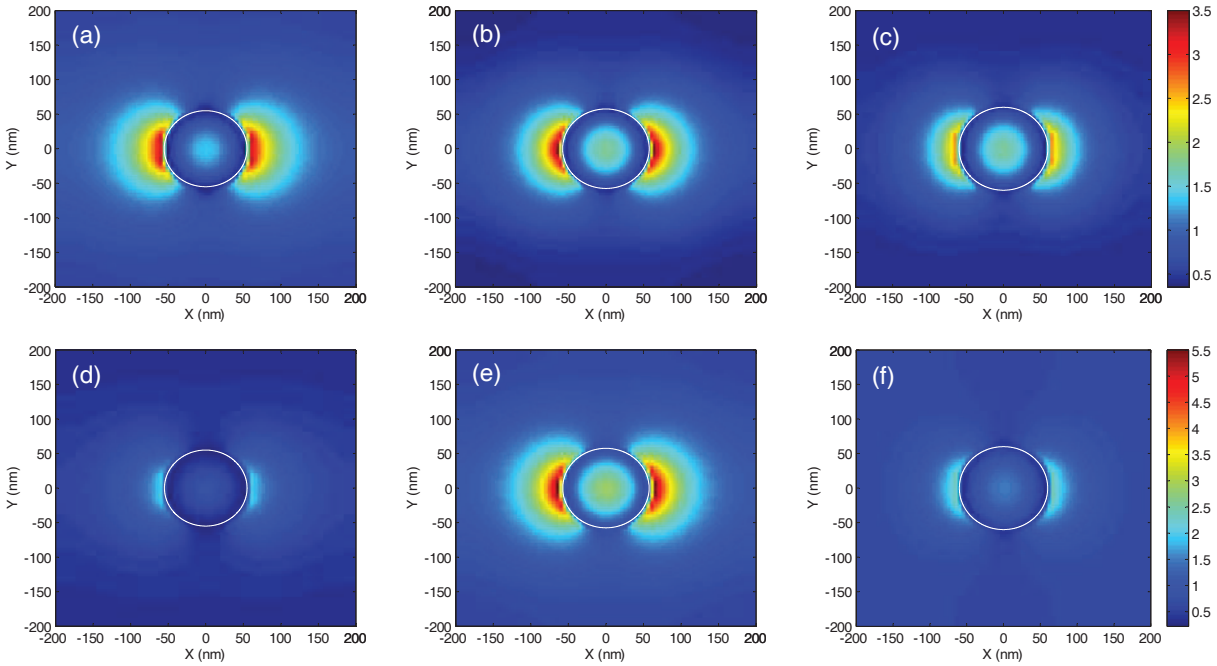

Figure 5.5: Electric field distributions for diameters of (a) 110 nm (b) 115 nm and (c) 120 nm for semi-infinitely long nanowires. Electric field distributions for diameters of (d) 110 nm (e) 115 nm and (f) 120 nm for 1 μm long nanowires on SOI wafer [7].

diameters for semi-infinitely long nanowires is also shown in Fig. 5.5(a-c). When the SiNWs are considered to be semi-infinite, the confinement of the light is again higher for the 115 nm diameter due to near field coupling, but the enhancement is not as large as when placed in a cavity. This strong enhancement results from the fact that for this diameter, a Fabry-Perot mode has a maximum at the top of the nanowire, building up the intensity. At the same time, near field coupling has significantly enhanced the electric field within the nanowire. Hence, both length and the diameter of the nanowires plays an important role in producing the observed colors. In order to confirm this, two different lengths were fabricated, and the observed colors were only slightly different for the different lengths. Accordingly, the observed colors are mainly from the emergent optical properties of SiNWs arranged in a square array. The advantage of SiNWs is the large refractive index contrast with air. As such if nanowires with lower refractive index materials like cadmium sulphide (CdS) are used, we do not expect vivid colors to be observed. Also since the reflections over a broader wavelength range are due to the Fabry-Perot cavity created between the air-nanowire and nanowire-silicon interfaces, the absorption of light within the nanowires also play a role in the reflection spectrum. Thus, for shorter wavelengths, (< 400 nm) where the absorptions are high, the reflections are very weak as seen in Fig. 5.3. Within our structure, we had expected to create another resonance due to coupled-cavity between the SiNW-air, SiNW-Si and Si-oxide interface. However, within the experimental data no Fabry-Perot modes from the Si-oxide interface were observed. This was confirmed by measuring the reflections from an area beside the arrays where only unetched silicon was present. The reflections observed were exactly the same as the bulk silicon. The reason for the lack of Fabry-Perot interferences could be due to the large surface roughness between the Si-oxide layers within the starting wafer.

The coupling between nanowires and the Fabry-Perot cavity creates the sharp reflection features and the resultant colors. In keeping with this, it was envisioned that the reflection spectra will be dependent on the refractive index of the surrounding medium. If the change in color with the surrounding index medium could be measured, then a simple refractive index sensor with no costly optics can be considered. In order to quantify this, an experiment was conducted using Cargille refractive index fluids [129] of known refractive indices ranging from 1.3 to 1.39. Cargille refractive index fluids contain chlorofluorocarbons with high stability and wettability to surfaces. Also, etched SiNWs have shown to have superhydrophilic surfaces due to a hemi-wicking phenomenon [130], provided the surface roughness is small, which is true in our case, meaning the arrays could be used to test for a wide variety of different liquids. Additionally, excellent repeatability was previously achieved in connection

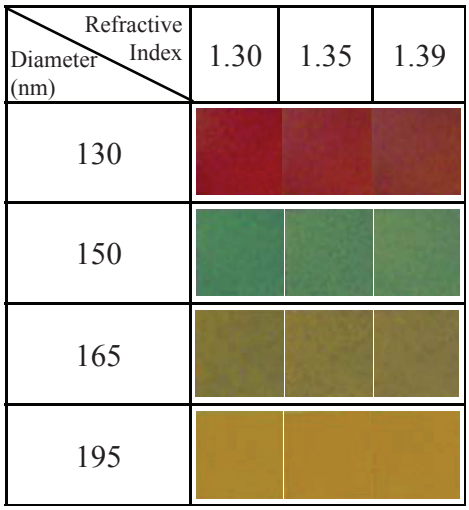

Figure 5.6: Bright-field microscope images of four different diameters with changing refractive index of the surrounding medium. Arrays with diameters of 130 nm and 150 nm show a perceptible change to the naked eye whereas for diameters of 165 nm and 195 nm, the change is weak [7].

with these fluids on etched optical fiber sensors [131]. The fluids were introduced in between the nanowires and an image of the nanowires was captured. This range of the refractive index was chosen since the refractive index of water (1.33) and many other liquids of interest for bio-chemical sensing lie within these values. Figure 5.6 plots the bright-field microscope images for four different arrays consisting of SiNWs with average diameters of 130 nm, 150 nm, 165 nm and 195 nm. Diameters of 130 nm and 150 nm displayed the sharp spectral peaks whereas for the diameters of 165 nm and 195 nm such features were not observed. As the refractive index of the surrounding fluid, and hence the surrounding medium changes, the corresponding variation in reflected color is clearly perceptible for the diameters of 130 nm and 150 nm, while the change is weak for the other two diameters. These results complement the experimental data where sharp reflection features were observed for the same SiNW diameters. Thus, just by simply measuring the reflected colors using a simple camera, following by performing basic image processing, a refractive index sensor can be realized.

In order to quantify the sensitivity of the color change with the refractive index of the surrounding medium, the red (R) green (G) and blue (B) values for the images

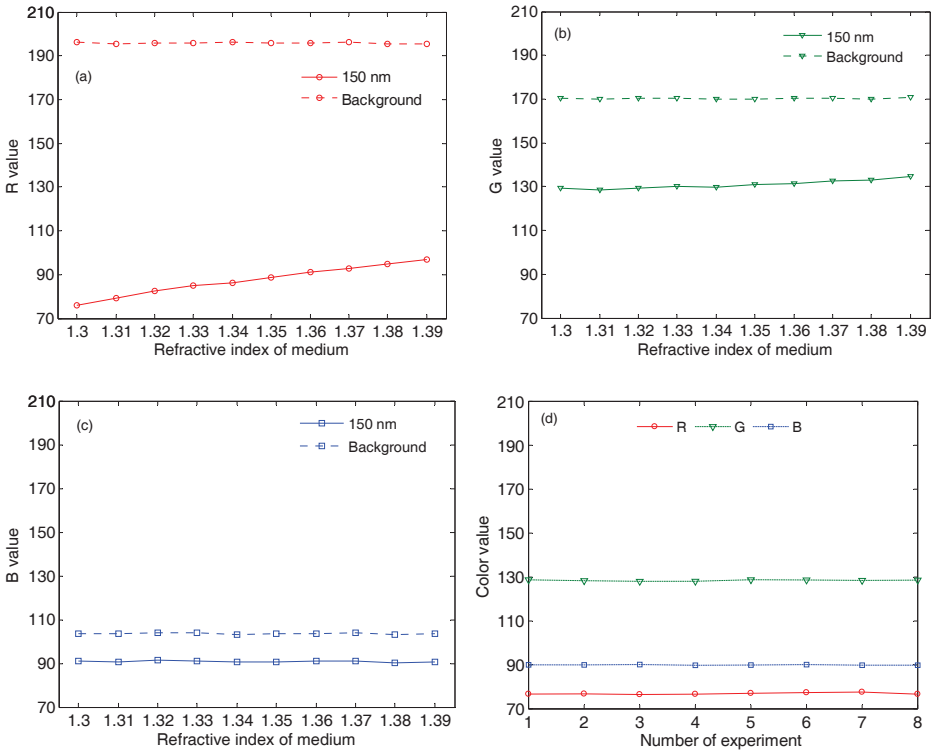

Figure 5.7: Values for nanowires with diameter of 150 nm for (a) R (b) G and (c) B from the reflected colors as the refractive index of the surrounding medium is changed. Values for the background where no nanowires are present are also shown. (d) R, G and B values for the refractive index of 1.3 for 8 different experiments done independently [7].

of the arrays were calculated using the additive RGB model. Each combination of R, G and B value gives a unique color. Figure 5.7 plots the change in R, G, and B values for an array of SiNWs with a diameter 150 nm. The R, G, and B values from the background where there are no nanowires are also shown. This measurement was done to make sure that the color change was not from the different fluids used but from the interaction of the liquid with the nanowires themselves. For this diameter, the R value changes linearly with increasing refractive indices while G and B values do not change appreciably. Another experiment was also performed to gauge the repeatability of the measurement where a fluid with a refractive index of 1.3 was introduced to the nanowire arrays 8 different times. The results for the same array are plotted in Fig. 5.7(d). During all these measurements, the sample was taken

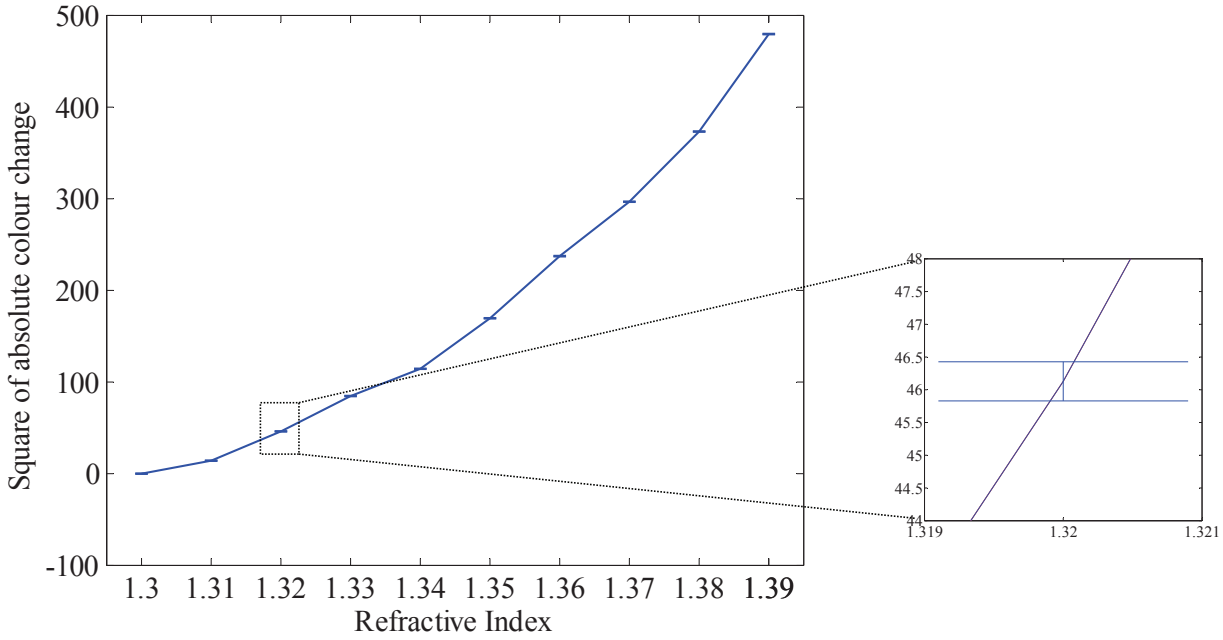

Figure 5.8: Square of absolute colour change versus refractive index of surrounding media [7].

off the microscope stage, cleaned with isopropanol and blow dried before the fluid was introduced again. Good repeatability of the measurements was achieved with a standard deviation of 0.3 in the values of R, G and B. If one only considers the R values for this diameter, then a refractive index resolution of 1×10^{-3} is achieved. However, since each combination of R, G and B is a unique color, one should be able to increase the sensitivity by combining the changes in all the three color values. In order to compare the different arrays, the changes in the values of R, G and B (R, G, B) from the reference value at 1.3 were computed, and the square of the changes were added together.

The sensitivity of the sensor, S, is defined as the average change of $(\triangle R)^2 + (\triangle G)^2 + (\triangle B)^2$ versus the change of refractive index of the surrounding medium over the measured range. R, G, and B are the changes in the values of R, G and B respectively from the reference. The index resolution is defined as twice the standard deviation divided by S. As shown in Fig. 5.8, the value of $(\triangle R)^2 + (\triangle G)^2 + (\triangle B)^2$ versus refractive index is plotted for 150 nm diameter along with a fit to the data allowing for the calculation of S. The standard deviation of the data in the

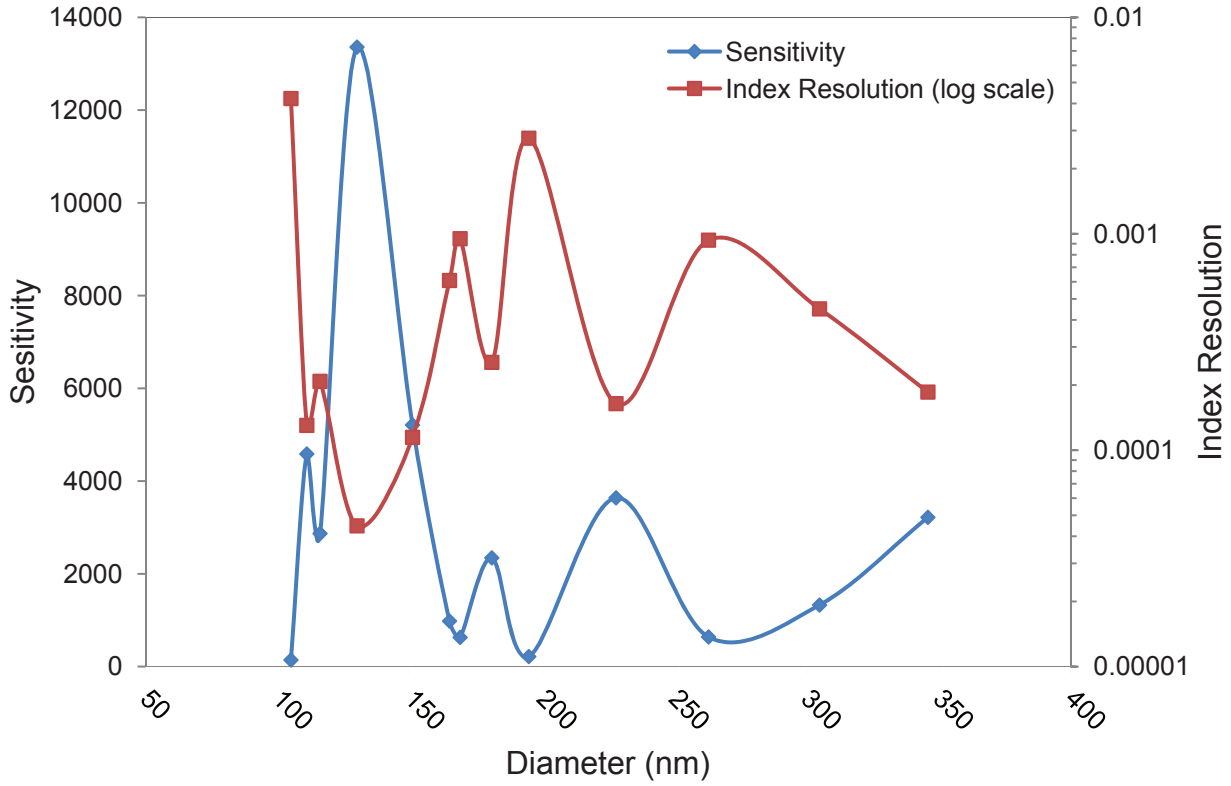

Figure 5.9: Sensitivity and index resolution as function of diameter of the nanowire arrays [7].

experiments from multiple measurements is very small and error bars do not show well in the figure. An inset is plotted for ease of visualization. The sensitivity, S, is calculated as the slope of the change in colors with refractive index plotted in Fig. 5.9 for different diameters. Using the standard deviation value from the repeatability measurements, the refractive index resolution was calculated as the ratio of twice the standard deviation and S, and is plotted in the same figure for different diameters. The best refractive index resolution achieved was 5×10^{-5} for the array with diameter of 130 nm. Both 130 nm and 150 nm diameters achieve an index resolution of less than 1×10^{-4}. This compares well with photonic based integrated circuit sensors with a sensitivity of 250 nm/RIU assuming a spectral resolution of 0.01 nm [121]. Once again, the arrays with the highest resolution (130 nm and 150 nm) also had the sharpest features in their corresponding reflection spectra. The resolution does not change monotonically like it would if the nanowires were acting individually.

For example, the sensitivity degrades as the diameter is increased or decreased from 130 nm. For a diameter of 105 nm, the sensitivity is only 5×10^{-3}; two orders of magnitude lower than the diameter of 130 nm. As the diameter is reduced the evanescent field increases [6] and sensitivity should have increased if the nanowires were acting individually. By taking advantage of the coherent coupling between the nanowires, the sensitivity to color change has been increased appreciably in our experiment beyond what is expected from the evanescent fields. Optimization of the pitch and the length of the nanowires is currently being pursued as it may further increase the sensitivity and refractive index resolution.

The sensitivity of the color change with respect to temperature was measured by heating the sample to $225°C$ and capturing images in steps of every $10°C$, down to room temperature. The temperature was measured directly on the sample by a laser infrared scope. The values of the color change are plotted in Fig. 5.10 showing little temperature dependence as compared to refractive index changes. Thus, not only a good refractive index resolution is achieved with a simple camera, the color change is also insensitive to temperature changes, especially for values around room temperature. For the arrays with highest sensitivity to refractive index, the change in the values of R and G showed opposite trends. While R changed with increasing refractive index, G changed more with temperature. Thus, by using these components separately, the changes in temperature and refractive index may be measured simultaneously and is being currently investigated. This uses the same principle that has been previously demonstrated by us for etched core fiber Bragg grating sensors [131].

In conclusion, this study has shown that coupled nanowire arrays also reflect vivid colors as single nanowires do. Furthermore, by tuning the diameter, strong coupling between the nanowires is achieved and results in an enhanced electric field in the area surrounding the nanowires. The coupling was confirmed by measuring the polarization resolved reflections from the arrays and FDTD simulations. The change in color was measured by introducing Cargille refractive index fluids and perceptible change in color was obtained for coupled nanowire arrays. The experiments were repeatable and an index resolution of 5×10^{-5} was achieved by simply analyzing the images and adding the square of the changes in the values of R, G and B for different refractive indices. Different diameters had remarkably different sensitivities to color change, again confirming the fact that coupling between the nanowires plays an important role, and the sensitivity does not monotonically vary with diameter. The color change with temperature was also measured and was found to be much less sensitive as compared to small changes in refractive index. The results suggest that SiNWs can be used as platforms for low cost refractive index sensors using a simple CCD camera.

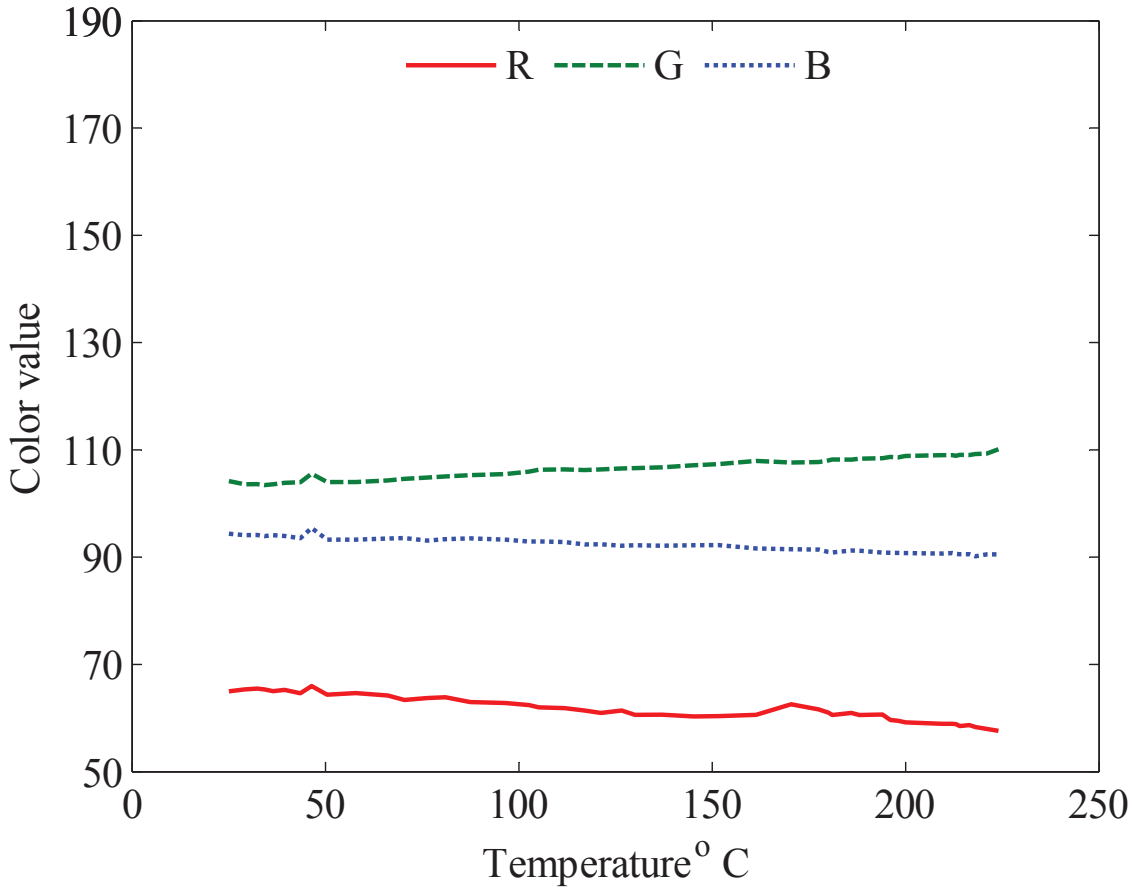

Figure 5.10: R, G, and B values versus temperature change for the array with nanowires of diameter 150 nm [7].

Chapter 6

Summary of Completed and Future Works

6.1 Summary of Completed Work

The objective of this research was to create a platform based on Silicon Nanowires (SiNWs) and apply it to various applications. Essential physical properties of nanowires can be altered with regard to properties of bulk material which brings a possibility to improve performance of different devices. Specially, we are expecting an improved electrostatics characteristic due to 3-dimensional nature and quantum confinement of carrier can lead to increased sensitivity for these kinds of devices.

As a summary of the work done so far, we:

1. **Developed** all steps of fabrication process to create high-anisotropic silicon nanowires using top-down approach, electron beam lithography followed by reactive ion etching. Silicon nanowire as small as 15 nm in diameters to the length of few micrometers have been fabricated by this method.

2. **Proposed** a novel optical waveguide called Silicon Nanowire Optical Waveguide (SNOW). SNOW bridges the gap between the "nanoscopic" and microscopic world in that while light interacts with the nano-confined SiNWs, the optical mode resembles that of conventional waveguides, requiring conventional micro-lenses for coupling light in and out of SNOW structures. As a potential application, a high-sensitive bio-sensor was designed and simulated based on SNOW concept.

3. **Proposed** and analyzed novel ring resonator based bio-chemical sensors on silicon nanowire optical waveguide (SNOW) and show that the sensitivity of the sensors can be increased by an order of magnitude as compared to silicon-on-insulator based ring resonators while maintaining high index contrast and compact devices.

4. **Demonstrate** vivid colors in mutually coupled silicon nanowires with diameters ranging from 105 nm to 345 nm. A simple sensor was demonstrated by observing the change in the reflected color with changing refractive index of the surrounding medium. A refractive index resolution of 5×10^{-5} is achieved using a simple charge coupled device (CCD) camera.

5. **Demonstrated** Second Harmonic Generation (SHG) in silicon nanowires for the first time. While SHG is forbidden in silicon with inversion symmetry, it can be allowed on the surface due to broken symmetry. This discovery introduces potential applications in silicon that were not possible before.

6. **Implemented** a model to describe Raman scattering enhancement in silicon nanowires. Experimental results show excellent agreements with theoretical predictions. This model is important, especially in design and simulation of optical devices based on nonlinear Raman effects such as optical bio-sensors. Enhanced Raman intensity by a factor of 15 was achieved for the first time.

7. **Implemented** a model to describe Raman scattering enhancement in silicon nanowires. Experimental results show excellent agreements with theoretical predictions. This model is important, especially in design and simulation of optical devices based on nonlinear Raman effects such as optical bio-sensors. Enhanced Raman intensity by a factor of 15 was achieved for the first time.

8. **Studied** and modeled polarization resolved reflection of SiNWs to investigate light trapping properties.

9. **Proposed** and simulated multiple all-optical logic operations in silicon on insulator waveguides based on three nonlinear phenomena, stimulated Raman scattering, free carrier absorption, and cross phase modulation.

6.2 Future Works

1. **Design** and fabricate photodetector based on the understanding that we archived by polarization resolved measurement.

2. **Enhance** Raman scattering from array of SiNWs by coating the nanowires with noble metals, such as Ag or Au. This is promising for several applications including surface-enhanced Raman spectroscopy.

3. **Realize** terahertz (THz) source using SiNWs. As shown before second-harmonic generation (SHG), one of the well-known phenomena for THz radiation, is possible in self-strained SiNWs which opens a window to fulfill this desire.

References

[1] M. Khorasaninejad N. Abedzadeh A. S. Jawanda N. O M. P. Anantram S. S. Saini. Bunching characteristics of silicon nanowire arrays. *J. Appl. Phys.*, 111, 2012.

[2] M. Khorasaninjead N. Abedzadeh J. Sun J. N. Hilfiker S. S. Saini. Polarization resolved reflection from ordered vertical silicon nanowire arrays. 37:2961–2963, 2012.

[3] M. Khorasaninejad J. Walia S. S. Saini. Enhanced first order raman scattering from arrays of vertical silicon nanowires. *Nanotechnology (IOP)*, 23:1–7, 2012.

[4] M. Khorasaninejad S. S. Saini. Silicon nanowire optical waveguide (snow). *Optics Express*, 18:23442–23457, 2010.

[5] M. Khorasaninejad S. S. Saini. Bend-waveguides on silicon nanowire optical waveguide (snow). *IEEE Photonics Journal*, 3:696 –702, 2011.

[6] M. Khorasaninejad N. Clarke M. P. Anantram S. S. Saini. Optical bio-chemical sensors on snow ring resonators. *Optics Express*, 19:17575–17584, 2011.

[7] M. Khorasaninejad N. Abedzadeh J. Walia S. Patchett S. S. Saini. Color matrix refractive index sensors using coupled vertical silicon nanowire arrays. *Nano Letters*, 12:42284234, 2012.

[8] B. Jalali S. Fathpour. Silicon photonics. *IEEE J. of Lightwave Technology*, 24:4600–4615, 2006.

[9] L. Liao D. Samara-Rubio M. Morse A. Liu D. Hodge D. Rubin U. D. Keil T. Franck. High speed silicon mach-zehnder modulator. *Opt. Express*, 13:3129–3135, 2005.

[10] V. R. Almeida C. A. Barrios R. R. Panepucci M. Lipson M. A. Foster D. G. Ouzounov A. L. Gaeta. All-optical switching on a silicon chip. *Opt.Lett.*, 29:2867–2869, 2004.

[11] M. S. Unlu M. K. Emsley O. I. Dosunmu P. Muller Y. Leblebici. High-speed si resonant cavity enhanced photodetectors and arrays. *J. Vac. Sci. Technol. A*, 22:781–787, 2004.

[12] A. Liu H. Rong R. Jones O. Cohen D. Hak M. Paniccia. Optical amplification and lasing by stimulated raman scattering in silicon waveguides. *J. Lightwave Technol.*, 24:1440–1455, 2006.

[13] R. Jones A. Liu H. Rong M. Paniccia O. Cohen D. Hak. Lossless optical modulation in a silicon waveguide using stimulated raman scattering. *Opt. Express*, 13:1716–1723, 2005.

[14] M. Khorasaninejad S. S. Saini. All-optical logic using nonlinear effects in silicon-on-insulator waveguides. *Appl. Opt.*, 48:F32–F37, 2009.

[15] M. A. Foster A. C. Turner J. E. Sharping B. S. Schmidt M. Lipson A. L. Gaeta. Broad-band optical parametric gain on a silicon photonic chip. *Nature*, 441:960–963, 2006.

[16] L. T. Canham. Silicon quantum wire array fabrication by electrochemical and chemical dissolution of wafers. *Appl. Phys. lett.*, page 57, 1990.

[17] L. Brus. Luminescence of silicon materials: Chains, sheets, nanocrystals, nanowires, microcrystals, and porous silicon. *J. Phys. Chem.*, 98:3515–3581, 1994.

[18] D. P. Yu Z. G. Bai Y. Ding Q. L. Hang H. Z. Zhang J. J. Wang Y. H. Zou W. Qian G. C. Xiong H. T. Zhou S. Q. Feng. Nanoscale silicon wires synthesized using simple physical evaporation. 72:3458–3460, 1998.

[19] J. D. Holmes K. P. Johnston R. C. Doty B. A. Korgel. Control of thickness and orientation of solution-grown silicon nanowires. *Science*, 287:1471–1473, 2000.

[20] Y. F. Zhang Y. H. Tang H. Y. Peng N. Wang C. S. Lee I. Bello S. T. Lee. Diameter modification of silicon nanowires by ambient gas. *Appl. Phys. Lett.*, 75:1842–1844, 1999.

[21] A. G. Nassiopoulos S. Grigoropoulos D. Papadimitriou. Electroluminescent device based on silicon nanopillars. *Appl. Phys. Lett.*, 69:2267–2269, 1996.

[22] J. Huo R. Solanki J. L. Freeouf J. R. Carruthers. Electroluminescence from silicon nanowires. *Nanotechnology*, 15:1848–1859, 2004.

[23] G. T. Reed C. E. J. Peng. Silicon optical modulators. *Mater. Today*, 8:40–50, 2005.

[24] G. Lupke D. J. Bottomley H. M. van Driel. Sio2/si interfacial structure on vicinal si(100) studied with second-harmonic generation. *Physical Review B*, 47:10389–94, 1993.

[25] P. Figliozzi L. Sun Y. Jiang N. Matlis B. Mattern M. C. Downer S. P. Withrow C.W. White W. L. Mochan B. S. Mendoza. Single-beam and enhanced two-beam second-harmonic generation from silicon nanocrystals by use of spatially inhomogeneous femtosecond pulses. *Phys. Rev. Lett.*, 94:047401, 2005.

[26] R. S. Jacobsen K. N. Anderson P. I. Borel J. Fadge-Pedersen L. H. Frandsen O. Hansen M. Kristensen A. V. Lavrinenko G. Moulin H. Ou C. Peucheret B. Zsigri A. Bjarklev. Strained silicon as a new electro-optic material. *Nature*, 441:2006, 199-202.

[27] T. V. Dolgova A. I. Maidykovski M. G. Martemyanov A. A. Fedyanin O. A. Aktsipetrov G. Marowsky V. A. Yakovlev G. Mattei. Giant microcavity enhancement of second-harmonic generation in all-silicon photonics crystals. *Appl. Phys. Lett.*, 81:2725–2727, 2002.

[28] M. Wachter C. Matheisen M. Waldow T. Wahlbrink J. Bolten M. Nagel H. Kurz. Optical generation of terahertz and second-harmonic light in plasma-activated silicon nanophotonic structures. *Applied Physics Letters*, 97:161107, 2010.

[29] S. S. Walavalkar A. P. Homyk M. D. Henry A. Scherer. Controllable deformation of silicon nanowires with strain up to 24%. *Journ. Appl. Phys.*, 107:124314 – 124314–5, 2010.

[30] T. R. Hart R. L. Aggarwal B. Lax. Temperature dependence of raman scattering in silicon. *Phys. Rev. B*, pages 638–642, 1970.

[31] P. A. Temple C. E Hathaway. Multiphonon raman spectrum of silicon. *Phys. Rev. B*, 7:3685–3697, 1971.

[32] L. Cao B. Nabet J. E. Spanier. Enhanced raman scattering from individual semiconductor nanocones and nanowires. *Phys. Rev. Lett.*, 96:157402, 2006.

[33] J. A. Huang Y. Q. Zhao X. J. Zhang L. B. Luo Y. K. Liu J. A. Zapien C. Surya S. T. Lee. Enhanced raman scattering from vertical silicon nanowires array. *Appl. Phys. Lett.*, 98:183108, 2011.

[34] C. G. Bernhard. Structural and functional adaptation in a visual system. *Endeavour*, 26:79–84, 1967.

[35] P.B. Clapham M.C Hutley. Reduction of lens reflexion by the.

[36] J. I. Gittleman E. K. Sichel H. W. Lehmann R. Widmer. Textured silicon: A selective absorber for solar thermal conversion. *Appl. Phys. Lett.*, 35:742–744, 1979.

[37] H. G. Craighead R. E. Howard D. M. Tenant. Textured thin film si solar-selective absorbers using reactive ion etching. *Appl. Phys. Lett.*, 37:653655, 1980.

[38] K. Peng Y. Xu Y. Wu Y. Yan S.T. Lee J. Zhu*. Aligned single-crystalline si nanowire arrays for photovoltaic applications. *Small*, 1:1062–1067, 2005.

[39] L. Tsakalakos J. Balch J. Fronheiser B. A. Korevaar O. Sulima J. Rand. Silicon nanowire solar cells. *Appl. Phys. Lett*, 91:233117–1–3, 2007.

[40] Y. Kanamori M. Sasaki K. Hane. Broadband antireflection gratings fabricated upon silicon substrates,. *Opt. Lett.*, 24:1422–1424, 1999.

[41] Y. F. Huang S. Chattopadhyay Y. J. Jen C. Y. Peng T. A. Liu Y. K. Hsu C. L. Pan H. C. Lo C. H. Hsu Y. H. Chang C. S. Lee K. H. Chen L. C. Chen. Improved broadband and quasi-omnidirectional anti-reflection properties with biomimetic silicon nanostructures. *Nat. Nanotechnol.*, 2:770–774, 2007.

[42] L. Hu and G. Chen. Analysis of optical absorption in silicon nanowire arrays for photovoltaic applications. *Nano Lett.*, 7:32493252, 2007.

[43] E. Garnett and P. Yang. Light trapping in silicon nanowire solar cells. *Nano Lett.*, 10:10821087, 2010.

[44] Z. Li Y. Chen X. Li T. I. Kamins K. Nauka R. S. Williams. Sequence-specific label-free dna sensors based on silicon nanowires. *Nano Lett.*, 4:245247, 2004.

[45] W. Chen H. Yao C. H. Tzang J. Zhu M. Yang S. T. Lee. Silicon nanowires for high-sensitivity glucose detection. *Appl. Phys. Lett.*, 88:213104, 2006.

[46] V. S. Y. Lin K. Motesharei K. P. S. Dancil M. J. Sailor M. R. Ghadiri. A porous silicon-based optical interferometric biosensor. *Science*, 278:840–843, 1997.

[47] L. Mu W. Shi J. C. Chang S. T. Lee. Silicon nanowires-based fluorescence sensor for cu(ii). *Nano Lett.*, 8:104–109, 2008.

[48] M. D. Henry S. Walavalkar A. Homyk A.Scherer. Alumina etch masks for fabrication of high-aspect-ratio silicon micropillars and nanopillars. *Nanotechnology*, 20:1–4, 2009.

[49] K. Seo M. Wober P. Steinvurzal E. Schonbrun Y. Dan T. Ellenbogen K. B. Crozier. Multicolored vertical silicon nanowires. *Nano Letts.*, 11:1851–1856, 2011.

[50] R. S. Wagner W. C. Ellis. Vapor liquid solid mechanism of single crystal growth. *Appl. Phys. Lett.*, 4:89–90, 1964.

[51] R. S. Wagner C. J. Doherty. Mechanism of branching and kinking during vls crystal growth. *Electrochemical Society*, 115:93–99, 1968.

[52] Y. F. Zhang Y.H. Tang C. Lam N. Wang C.S. Lee I. Bello S.T. Lee. Bulk-quantitysinanowiressynthesized by sio sublimation. *J. of Crystal Growth*, 212:115–118, 2000.

[53] N. Wang Y. H. Tang Y.F. Zhang C. S. Lee I. Bello S. T. Lee. Si nanowires grown from silicon oxide. *Chemical Physics Letters*, 299:237242, 1999.

[54] N. Wang Y. F. Zhang Y. H. Tang C. S. Lee S. T. Lee. Sio2-enhanced synthesis of si nanowires by laser ablation. *Appl. Phys. Lett.*, 73:3902–3904, 1998.

[55] D. Routkevitch A. A. Tager J. Haruyama D. Almawlawi M. Moskovits J. M. Xu. Nonlithographic nano-wire arrays: fabrication, physics, and device applications. *IEEE Transactions on Electron Devices.*, 43:1646–1658, 1996.

[56] D. Al-Mawlawi C.Z. Liu M. Moskovits. Nanowires formed in anodic oxide nanotemplates. *Materials Research.*

[57] D. Xu X. Shi G. Guo L. Gui Y. Tang. Electrochemical preparation of CdSe nanowire arrays. *Physical Chemistry B*, 104:50615063, 2000.

[58] H. Bao and X. Ruan. Optical absorption enhancement in disordered vertical silicon nanowire arrays for photovoltaic applications. *Opt. Lett.*, 35:3378–3380, 2010.

[59] M. F. L. De Volder D. O. Vidaud E. R. Meshot S. Tawfick and A. John Hart. Self-similar organization of arrays of individual carbon nanotubes and carbon nanotube micropillars. *Microelectronic Engineering*, 87:1233–1238, 2010.

[60] J. N. Israelachvili. *Intermolecular and Surface Forces*. Academic Press, Third ed., 2011.

[61] C. Lin and M. L. Povinelli. Optical absorption enhancement in silicon nanowire arrays with a large lattice constant for photovoltaic applications. *Opt. Express*, 17:19371–19381, 2009.

[62] S-H. Hsu E-S. Liu Y-C. Chang J. N. Hilfiker Y. D. Kim T. J. Jim C-J. Lin G-R. Lin. Characterization of si nanorods by spectroscopic ellipsometry with efficient theoretical modeling. *Phys. Stat. Sol. (a)*, 205:876–879, 2008.

[63] DiffractMod. Rsoft inc., http://www.rsoftinc.com.

[64] W. Q. Xie J. I. Oh W. Z. Shen. Realization of effective light trapping and omnidirectional antireflection in smooth surface silicon nanowire arrays. *Nanotechnology*, 22:1–9, 2011.

[65] L. J. Mawst D. Zhou and Z Dai. Modal properties of two-dimensional antiguided vertical-cavity surface-emitting laser arrays. *IEEE J. Quantum Electron.*, 38:652–664, 2002.

[66] L. D. Landau E. M. Lifshitz L. P. Pitaevskii. *Electrodynamics of Continuous Media*. Pergamon, pp 34-42, 1984.

[67] D. Kovalev M. Ben Chorin J. Diener F. Koch Al. L. Efros M. Rosen N. A. Gippius S. G. Tikhodeev. Porous si anisotropy from photoluminescence polarization. *Appl. Phys. Lett.*, 67:1585, 1995.

[68] Y. Ogata N. A. Tuan S. Takase G. Mizutani. Polarization and azimuthal angle dependence of the optical second harmonic generation from pt nanowires on the mgo(110) faceted template. *Suf. Interface Anal*, 42:1663–1666, 2010.

[69] B. Li D. Yu S. L. Zhang. Raman spectral study of silicon nanowires. *Phys. Rev., B*, 59, 1999.

[70] R. Wang G. Zhou Y. Liu S. Pan H. Zhang D. Yu Z. Zhang. Raman spectral study of silicon nanowires: High-order scattering and phonon confinement effects. *Phys. Rev. B*, 61:16827–16832, 2000.

[71] Z. Su J. Sha G. Pan J. Liu D. Yang C. Dickinson W. Zhou. Temperature-dependant raman scattering of silicon nanowires. *J. Phys. Chem. B*, 110:1229–1234, 2006.

[72] Y. Chen B. Peng B. Wang. Raman spectra and temperature-dependent raman scattering of silicon nanowires. *J. Phys. Chem. C*, 111:5855–5858, 2007.

[73] M. M. Adachi M. P. Anantram K. S. Karim. Optical properties of crystalline-amorphous core-shell silicon nanowires. *Nano Lett.*, 10:4093, 2010.

[74] Z. Iqbal S. Veprek. Raman scattering from hydrogenated microcrystalline and amorphous silicon. *J. Phys. C: Solid State Phys.*, 15:377–392, 1982.

[75] H. Richter Z. P. Wang L. Ley. The one phonon raman spectrum in microcrystalline silicon. *Solid State Commun.*, 39:625, 1981.

[76] I. H. Campbell P.M. Fauchet. The effects of microcrystal size and shape on the one phonon raman spectra of crystalline semiconductors. *Solid State Commun.*, 58:739, 1986.

[77] S. Piscaneca A. C. Ferraria M. Cantoroa S. Hofmanna J. A. Zapienb Y. Lifshitzb S. T. Leeb J. Robertsona. Raman spectrum of silicon nanowires. *Materials Science and Engineering C*, 23:931–934, 2003.

[78] K. W. Adu Q. Xiong H. R. Gutierrez G. Chen P.C. Eklund. Raman scattering as a probe of phonon confinement and surface optical modes in semiconducting nanowires. *Appl. Phys. A*, 85:287–297, 2006.

[79] H. E. Ruda A. Shik. Polarization-sensitive optical phenomena in semiconducting and metallic nanowires. *Phys. Rev. B*, 72:115308, 2005.

[80] F. J. Lopez J. K. Hyun U. Givan I. S. Kim A. L. Holsteen L. J. Lauhon. Diameter and polarization-dependent raman scattering intensities of semiconductor nanowires. *Nano Lett.*, pages 2266–2271, 2012.

[81] Q. Xu V. Almeida M. Lipson. Time-resolved study of raman gain in highly confined silicon-on-insulator waveguides. *12*, pages 4437–4442, 2004.

[82] O. Boyraz P. Koonath V. Raghunathan B. Jalali. All optical switching and continuum generation in silicon waveguides. 12:4094–4102, 2004.

[83] T. Shoji M. Takahashi T. Tsuchizawa T. Watanabe J. Takahashi S. Itabashi H. Fukuda, K. Yamada. Four-wave mixing in silicon wire waveguides. *Opt. Express*, 12:4629–4637, 2005.

[84] K. K. Lee D. R. Lim L. C. Kimerling J. Shin F. Cerrina. Fabrication of ultralow-loss si/sio2 waveguides by roughness reduction. *Opt. Lett.*, 26:1888–1890, 2001.

[85] T. Tsuchizawa K. Yamada H. Fukuda T. Watanabe J. Takahashi M. Takahashi T. Shoji E. Tamechika S. Itabashi H. Morita. Microphotonics devices based on silicon microfabrication technology. *IEEE J. Sel. Top. Quantum Electron.*, 11:232–240, 2005.

[86] J. Cardenas C. B. Poitras J. T. Robinson K. Preston L. Chen M. Lipson. Low loss etchless silicon photonic waveguides. *Opt. Express*, 17:4752–4757, 2009.

[87] B. A. Daniel G. P. Agrawal. Vectorial nonlinear propagation in silicon nanowire waveguides: polarization effects. *J. Opt. Soc. Am. B*, 27:956–964, 2010.

[88] V. R. Almeida R. R. Panepucci M. Lipson. Nanotaper for compact mode conversion. *Opt. Lett.*, 28:1302–1304, 2003.

[89] P. A. Kossyrev J. Xu S. G. Cloutier. Optical gain and stimulated emission in periodic nanopatterned crystalline silicon. *Nat. Mater.*, 4:887–891, 2005.

[90] M. J. Chen J. L. Yen J. Y. Li J. F. Chang S. C. Tsai C. S. Tsaic. Stimulated emission in a nanostructured silicon pn junction diode using current injection. *Appl. Phys. Lett.*, 84:2163–2165, 2004.

[91] D. Shiri Y. Kong A. Buin M. P. Anantram. Strain induced change of bandgap and effective mass in silicon nanowires. *Appl. Phys. Lett.*, 93:073114, 2008.

[92] Z. Li B. Rajendran T. I. Kamins X. Li Y. Chen R. S. Williams. Silicon nanowires for sequence-specific dna sensing: device fabrication and simulation. *Appl. Phys. A*, 80:1257–1263, 2005.

[93] K. Q. Peng Z. P. Huang J. Zhu. Fabrication of large-area silicon nanowire p-n junction diode arrays. *Adv. Mater.*, 16:7376, 2004.

[94] C. J. Barrelet A. B. Greytak C. M. Lieber. Nanowire photonic circuit elements. *Nano Lett.*, 4:1981–1985, 2004.

[95] M. Huang S. Mao H. Feick H. Yan Y. Wu H. Kind E. Weber R. Russo P. Yang. Room-temperature ultraviolet nanowire nanolasers. *Science*, 292:1897–1899, 2001.

[96] X. Duan Y. Huang Y. Cui J. Wang C. M. Lieber. Indium phosphide nanowires as building blocks for nanoscale electronic and optoelectronic devices. *Nature*, 409:66–69, 2001.

[97] P. G. Kik H. A. Atwater S. Meltzer E. Harel B. E. Koel A. A. G. Requicha S. A. Maier. Local detection of electromagnetic energy transport below the diffraction limit in metal nanoparticle plasmon waveguides. *Nat. Mater.*, 2:229–232, 2003.

[98] S. A. Maier M. L. Brongersma P. G. Kik S. Meltzer A. A. G. Requicha H. A. Atwater. Plasmonics - a route to nanoscale optical devices. *Adv. Mater.*, 13:1501–1505, 2001.

[99] J. Wang M. S. Gudiksen X. Duan Y. Cui C. M. Lieber. Highly polarized photoluminescence and photodetection from single indium phosphide nanowires. 293:1455–1457, 2001.

[100] T. J. Cui D. R. Smith R. Liu. *Metamaterials Theory, Design and Applications.* Springer, 2009.

[101] L. J. Lauhon M. S. Gudiksen D. Wang C. M. Lieber. Epitaxial core-shell and core-multishell nanowire heterostructures. *Nature*, 420:57–61, 2002.

[102] J. Goldberger P. Yang M. Law. Semiconductor nanowires and nanotubes. *Annu. Rev. Mater. Res.*, 34:83–122, 2004.

[103] M. Gharghi S. Sivoththaman. Formation of nanoscale columnar structures in silicon by a maskless rie process. *J. Vac. Sci. Technol. A*, 24:723–727, 2006.

[104] H. J. Eom. *Electromagnetic Wave Theory for Boundary-Value Problems.* Springer, 2004.

[105] M. Cai O. Painter K. J. Vahala. Observation of critical coupling in a fiber taper to a silica-microsphere whispering-gallery mode system. *Phys. Rev. Lett*, 85:7477, 2000.

[106] G. M. Alman L. A. Molter H. Shen M. Dutta. Refractive index approximations from linear perturbation theory for planar mqw waveguides. *IEEE J. Quantum Electron.*, 28:650–657, 1992.

[107] K. C. Kwan X. Zang Z. Q. Zhang C. T. Chan. Effects due to disorder on photonic crystal-based waveguides. *App. Phys. Lett.*, 25:4414–4416, 2004.

[108] S. Hughes L. Ramunno J. F. Young J. E. Sipe. Extrinsic optical scattering loss in photonic crystalwaveguides: Role of fabrication disorder and photon group velocity. *Physical Review Letters*, 94:1–4, 2005.

[109] F. Grillot L. Vivien S. Laval D. Pascal E. Cassan. Size influence on the propagation loss induced by sidewall roughness in ultrasmall soi waveguides. *IEEE Photonics Technology Letters*, 16:1661–1663, 2004.

[110] X. Fan I. M. White S. I. Shopova H. Zhu J. D. Suter Y. Sun. Sensitive optical biosensors for unlabeled targets: A review. *Analytica Chimica Acta*, 620:8–26, 2008.

[111] B. Bilenberg K. B. Mogensen D. Snakenborg O. Geschke J. P. Kutter S. Balslev, A. M. Jorgensen and A. Kristensen. Lab-on-a-chip with integrated optical transducers. *Lab on a Chip*, 6:213–217, 2006.

[112] W. E. Moerner. New directions in single-molecule imaging and analysis. *Proc. Natl. Acad. Sci.*, 104:1259612602, 2007.

[113] W. G. Cox V. L. Singer. Fluorescent dna hybridization probe preparation using amine modification and reactive dye coupling. *Biotechniques*, 36:114–122, 2004.

[114] B. J. Luff R. D. Harris J. S. Wilkinson R. Wilson D. J. Schiffrin. Integrated optical directional coupler biosensor. *Opt. Lett.*, 21:618–620, 1996.

[115] F. Prieto B. Sepu′lveda A. Calle A. Llobera C. Domi′nguez A. Abad A. Montoya L. M. Lechuga. An integrated optical interferometric nanodevice based on silicon technology for biosensor applications. *Nanotechnology*, 14:907912, 2003.

[116] W. C. L. Hopman P. Pottier D. Yudistira J. V. Lith P. V. Lambeck R. M. De La Rue A. Driessen H. J. W. M. Hoekstra Ren M. de Ridder. Quasi-one-dimensional photonic crystal as a compact building-block for refractometric optical sensors. *J. Sel. Top. Quantum Electron.*, 11:11–16, 2005.

[117] E. S. Hosseini S. Yegnanarayanan A. H. Atabaki M. Soltani A. Adibi. High quality planar silicon nitride microdisk resonators for integrated photonics in the visible wavelength range. *Opt. Express*, 17:14543–14551, 2009.

[118] A. M. Armani K. J. Vahala. Heavy water detection using ultra-high-q microcavities. *Opt. Lett.*, 31:1896–1898, 2006.

[119] L. Rindorf J. B. Jenson M. Dufva L. H. Pedersen P. E. Hiby O. Bang. Photonic crystal fiber long-period gratings for biochemical sensing. *Opt. Express*, 14:8224–8231, 2006.

[120] K. D. Vos I. Bartolozzi E. Schacht P. Bienstman R. Baets. Silicon-on-insulator microring resonator for sensitive and label-free biosensing. *Opt. Express*, 15:7610–7615, 2007.

[121] T. Claes J. G. Molera K. D. Vos E. Schacht R. Baets P. Bienstman. Label-free biosensing with a slot-waveguide based ring resonator in silicon on insulator. *IEEE Photonics Journal*, 1:197–204, 2009.

[122] E. S. Larsen J R. Meyrowitz A. J. C. Wilson. *Mathematical, physical and chemical tables*. Springer, 160-161, 2006.

[123] S. S. Saini C. Stanford S. M. Lee J. Park P. DeShong W. E. Bentley M. Dagenais. Monolayer detection of biochemical agents using etched-core fiber bragg grating sensors. *IEEE Photon. Technol. Letts.*, 19:1341–1343, 2007.

[124] L. Cao P. Fan E. S. Barnard A. M. Brown M. L. Brongersma. Tuning the color of silicon nanostructures. *Nano Lett.*, 10:2649–2654, 2010.

[125] N. Boughen. *Lightwave 3d 7.5 Lighting*. Wordware Publishing, Inc., 2003.

[126] P. V. Lambeck. Integrated optical sensors for the chemical domain. *Meas. Sci. Technol.*, 17:R93–R116, 2006.

[127] S. Peng G. M. Morris. Resonant scattering from two-dimensional gratings. *J. Opt. Soc. Am. A*, 13:993–1005, 1996.

[128] S. Peng G. M. Morris. Experimental demonstration of resonant anomalies in diffraction from two-dimensional gratings. *Optics Letts*, 21:549–551, 1996.

[129] http://www.cargille.com.

[130] B. S. Kim S. Shin S. J. Shin K. M. Kim and H. H. Cho. Control of superhydrophilicity / superhydrophobicity using silicon nanowires via electroless etchng method and fluorine carbon coatings. *Langmuir*, 27:10148–10156, 2011.

[131] S. M. Lee M. Y. Jeong S. S. Saini. Etched-core fiber bragg grating sensors integrated with microfluidic channels. *J. Lightw. Technol.*, 30:1025–1031, 2011.